Geomechanics of Fluid Injection in Geological Reservoirs

by

Kamelia Atefi Monfared

A thesis
presented to the University of Waterloo
in fulfilment of the
thesis requirement for the degree of
Doctor of Philosophy
in
Civil Engineering

Waterloo, Ontario, Canada, 2015

Author's Declaration

I hereby declare that I am the sole author of this thesis. This is a true copy of the thesis, including any required final revisions, as accepted by my examiners.
I understand that my thesis may be made electronically available to the public.

Kamelia Atefi Monfared

ABSTRACT

Numerous petroleum engineering, mining, and enhanced geothermal energy operations involve cyclic injection of fluids into geological formations. Geomechanics of injection operations in weakly consolidated or unconsolidated reservoirs is complex, and means for analyzing the involved physical processes are limited. The key feature that must be considered is parting of the formation during injection, which occurs at near zero effective stresses when strength and stiffness of the medium become effectively zero. Even if peculiarities of the granular media behavior at near zero effective stresses are disregarded and a highly idealized Mohr-Coulomb behavior coupled with constant permeability Darcy flow is assumed, the injection problem is still highly challenging. This type of poroplastic formulation remains analytically intractable even for simplest geometries. Numerical computations are highly challenging as well, due to high fluid-solid matrix stiffness contrast.

Much effort has been devoted thus far to understand soil-fluid interactions in geological reservoirs triggered by borehole excavation and production operations. With regards to injection operations however, practically no comprehensive study has been performed to access the fundamental geomechanical processes involved. Previous attempts to evaluate injection operations mainly concentrate on describing fracture growth in hard brittle formations. In principle, the geomechanical processes prior to fracture initiation are particularly complicated in weakly consolidated strata. This dissertation presents analytical solutions and numerical models to examine geomechanics of high pressure fluid injection in conditions when flow rates are high enough to induce plasticity yet not parting of the formation. The study considers injection through a fully-penetrating vertical wellbore into an isotropic, homogeneous unconsolidated geological layer confined between impermeable seal rock layers. Axisymmetric conditions are assumed. The main objective is to evaluate the time dependent geomechanical response of the unconsolidated reservoir in such conditions

focusing on failure mechanisms and permanent changes in stress conditions around the injection area. Results of this research makes it possible to address the issue of integrity of confining strata, facilitate assessments of potential leakage areas, and offer aid for optimization of injection operations as well as in formulating monitoring strategies.

First, rock-fluid interactions are evaluated prior to the state where limiting shear resistance is reached during injection. Unlike previous studies, impacts of vertical confinement governed by the stiffness of the overburden layer are incorporated. The Winkler spring model approximation is implemented to describe the response of the confining strata in the plane perpendicular to the reservoir. New poroelastic analytical solutions are derived to describe evolution of stress and strain components in time as a function of induced pore pressures. Solutions are verified against fully-coupled numerical models designed in this study. Next, novel insights into the geomechanics of parting in various stress regimes is offered via a comprehensive assessment of stress perturbations surrounding vertical injection wellbores. A thorough sensitivity analysis is conducted to examine the effect of vertical confinement and rock-fluid characteristic parameters on the reservoir response in the wellbore vicinity. Results demonstrate a notable impact of seal rock stiffness on the near wellbore rock behavior in formations with high intrinsic permeability (typically exceeding 0.05 Darcy). The study shows that the key parameter controlling the injection process in the poroelastic regime is the ratio of the overburden Winkler stiffness to the reservoir's bulk modulus, with the Winkler parameter reflecting the seal rock stiffness. When this ratio approaches unity, practically no shear stress is induced in the reservoir while for ratios exceeding unity, deviatoric stresses gradually increase. In situations when the stiffness ratio is below unity, the porous formations can behave in a rather complicated manner depending on the initial stress regime where redirection of the minimal principal stress occurs from a horizontal to a vertical plane. Sensitivity analyses reveal that at the same injection rate rock failure occur more rapidly in conditions of higher stress anisotropy, higher elastic moduli, lower permeability, higher degree of rock-fluid coupling, and a higher vertical confinement.

Next, rock-fluid interactions are evaluated in an unconsolidated reservoir formation confined between two stiff seal rock layers subjected to injection pressures high enough to induce plasticity yet not parting of the formation. The injection process is first examined numerically by constructing a fluid-coupled poro-elasto-plastic model in which propagation of the significant influence zone surrounding the injection borehole is quantified by the extent of the plastic domain. A comprehensive assessment of stresses, pore pressures, as well as failure planes is carried out throughout an entire transient state of an injection cycle, at steady state, and also during the shut-in period. The numerical solution describes five distinct zones evolving with time around the injection well and corresponding to different stress states: liquefaction at the wellbore followed by three inner plastic domains where directions of major principal stress changes from

vertical to radial and failure planes change accordingly. The plastic domains are followed by a region where stress states remain in the elastic range. Failure mechanisms at the wellbore is found to be in shear initially, followed by development of a state of zero effective stress, i.e. liquefaction. Next, a novel methodology is proposed based on which new weakly-coupled poro-elasto-plastic analytical solutions are derived for the stress/strain components during injection. Unlike previous studies, extension of the plastic zone is obtained as a function of injection pressure, incorporating the plasticity effects around the injection well. The derived loosely-coupled solutions are proven to be good approximations of fully-coupled numerical models. These solutions offer a significant advantage over numerical computations as the run time of a fully-coupled numerical model is exceedingly long (requiring about six months for 661 million time computational steps using FLAC3D 3.0 code on Intel® i7 3.33 GHz CPU).

The final part of this dissertation includes a brief chapter on the post-injection behavior of unconsolidated reservoir formations confined with stiff seal rock layers. Pore pressure dissipation, stress variations, and the transition behavior of the plastic domain surrounding the injection wellbore to an elastic state are numerically evaluated. Results offer an original insight into the permanent geomechanical effects of injection operations in such formations.

Acknowledgements

The author wishes to express her sincere appreciation to supervisor Professor Leo Rothenburg, to whom will always be indebted for his ongoing support, valuable insights, and stimulating guidance throughout these years.

Sincere appreciation to Professor Giovanni Cascante for his valuable comments, continuous support, precious motivation, and always kind attention.

Appreciation is extended to Professor Maurice Dusseault and Professor James Craig for their valuable comments and advice.

Financial support from the Natural Science and Engineering Council of Canada is gratefully acknowledged.

Heartfelt thanks to my father Amir Pasha for being the greatest mentor and role model and supporting me in all possible ways. Special thanks to my mother Golrokh for her unconditional love and support. To my sister Yasaman, special thanks for her affection, encouragement, and cheerfulness. Many thanks to my dear friends, specially the soil's lab group for their valuable friendship and support.

To my father and mother…

Contents

List of Tables

List of Figures

CHAPTER I

1. Introduction

This dissertation presents a multi-faceted effort to assess coupled geomechanical processes involved during fluid injection from a fully penetrating vertical wellbore into a confined unconsolidated geological reservoir. The study focuses on the poroelastic and poro-elasto-plastic response of the unconsolidated medium, concentrating on injection pressures that are high enough to induce plasticity yet not fracturing, explicitly fracture propagation. Unlike previous studies, impacts of vertical confinement – governed by the stiffness of the confining layers – on the coupled response of the reservoir formation during injection are incorporated. Stress changes induced during injection operations may: damage the confining seal rock layers, compromise the hydraulic integrity of the reservoir; and increase the potential for reactivation of existing faults. The key objectives of this research endeavor are: to attain novel insight into geomechanics of failure initiation in confined unconsolidated reservoirs (failure mechanism/s and failure plane/s), to quantify the extent of the significant influence zone induced around a fully-penetrating vertical injection wellbore, and to assess the permanent geomechanical impacts of injection operations in such formations. Results of this study facilitate prediction of potential leakage areas, and help optimize injection operations as well as monitoring strategies.

This chapter presents a brief history of the development of hydraulic fracturing technology, describing common injection operations being carried out in weakly consolidated and unconsolidated reservoirs. Next, the geomechanical aspects of injection in such formations and the coupled nature of the involved processes is briefly discussed. The final part of this chapter includes a brief literature review of previous studies on coupled soil-fluid interactions associated with production and injection operations in geological formations.

1.1 Injection Operations in Geological Reservoirs

Hydraulic fracturing is a broad term adopted to define processes through which a fracture initiates and propagates in the porous media as a result of hydraulic loading (Adachi et al., 2007). Magma-driven dikes, typically on the scale of tens of kilometers, are examples of nature-induced hydraulic fractures (Spence et al., 1985; Lister, 1990; Rubin, 1995).

Hydraulic fracturing was originally utilized by the petroleum industry for the purpose of facilitating oil flow (stimulation). Fracturing is reportedly traced back to the 1860s, when liquid nitroglycerin was applied to stimulate shallow, hard rock wells in Pennsylvania, New York, Kentucky, and West Virginia (Montgomery et al., 2010). Despite being extremely hazardous and often used illegally, nitroglycerin was tremendously successful for oil, water, and gas well "*shooting*". In the 1930s, the idea of injecting a nonexplosive fluid (acid) into the ground to enhance well stimulation began to emerge. The "*pressure parting*" phenomenon was recognized in this era, where a fracture can be generated in situ under induced injection pressures, leaving a flow channel to the well and enhancing productivity. This phenomenon was later confirmed during water injection and squeeze-cementing operations. Floyd Farris was the first who performed an in-depth study to stablish a relationship between observed well performance and treatment pressures. Farris conceived the idea of hydraulically fracturing a formation to enhance production from oil and gas wells. The first experimental hydraulic fracturing stimulation operation was carried out by Stanolind Oil in the Hugoton Gas field, Kansas, in 1947 (Mader, 1989; Montgomery et al., 2010; Shokanov et al., 2011), where a total of 1,000 gal of naphthenic-acid- and palm-oil thickened gasoline followed by a gel breaker were pumped into the limestone formation at a depth of 730 m. The first two commercial hydraulic fracturing treatments were conducted in 1949 by Halliburton Oil Well Cementing Company, one in Stephens County, Oklahoma and the other in Archer County, Texas. The fracking fluid applied in these treatments was a blend of crude and gasoline, and 45 – 70 kg of sand.

Applications of hydraulic fracturing technology grew rapidly over the years. Nowadays, abundant petroleum engineering operations, mining, enhanced geothermal energy, and environmental industry projects involve hydraulic fracturing processes. These operations include: fracturing of oil and gas reservoirs using a mixture of viscous and non-viscous hydraulic fluids and sorted sand (proppant) for reservoir stimulation (Mack et al., 2000); disposal of waste drill cuttings into depleted hydrocarbon reservoirs (Moschovidis et al., 2000); heat production from geothermal reservoirs (Pine et al., 1985; Legarth et al., 2005; Hofmann et al., 2014; Zhang et al., 2014; Zhang et al., 2015); removing of the minerals from

mines, i.e. goafing (Zhang et al., 2002), fault reactivation in mining (Board et al., 1992); and measurement of in situ stresses (Desroches et al., 1993; Desroches et al., 1995).

While the idea of hydraulic fracturing is somewhat similar for various projects, execution mainly depends on the type of reservoir rock, or more specifically the geomechanical characteristics of the porous strata. Although developed primarily for hard, brittle reservoir formations, hydraulic fracturing is nowadays being carried out in extremely diverse geological settings: low permeability gas fields, weakly consolidated sediments, soft coal bed for methane extraction, naturally fractured reservoirs, and geometrically complex structures such as lenticular formations (Adachi et al., 2007).

Over the years, global population increase superimposed with limited earth resources has fostered development of challenging resource exploration techniques. Weakly consolidated reservoirs (i.e. sandstones) thus became of substantial interest to the petroleum industry. In fact, over 70% of the oil and gas reservoirs are reportedly characterized as weakly consolidated or unconsolidated strata (Bianco, 1999; Walton et al., 2002; Bellarby, 2009). Common high pressure injection operations carried out in such reservoirs are essentially modifications of the original hydraulic fracturing technology. In the petroleum engineering sector, such operations include: gravel injection, and Frac-Pack to minimize sand production during oil and gas extraction; grout injection to create barriers for contaminant flow in porous media; and slurry fracture injection (SFI) for permanent disposal of waste (Bruno et al., 2001).

Gravel injection and Frac-Pack are technologies developed for the purpose of minimizing sand production during extraction of oil and gas operations in weakly consolidated reservoirs (Figure 1-1) (Economides et al., 2000; Sanchez et al., 2007). Large volumes of produced oily sand, in extreme cases several tons from one reservoir in a single day (Sanchez et al., 2007), create major complications through affecting hydrocarbon extraction, damaging vital production equipment, and generating an additional problem of waste disposal. Frac-Packing, initially conducted in the Gulf of Mexico in 1980s, is a relatively new technology compared to the conventional gravel pack techniques adopted to reduce sand production (Sanchez et al., 2007). Frac-Packing involves simultaneous hydraulic fracturing of the reservoir formation using a viscous fluid (to improve production by providing a highly conductive crack) and the placement of a gravel pack (to provide effective sand control) (Chekhonin et al., 2012). Tip Screenout (TSO) treatment is commonly adopted for Frac-Pack operations to intentionally hinder fracture propagation and to increase fracture width in weakly consolidated strata. TSO treatment is also frequently intended to improve well productivity in both high permeable reservoirs (permeability higher that 5.0 Darcy for oil reservoirs; 0.5 Darcy for gas reservoirs) (Economides et al., 2002), and moderately permeable formations (permeability

greater than 0.5 Darcy for oil reservoirs; 0.05 Darcy for gas reservoirs) (Economides et al. 2000). A typical TSO treatment includes several consistent stages: (a) Fluid injection resulting in fracture initiation and unsteady-state propagation; (b) Proppant injection; and (c) Leakoff, creating a zone of packed proppant screen at the tip of the fracture. Formation and evolution of the proppant screen prevents further propagation of the fracture and results in an increase in fracture width or "*ballooning*". Thus, the induced fracture is notably shorter and wider (usually up to 30 m length, and several cm width) compared to that of a traditional treatment (typically extends more than 150 m in hard rock) (Fan et al., 1996; Sanchez et al., 2007).

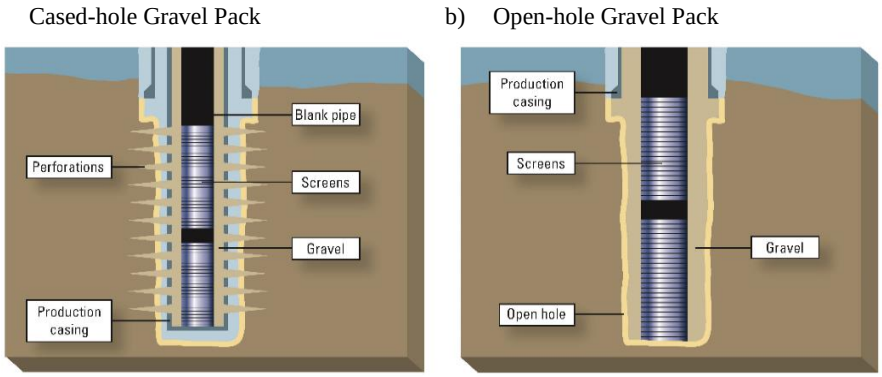

Figure 1-1. A schematic of gravel pack in a) cased wellbore b) open-hole (Sanchez et al., 2007).

Slurry Fracture Injection (SFI)™ (courtesy of Terralog Technologies Inc.) is a technology established for final disposal of hydrocarbon production waste. Depositing industrial waste into geological formations has in fact been practiced from as early as 1930. By 1986, 944 deep injection wells were already operational in the continental United States, and 576 new wells were being built or in the commissioning process (Akpoborie, 2005). Figure 1-2 illustrates the distribution of hazardous deep wells in the United States, prior to 2001.

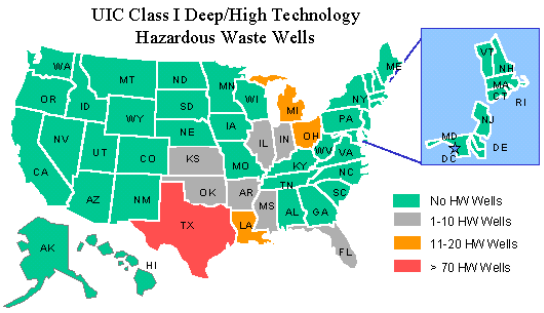

Figure 1-2. Distribution of hazardous wells in the United States prior to 2001 (U.S. Environmental Protection Agency website).

SFI technique is in fact a modification of hydraulic fracturing technology, designed to enable cyclic injection of large volumes of solid/semi-solid waste under moderate to high pressures for periods of months to years through the same well (Dusseault et al., 1997). The process of SFI operation involves forming an aqueous slurry from a mixture of fine granular solid waste screened to a particle size of normally less than 3- 5 mm (concentration of typically 20 - 30% by weight depending on characteristics of the disposal formation), OVF (oily, viscous fluids including emulsions, tank bottoms), and waste water. Rheological properties of the slurry can be adjusted using additives in some circumstances (e.g. corrosion inhibitors, biocides, friction reducers) (Sanfilippo et al., 2009). The slurry is then injected into a suitable deep geological formation which acts as a containment zone (Figure 1-3). Injection pressures must be maintained above certain values to ensure injectivity over time. Injection rate is however restricted between a given range (e.g. 3 – 7 bpm) in order to maintain control over fracturing, and to reduce wear and tear of well completion and surface equipment (Shokanov et al., 2001). Identification of suitable target zones is a key element of a successful SFI operation.

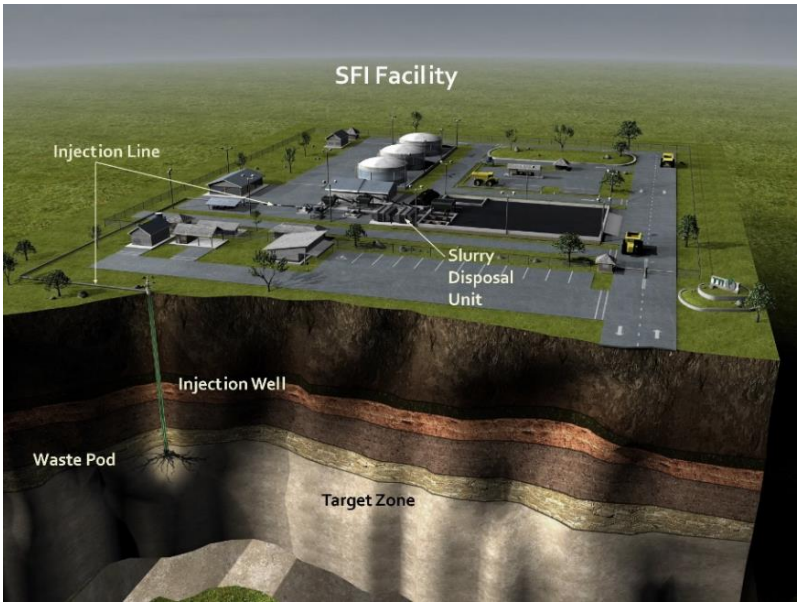

Figure 1-3. A schematic of SFI facility and operation (courtesy of Terralog Technologies Inc.).

The first experimental SFI operation was executed in Saskatchewan by Mobil Canada in the late 1980s for permanent disposal of produced oily sand (Dusseault et al., 1995). In this operation, a total of 10,000 m^3 of fine-grained produced sand was pumped into a 35 m thick unconsolidated sandstone at a depth of 690 m over a period of several years. Ever since, the SFI technique has widely been implemented in the United States, Canada, The North Sea, Indonesia, Nigeria, and The Middle East for disposal of non-hazardous oil field waste as well as naturally occurring radioactive materials (NORMs) (Schuh et al., 1993; Sipple-Srinivasan et al., 1997, 1998; Baker et al., 1999; Reed et al., 2001; Arfie et al., 2005; Saif Ud Din et al., 2009; Sanfilippo et al., 2009).

Large volumes of aqueous waste referred to as wastewater or produced water, as well as contaminated solid semi-solid waste, are produced as a result of hydrocarbon related drilling, production, transportation and storage processes. Main waste streams in the hydrocarbon industry include: heavy oils, water treatment sludges, tank bottoms, produced solids, difficult emulsions, and produced water. Various studies carried out by Khatib et al., (2002), Dal Ferro et al., (2007), and Fakhru´l-Razi et al., (2009) suggest an estimated 250 million barrels of produced water extracted for 80 million barrels of produced oil per day worldwide, i.e. a 3:1 water/oil ratio (Figure 1-4). To demonstrate the significance of the produced solid waste, data from the Kuwait Oil Company Facilities in Ahmadi and Wafra operations alone will suffice, which indicate an estimated 1,847,000 tons of solid and semi-solid waste generated annually (Al Salem et al., 2007).

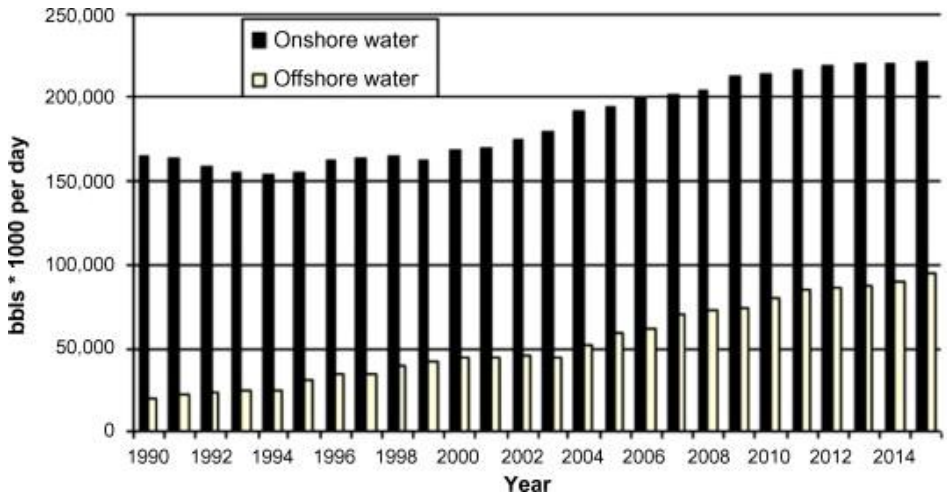

Figure 1-4. Global onshore and offshore water production (Dal Ferro et al., 2007).

Conventional methods of waste disposal, i.e. lined or unlined (to allow desiccation) pits, continue to raise serious issues in terms of long-term environmental integrity (Saif Ud din et al., 2009). Deep well disposal techniques are proven to be valuable alternatives to the traditional methods, as – if properly implemented – they are viable to achieve permanent waste disposal with "zero discharge" without compromising future land-use, affecting land-cover, or deteriorating groundwater quality.

A slurry injection operation is a multi-cycle injection process which consists of several injection and shut-in periods. In practice, a single injection episode is carried out in three phases as illustrated in Figure 1-5. The initial phase, commonly referred to as *pre-conditioning*, involves pumping of solids-free waste water at pressures to fracture/open the porous reservoir formation. This stage is followed by the second phase which is the actual slurry injection cycle. This injection phase continues for many hours/days, and is followed by the third and last phase, referred to as *post-flush*, during which water is pumped to clean up the injection system, the well, and the near-wellbore system, assuring injectivity for subsequent injection cycles. Following this cycle, the well is closed and down-hole pressure is monitored. It is important to consider that each phase of the injection process generates short-term as well as permanent geomechanical changes within the unconsolidated medium, affecting the response of the formation during subsequent injection cycles. Therefore, to be able to properly assess the geomechanical and environmental impacts of cyclic injection operations, it is crucial to obtain a comprehensive understanding of the coupled rock-fluid interactions from initiation of the injection start-up (pre-conditioning phase).

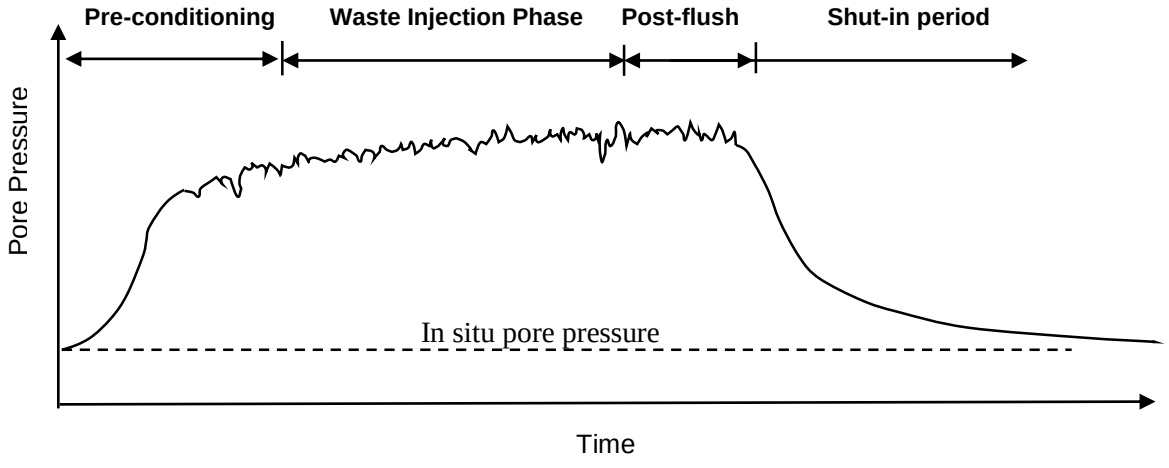

Figure 1-5. Details of one injection episode of a slurry injection operation.

1.2 Geomechanics of Fluid Injection

Injection of fluids in a reservoir results in changes in pore pressure and fluid mass content within the injection layer, bringing about stress variations. More specifically, an increase in pore pressures is generated in the wellbore vicinity. This translates into poroelastic dilative strains in the porous structure surrounding the well, which in turn result in a reduction in pore pressures, bringing about further stress/strain variations. Clearly, there exists a coupling between rocks' mechanical response and the quantity of the interstitial fluid flow within the weakly consolidated porous medium during injection operations. The degree of this coupling depends on different parameters, including formation type and structure as well as fluid properties. As long as pore pressures continue to change, coupled fluid-rock interactions result in a time dependent behavior of the porous strata. The overall geomechanical response of the reservoir formation is dependent upon vertical confinement governed by stiffness of the surrounding rocks which include the seal rock layers. Under high enough induced pore pressures, the porous formation at the wellbore vicinity reaches a state of limiting shear resistance (failure). The formation then behaves in a poroplastic manner. The region undergoing a state of limiting shear resistance, wherein the rock behaves in a poroplastic manner, is referred to as the *plastic domain* in this study. All the aforementioned geomechanical interactions are believed to take place during the pre-conditioning phase.

During the shut-in period, pressures in the formation drop. The fluid phase of the injected slurry will leak into the formation, resulting in compaction of the injection zone and trapping of the solid particles within fractures/voids surrounding the injection well, the area commonly referred to as the *waste disposal domain* (Sanfilippo et al., 2009, Shokanov et al., 2011) (Figure 1-6). As a result, polyvalent cations and other dissolved constituents will become adsorbed and diluted. These weakened particles will disperse during flow, and be adsorbed on clays and other minerals, and therefore attenuated with distance from the injection point. Eventually, the injectate becomes more environmentally benign (Nadeem et al., 2005).

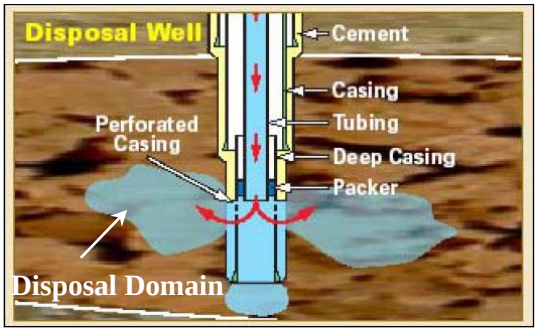

Figure 1-6. Waste Injection through deep wells (Sanfilippo et al., 2009).

The majority of the induced pore pressures and deformations (strains) as a result of injection are in fact generated within the plastic domain. The extent of the significant influence zone surrounding the injection wellbore can thus be quantified by the extent of the plastic region in the elasto-plastic model. The induced subsurface deformations generate ground level movements. More specifically, the increase in the volume of the reservoir rock as a result of injection pressures results in a surface heave (Figure 1-7). Ground surface deformations, if large, may cause substantial environmental impacts (e.g. flooding, shift of coastline) in addition to generating failure in structures and/or infrastructures. It is thus important to be able to predict the extent of the impacted ground surface region prior to initiating an injection operation. It should be noted that the area of the ground surface impacted domain is an important parameter for direct/indirect monitoring of the injection operation. This is because the depth and distribution of the sources of deformation directly affect the extent of the ground surface deformation field as well as the magnitude of deformation matrixes (vertical and horizontal displacements, tilt measurements) (Kroon et al., 2008; Atefi Monfared et al., 2011). It is thus essential to be able to predict the extent of the significant influence zone (plastic domain) within the reservoir formation during injection operations, to not only optimize the injection process, but to foresee the induced ground surface deformation field.

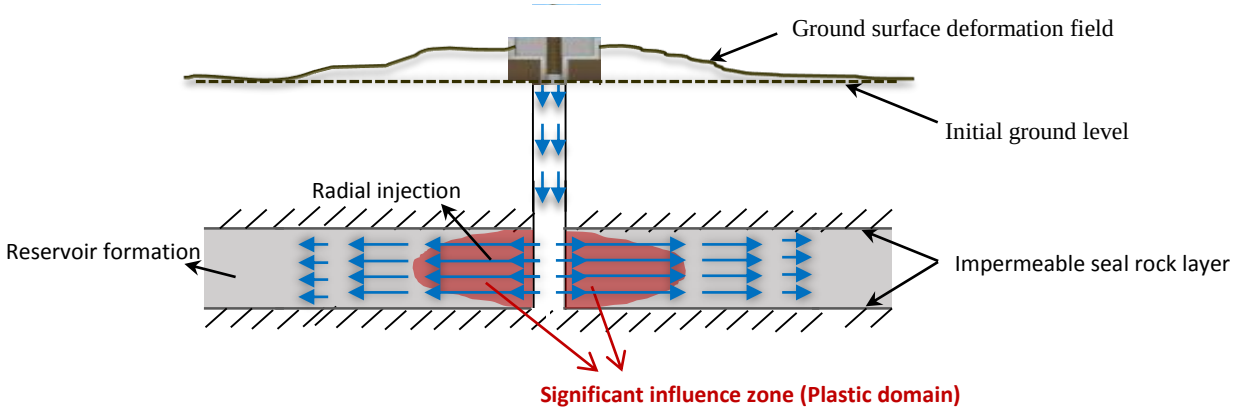

Figure 1-7. A schematic of an idealized radial injection operation from a fully-penetrating vertical well into a confined reservoir formation.

1.3 Literature Review

In order to ensure a safe and effective injection process, it is critical to assess pressure-induced stresses and to evaluate the geomechanical response of the reservoir formation. Reservoir expansion during injection operations and the resulting stress variations may damage the confining seal rock layers, and therefore compromise the hydraulic integrity of the reservoir. Furthermore, stress alterations within a reservoir formation can increase the potential for reactivation of existing faults (Soltanzadeh et al., 2008). The theory of poroelasticity, introduced by Terzaghi (1923) in one dimension and later extended to three dimensions by Biot (1941), is the first theory describing coupled fluid-soil interactions. Relevance of poroelasticity to rock mechanics was originally discussed by Geertsma (1957), who was the first to apply this theory to address coupled geomechanical processes during petroleum production operations. Subsequently, much effort has been devoted to understand soil-fluid interactions, most of which involve borehole drilling and production operations (Paslay at al., 1963; Risnes et al., 1982; Segall, 1992; Chin et al., 2000; Han et al., 2003; Yin et al., 2006). Hubbert and Willis (1957) conducted a linear elastic analysis surrounding a vertical wellbore based on the plane strain assumption, not taking into account coupled rock-fluid interactions due to excavation. Rice and Cleary (1976) presented deformation-diffusion solutions for fluid saturated elastic porous media under plane strain conditions. Carter and Booker (1982) proposed a method of analysing soil-fluid behavior due to drilling of a vertical borehole in a linear elastic medium, under plane strain conditions and assuming incompressible fluid and soil constituents. Detournay and Cheng (1988) proposed more generalized solutions for the poroelastic processes triggered by the excavation of a vertical borehole in a saturated formation under plane strain conditions, taking into account compressibility of fluid and soil. The coupling effect of strains on the induced pore pressures were not accounted for in that study. Egberts and Fokker (2001) presented an analytical approximation of flow into a well assuming steady state conditions.

Risnes et al. (1982) presented weakly-coupled elasto-plastic solutions for stresses surrounding a production wellbore at steady state. Principal stresses were presumed to be along the main directions in the cylindrical coordinate system. The extent of the plastic domain and stresses in it were determined from elastic solutions outside of the plastic zone. Han and Dusseault (2003) derived a general analytical method to describe fluid flow at steady state surrounding a production wellbore in an unconsolidated sand with stress dependent porosity and permeability. It was suggested that the stress dependent aspect of porosity and permeability may be considered negligible when evaluated in terms of pore pressure variations as far as stress analysis is concerned.

Numerous analytical models have been presented in the literature for predicting deformations (subsurface and/or ground surface) generated as a result of production or injection-induced stress changes, many of which are developed assuming a uniaxial compaction or expansion of the reservoir rock. That is, the total horizontal stresses changes within the reservoir, whereas the total vertical stress remains constant (Zoback and Zinke, 2002; Goulty, 2003; Streit and Hillis, 2004; Hawkes et al., 2005). Engelder and Fischer (1994) conducted an analytical study on the influence of poroelastic behavior on the magnitude of the minimum horizontal stress in over-pressured zones of sedimentary basins, under the assumptions of: a constant vertical stress which is independent of in situ pore pressures, zero horizontal strains, and identical changes in the maximum and minimum horizontal stresses. A uniaxial based model is considered to be acceptable for estimating induced stress changes in some limited cases (i.e. thin horizontal reservoirs) (Segall and Fitzgerald, 1998). The conventional uniaxial strain assumption does not hold for all geometries, shallow or thick reservoirs, or in cases where the elastic moduli of the reservoir formation differs significantly from that of the confining formation (e.g. the North Sea Reservoirs). Soltanzadeh and Hawkes (2008) adopted Eshelby's theory of inclusions to evaluate stress changes in a poroelastic half-space under plane strain conditions with the intention of assessing the possibility of fault reactivation as a result of production or injection. The proposed model does not account for cases where the mechanical properties of the reservoir differ from those of the surrounding rocks.

With respect to injection operations, practically no comprehensive study has been performed on the fundamental geomechanical processes involved in unconsolidated or weakly consolidated geological formations. The geomechanical processes involved during injection operations in such formations are complicated and not yet well understood. Strong flow-stress coupling, large non-linear deformations, and plasticity are typical in weakly consolidated formations under high induced pore pressures. Furthermore, the cyclic nature of injection operations in such reservoirs adds to the existing complexities. The intricate behavior of unconsolidated soils is commonly associated with high permeability, no cementation, Young's modulus less than 1 GPa (Bohloli et al., 2006), and low mechanical strength of these formations.

Most hydraulic fracture models are developed based on Linear Elastic Fracture Mechanics (LEFM), therefore mainly applicable for hard brittle formations rather than weakly consolidated strata. There are various approaches proposed in the literature to numerically simulate fracturing, most of which concentrate on describing fracture growth (Gil et al., 2003; Wong 2003, 2003; Chin 2004; Zhai et al. 2005; Khodaverdian et al. 2009; Xu et al. 2010; Wangen 2011). Thallak et al. (1991) applied a discrete element method to study lateral growth and interactions of fluid induced fractures in unconsolidated medium. Wang et al. (1991) discussed fracture initiation in weakly consolidated rocks under plane strain conditions,

assuming pre-existence of plastic yielding due to borehole excavation prior to injection initiation. This assumption is not always accurate in case of deep boreholes with casing, where mud drilling (a commonly adopted excavation technique) partially counteracts major modifications in the in situ stress field. Potyondy et al. (1996) proposed the Bonded Particle Model to represent the behavior of rock under fluid injection. A different approach for simulating hydraulic fracturing in unconsolidated media was introduced based on lab experiments suggesting possible fingering at the interface of the injectant and in situ sand (Germanovich et al., 2012). Based on this fluid-like behavior, fracturing was treated as a viscous fluid invading another viscous fluid, results of which provide a good insight into interactions of competing forces on fracturing process. This type of simulation however, does not allow evaluation of in situ stresses. Showalter et al., (2004) presented an analytical work on diffusion in saturated inelastic media. Different material behaviors were considered; however, no specific solution to boundary value problems was detailed.

Most previous work on evaluating injection processes in a porous medium are developed based on at least one of the following assumptions: uncoupled soil's reaction with respect to induced pore pressures; uncoupled pressure variations with respect to stresses/strains; elastic behavior of reservoir rock; presence of a pre-existing fracture prior to injection initiation; independency of in situ conditions in the elastic domain from the plastic zone; a constant stress pattern throughout the plastic domain; and plane strain conditions perpendicular to the flow direction, thus ignoring impacts of the surrounding sealing rock layers on the coupled geomechanical response of geological reservoirs. Thus far, practically no comprehensive study exists on the coupled geomechanical response of unconsolidated formations during injection prior to fracture initiation. Typically, runtime of a tightly-coupled flow-mechanical simulation is slow even with the powerful computers nowadays. Consequently, no comprehensive study has been reported on the coupled response of an unconsolidated reservoir during a considerable duration of an injection cycle (an entire transient state). Assessments presented in the literature have been carried out at either very early times subsequent to injection initiation, or at steady state.

This dissertation presents a multi-faceted effort to assess the time-dependent, tightly-coupled geomechanical processes involved during fluid injection operations in geological reservoirs. The study focuses on the pre-conditioning phase of the injection cycle and thus injection pressures that are high enough to induce plasticity yet not fracturing, explicitly fracture propagation, within the unconsolidated medium. Unlike previous studies, effects of vertical confinement controlled by seal rock stiffness on the coupled response of the reservoir formation during injection are incorporated.

Chapter II

2. General Background

The current chapter presents geotechnical information on hydrocarbon reservoirs, and introduces common characteristic parameters adopted to describe these geological formations. In order to be able to conduct a realistic evaluation of the behavior of weakly consolidated reservoirs, data on characteristic parameters of weakly consolidated basins located in different parts of the world are presented. The major part of this chapter includes constitutive laws developed to describe the response of such formations due to changes in pore pressures.

2.1 Weakly Consolidated Sedimentary Basins

Hydrocarbon reservoir formations typically consist of reservoir rock, sealing rock layers and/or traps, and fluid content. A *reservoir rock* is formed of a porous permeable bed composed of sandstones (unconsolidated reservoirs); carbonates (most common naturally fractured reservoirs; i.e. limestone, dolomite); shales; cherts, siltstones or basement rocks. Sandstones and carbonates are the most common reservoir rocks. *Seal rocks* are composed of low permeability strata which enable confinement of hydrocarbon and/or fluids within the reservoir rock. The most common seal rock is shale. Typically, seal rocks exhibit elasto-plastic characteristics and are not subject to actions initiating fractures. *Traps* are formed of impervious material and thus help retain hydrocarbons within the reservoir formation. Petroleum geologists classify traps into two categories: structural and stratigraphic. A structural trap is where the folding or faulting of the rock layer contributes to the trapping mechanism, whereas a stratigraphic trap involves lateral changes in permeability, forming capillary flow barriers (Aguilera 1980).

Porosity and permeability are two important characteristic parameters of a reservoir rock. *Porosity* is expressed as the void space fraction of the bulk volume of the rock, and is classified as primary and secondary. Primary porosity is formed when the formation is deposited and is therefore an inherent original characteristic of the rock; secondary porosity (induced porosity) however, is caused as a result of dissolution, recrystallization, and/or fracturing (Aguilera 1980). *Bulk porosity* is the term commonly used when the entire pores within a soil specimen are incorporated. *Effective porosity* however takes into account the pores which are part of a unified system of interconnecting pores contributing to flow. The higher the porosity of a target zone, the higher its potential for solid waste storage would be. Unconsolidated, high porous rocks are therefore considered to be more favorable for the purpose of deep slurry injection operations compared to naturally fractured carbonate formations (Nadeem et al., 2005). Furthermore, high porosity is important for enabling liquid leakage and excess pore pressure dissipation to occur within a reasonable time. Porosity of sandstone is reported to be 10% - 40%, depending upon the nature of the cement and state of consolidation (Monicard, 1980).

Permeability is the ability of porous media to transmit fluids. Permeability is generally described in terms of *primary permeability* (matrix permeability), associated with the intact rock blocks between fractures; and *secondary permeability*, which is defined in terms of fractures or solution vugs. In general, stiff materials (e.g., limestone) are brittle and often possess low permeability; they tend to produce thin-long fractures as a result of injection-induced strains. On the other hand, porous and permeable formations with low stiffness (e.g., cohesionless sands or intensely fractured reservoirs) induce thick fractures (wide in aperture and short in length) under injection-induced strains, which can entomb greater volumes of solid waste compared to thin long fractures. Furthermore, the major factor facilitating the dissipation rate of the induced pressures within the disposal domain is believed to be formation permeability. Consequently, even though it is difficult to generate and sustain fractures in highly permeable formations, high permeability is favorable for enabling storage of large volumes of waste and facilitating pressure dissipation. However, permeability higher than 10 Darcy (9.87×10^{-12} m^2) is considered to be a negative factor for slurry injection due to high leakage which will prevent pressure build-up, a desirable parameter for inducing fractures during the injection initiation phase (Nadeem et al., 2005). Typically, the higher the porosity of a rock, the higher its permeability would be; this is not however a unique or well-defined relationship (e.g., high-porosity shale is almost impermeable compared to high-porosity coarse-grained sandstone). Permeability for unconsolidated sandstone is typically reported to be in the range of 0.5 – 5 Darcy (Pape et al., 1999). Some literature data on the characteristic parameters of weakly consolidated and/or unconsolidated sandstone reservoirs from different basins of the world is given next. Figure 2-1 illustrates permeability

versus porosity of a Permian deep-water Sandstone, East Ford Field, Delaware Basin, Texas (Dutton et al., 2003). Table 2-1 presents characteristics of sandstone reservoirs from the CockField formation of Louisiana (Monicard, 1980). Figure 2-2 demonstrates permeability and porosity of Rotliegend Sandstone from hydrocarbon reservoirs located in northeast Germany (Pape et al., 1998). Figure 2-3 presents data on porosity from Maritimes Basin in Eastern Canada (Hu et al., 2009). More data on characteristics of weakly consolidated and/or unconsolidated sandstone reservoirs can be found in Warren et al., 1997, and Bratli et al., 1981.

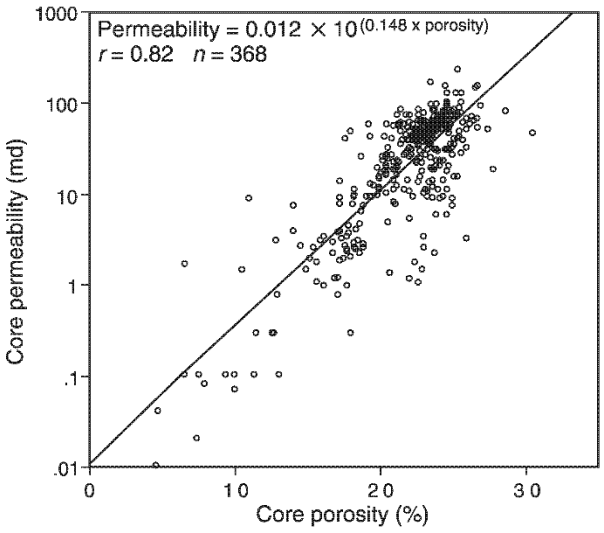

Figure 2-1. Cross plot of core porosity versus core permeability with porosity-permeability transform for the Ramsey sandstone in the East Ford Unit, Reeves County, Texas (Dutton et al., 2003).

Table 2-1. Sandstone characteristics from the CockField formation (Monicard, 1980).

Lithology	k_a (mD)	ϕ %	S_o %	S_{TW} %	Probable production	Observations
Clean sandstone	380	29	10	47	Oil	
Clean sandstone	350	30	2	42	Gas	
Clean sandstone	300	28	2	65	Water	
Clayey sandstone	15	24	3	70	Oil	Clayey
Clayey sandstone	50	24	1	75	Gas	
Clean sandstone	300	28	20	20	Oil	$S_{TW} \approx S_{cw}$
Clean sandstone	400	30	15	40	Oil	
Clean sandstone	500	31	7	50	Water	
Clean sandstone	300	30	2	60	Water	
Clays				Not analysed		

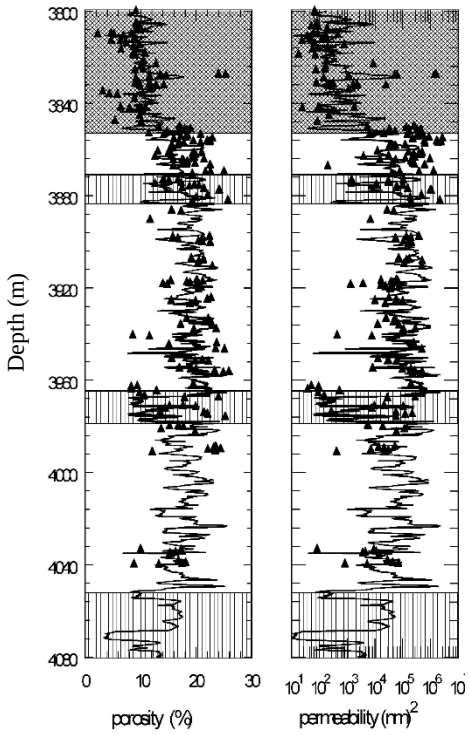

Figure 2-2. Sandstone characteristics (Pape et al., 1998).

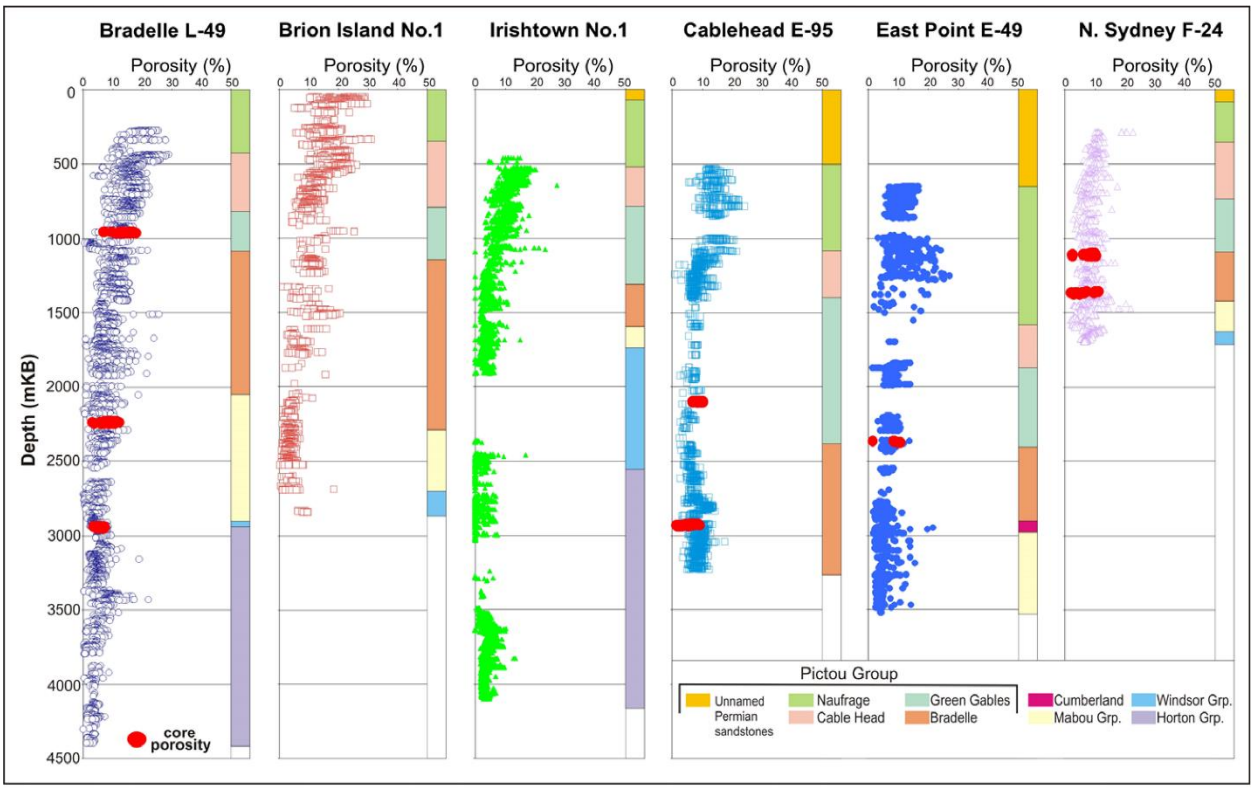

Figure 2-3. Porosity-depth plots for 6 wells in the Maritimes Basin (Hu et al., 2009).

2.2 Scaling

Different scales used for describing flow in a porous medium are: molecular scale at which molecular diffusion occurs; pore scale (wherein continuum equations are valid); Darcy scale (hundreds to thousands of pores forming a representative elementary volume (REV), where the average of material properties can be calculated, and within which Darcy's law is valid) (Detournay et al., 1993, Yang et al., 2004); and mega-scale (macroscopic scale), where effects of heterogeneity, anisotropy, and geological stratification are considered (Figure 2-4).

In classic continuum mechanics, the porous medium is typically described at the REV scale, which is large compared to the micro-scale, but small compared to the scale of the investigated phenomenon (Gueguen et al., 2004). This would provide an idealized continuum where mechanical quantities can be averaged. Consistent with classical continuum mechanics, any quantity appearing in this study will be averaged over a certain length scale, which is large compared to the micro-structure scale, and yet small enough to allow the study of material heterogeneity.

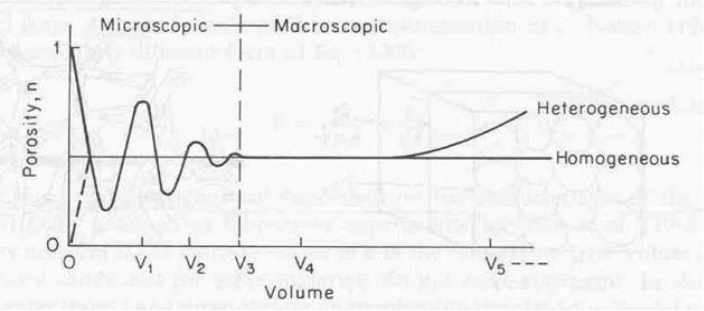

Figure 2-4. Microscopic, REV (V3), and macroscopic domains (after Hubbert 1956; Bear 1972; Freeze et al. 1979).

2.3 Basic Constitutive Laws

The basic principles governing Newtonian mechanics are conservation of mass, conservation of momentum, conservation of moment of momentum (or angular momentum), conservation of energy, and the laws of thermodynamics. These principles are valid for all materials irrespective of their internal constitution. In order to describe the behavior of a material based on its nature, constitutive equations/laws are required. Models of engineering materials, or stress-strain laws, have a significant role in characterization of physical processes. In order to determine a suitable constitutive model for a material, the following factors should be considered: external excitation, internal constitution of the medium, and the media's response (Desai et al., 1984).

There are four generic types of idealized constitutive laws in the geotechnical engineering field for describing the behavior of a homogeneous porous material (Zoback, 2010). Figure 2-5 illustrates a schematic of these idealized constitutive laws along with a corresponding conceptual model. A *linear elastic* behavior is referred to a response where stress-strain are linearly proportional, and the deformation can be considered reversible. In such materials, stress can be expressed as a function of the current state of deformation only (linear elastic Hooke's law):

$$[K_s]\{d\mathbf{u}\} = \{d\mathrm{Q}\} \tag{1}$$

where Q is the forcing function (load), **u** is material's response, and $[\mathrm{K_s}]$ is system's stiffness matrix. For a linear material, $\mathrm{K_s}$ = constant. Models that characterize the behavior of materials with reversible deformations are referred to as elastic models (e.g. Cauchy Elastic model, Green Elastic model) (Desai et al., 1984). In case the porous rock is saturated with fluids, the behavior is of a *poroelastic* nature, where time-dependent deformations occur due to stress-pore pressure coupling. In fact, the stiffness of a fluid-

saturated rock depends upon the rate at which the external force is applied. Once stress is applied faster relative to dissipation of the excess pore pressures, the formation behaves in an un-drained manner and the rock will be relatively stiff. However, once the load is applied slowly enough so that the excess pore pressures generated as a result of compression of the soil skeleton have sufficient time to dissipate, the stiffness of the rock matrix will be the same as if no fluid was present. The coupled behavior of saturated porous formations is discussed in greater detail later in this chapter.

- A *viscoelastic* rock is one in which the deformation induced as a result of an applied stress or strain is rate dependent. In other words, the stress required to induce a certain magnitude of deformation depends on the apparent viscosity of the rock. The conceptual model presented in Figure 2-5 corresponds to a specific type of viscoelastic material known as a *standard linear solid*.
- An e*lastic-plastic* material is one that undergoes reversible (elastic) deformations at lower stresses, but will reach a yield point subsequent to which permanent damage is induced. The reloading path in these materials does not follow the original loading path past the yield point. Plastic behavior is therefore a function of history-dependent deformations (history of stress or strain states). The plastic behavior of various materials is idealized into different categories based on stress-strain behavior as illustrated in Figure 2-6. The behavior of unconsolidated porous formations during fluid injection can be described as elasto-plastic.

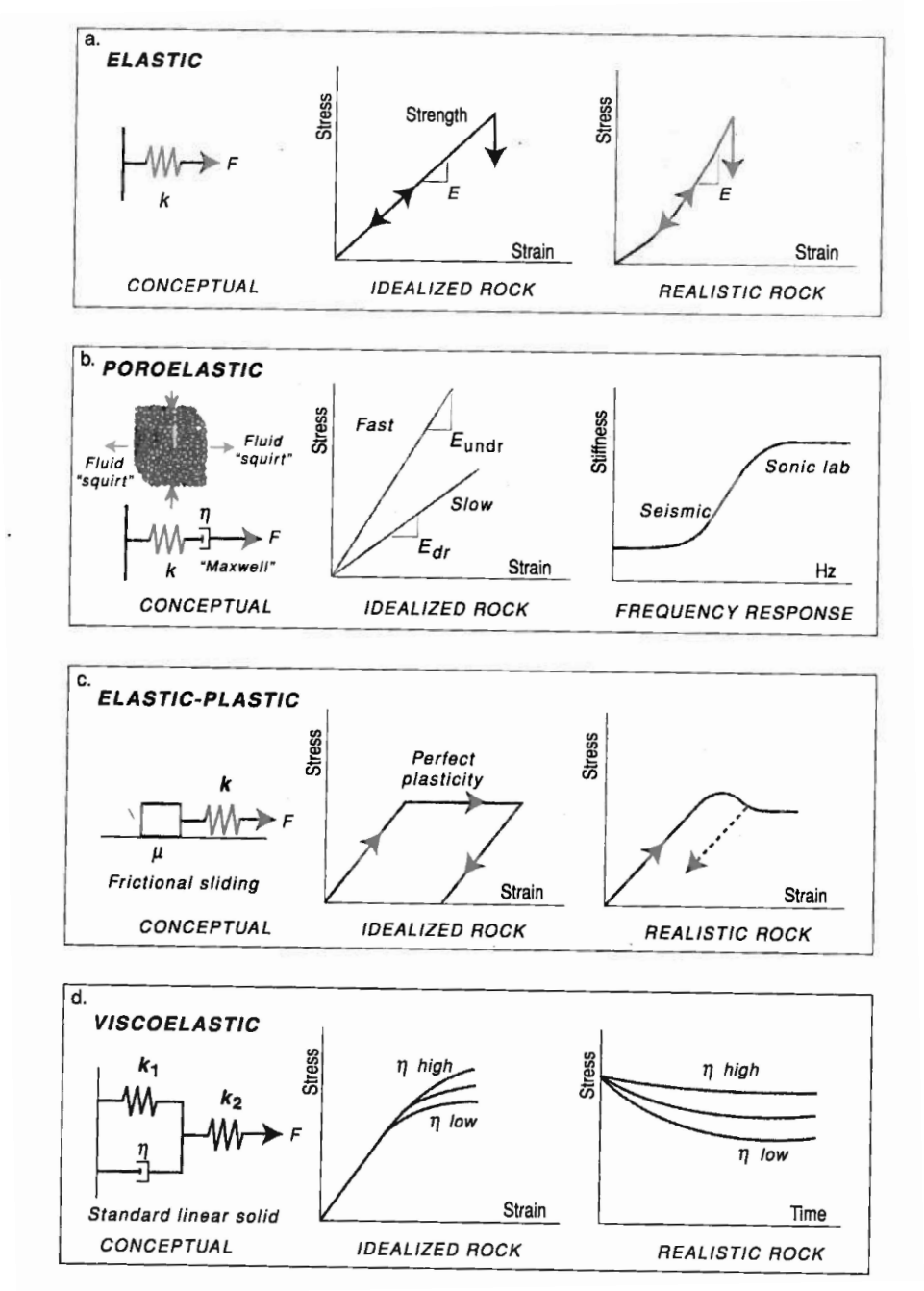

Figure 2-5. Schematic illustration of constitutive laws (Zoback 2010).

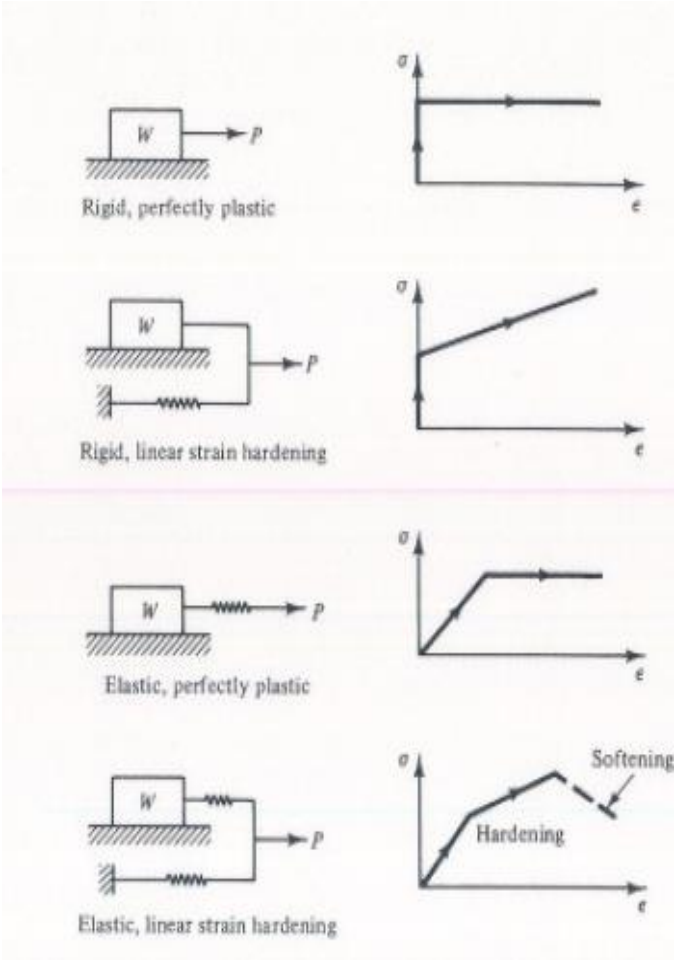

Figure 2-6. Idealized models for plasticity (Desai et al. 1984).

Plasticity theory is the study of the behavior of plastic materials. Two major aspects of plasticity theory are: yield criterion; and post-yield behavior (flow and hardening rules). Yield criterion is defined as the limit of elastic deformations/behavior that can be expressed using elastic stress-strain relationships. Typically, a yield function is described in terms of principal stresses and takes the form of ($f(\sigma_1, \sigma_2, \sigma_3) = 0$). For a homogeneous material, the same yield function is valid for every location within the material (Desai et al., 1984). Plastic strain increments can only occur if the stress state is on the boundary of the elastic domain. Stress states located past the yield function are not physically admissible (Gueguen et al., 2004). $f < 0$ implies that every solid particle inside the REV is strictly within the elastic domain. If $f = 0$, there is a region of the solid phase where the macroscopic stress state is located on the yield function (there might be parts of the REV still located in the elastic domain).

Ideally, the total induced strain can be decomposed into elastic and plastic components:

$$d\varepsilon = d\varepsilon^e + d\varepsilon^p \tag{2}$$

Where $d\varepsilon$ is the incremental total strain, $d\varepsilon^e$ is the incremental elastic strain, and $d\varepsilon^p$ is the incremental plastic strain component. From a physical point of view, variation of the residual stress at a grain-scale induced by plastic process is responsible for evolution of the plastic domain (Gueguen et al., 2004). This effect is referred to as "hardening". The plastic strain increment is assumed to be proportional to the deviatoric stress tensor (S_{ij}) at any instant during loading:

$$d\varepsilon_{ij}^p = \lambda S_{ij} \tag{3}$$

where λ is a nonnegative scalar factor which may vary during the loading history. Eq. 3 is also known as the flow rule.

2.4 Post-Yield Behavior

Once stresses reach the yield criterion, material undergoes plastic deformations; this is referred to as *plastic flow*. As a result of plastic flow, work hardening or strain hardening takes place in certain materials. Two hypothesis have been proposed to define the degree of hardening (Desai et al., 1984). One hypothesis offered by Hill (1950) is based on the concept of plastic work. The total work done per unit volume of a deformable body during a strain increment can be written as the summation of the elastic energy (W^e) which is recoverable, and the plastic work (W^P) which cannot be recovered. Hill (1950) suggested that hardening depends only on the plastic work, and is independent of the strain path. This also suggests that the resistance to further yielding is dependent only on the total plastic work that has been done on the material. Based on this hypothesis, the yield criterion can be written as shown in Eq. 4, which commonly referred to as the *work hardening hypothesis*:

$$f = f\left(\sigma_{ij}, W^P\right) \tag{4}$$

The other hypothesis assumes the plastic strain to be a measure of hardening. The yield function can thus be written as shown in Eq. 5, commonly referred to as the *strain hardening hypothesis*:

$$f = f\left(\sigma_{ij}, \varepsilon^P\right) \tag{5}$$

In the theory of plasticity, the direction of the local plastic strain vector is defined through a flow rule. This is achieved by assuming the existence of a plastic potential function, to which the incremental strain vectors are orthogonal. In this case, the plastic strain can be expressed as:

$$d\varepsilon_{ij}^{p} = \lambda \frac{\partial g}{\partial \sigma_{ij}} \tag{6}$$

where g is the plastic potential function, and λ is a positive scalar factor of proportionality and may depend on stress, strain and history of loading. This equation is commonly referred to as the *normality rule*. The normality rule indicates that the incremental plastic strain vector is normal to the yield surface; accordingly the plastic strain due to tangential plastic stress on the yield surface is zero. The plastic potential function and the yield function can be assumed to be the same for some materials. Such materials follow the *associative flow rule of plasticity*. However, for many geologic materials such as sand, the plastic potential function and the yield function are often different. These materials follow the *non-associative flow rule of plasticity* (Desai et al., 1984).

For an ideal plastic material, the yield function *f* does not move in the stress space. That is:

$$f = f(\sigma_{ij}) = \mathrm{k} \tag{7}$$

k in Eq. 7 is a constant that defines the yield limit.

Plastic models are suitable for describing mechanical properties of formations that undergo some degree of permanent, path-dependent deformations. Numerous plasticity models have been developed for various material types/behaviors (e.g. Von Mises for metals; Tresca for clay). Common plastic models applied for describing the behavior of geologic formations are: Mohr-Coulomb, Drucker-Prager, and Modified Cam-clay. Mohr-Coulomb is the most suitable model for characterizing the plastic behavior of unconsolidated sand formations, and is therefore adopted in this study.

2.5 Coupled Fluid-Soil Behavior

2.5.1 Poroelasticity

Solid-fluid coupling problems, also referred to as coupled deformation-flow problems, involve processes through which a change in the applied stress on the solid matrix will alter the hydraulic properties of the granular formation, inducing changes in the fluid pressure; and the change in the pore pressure will induce changes in the volume of the solid matrix. The earliest theory addressing solid-fluid coupling was Terzaghi's

consolidation theory (Biot, 1941, Terzaghi, 1923). Terzaghi introduced the concept of effective stress based on one-dimensional lab experiments:

$$\sigma'_{ij} = \sigma_{ij} + p\delta_{ij} \tag{8}$$

where σ'_{ij} is the effective stress on ij plane, p is the pore pressure, and δ_{ij} is the Kronecker delta. In this equation, compressive stresses are taken as a negative sign convention. Pore pressure is of central importance in reservoir geomechanics, and is defined as a scalar hydraulic potential acting within an interconnected pore space at depth (Zoback, 2007). The value of pore pressure is commonly described in relation to hydrostatic pressure, the pressure associated with a column of water from the surface to the depth of interest.

Biot generalized the concept of effective stress as follows:

$$\sigma'_{ij} = \sigma_{ij} - \alpha p\delta_{ij} \tag{9}$$

where α is the Biot coefficient defined as: $\alpha = 1 - K_b/K_s$ (K_b is the drained elastic bulk modulus and K_s is the bulk modulus of the solid phase). For soft materials, $K_b << K_s$, therefore, Terzaghi's effective stress concept is recovered. Biot (1941) also generalized Terzaghi's theory for three-dimensional consolidation, which was later referred to as the theory of poroelasticity by Greetsma (1966). Biot's theory for three-dimensional consolidation was developed based on the following assumptions: material is isotropic; stress-strain relationship is linear and reversible under final equilibrium conditions; induced strains are small; fluid is incompressible; and fluid flows within the porous media according to Darcy's law.

Poroelastic behavior describes two basic phenomena: solid to fluid coupling, which occurs when a change in the applied stress produces a change in the fluid pressure or fluid mass; and fluid to solid coupling, which occurs when a change in the fluid pressure or fluid mass produces a change in the volume of the porous material (Wang, 2000). Therefore, the mechanical response of the saturated porous media is characterized through coupled deformation-diffusion effects which result in a time dependent behavior of the geological formation (Detournay et al., 1988, Detournay et al., 1993).

Biot's fluid-filled porous material can be conceptually described as a coherent solid skeleton and a freely moving pore fluid, where the solid and fluid phase are fully connected. The "*kinematic*" quantities describing the motion of this conceptual model are: a solid displacement vector u_i which tracks the movement of the porous solid with respect to a reference configuration, and a specific discharge vector q_i which describes the motion of the fluid relative to the solid. Deformations and variations of the fluid content

with respect to an initial state can be described using "*strain*" quantities: strain tensor ε_{ij}, and variation of fluid content ω defined as the fluctuations of fluid volume per unit volume of porous material. The corresponding basic "*dynamic*" variables commonly applied to describe the causal forces that produce deformation are: total stress tensor σ_{ij}, and pore pressure p.

The volumetric response of a linear isotropic poroelastic material under drained conditions is typically described using pore pressure p as the coupling term. The elastic constituents describing the constitutive behavior of the poroelastic material will thus be those of the drained elastic solid. On the other hand, ω can be adopted as the coupling term, giving the volumetric response of the poroelastic material under undrained conditions. In this case, the elastic constituents will be those of the undrained elastic solid.

2.5.2 Poroplasticity

The theory of poroelasticity is restricted to calculating small, reversible strains, and therefore not suitable for describing injection of slurry into unconsolidated formations under high pressures (Gueguen et al., 2004). As a result of a mechanical loading σ_{ij} and/or fluid injection p, a strain ε_{ij} is induced, along with a fluid volume change of $v - v_0$. These two components can be split into a reversible component (elastic) and an irreversible component (plastic). This indicates that when unloading a REV to its initial state of σ_{ij_0} and p_0 through a purely reversible process (poroelastic), the initial state would have σ_{ij_0} and p_0. In case of poroplastic behavior, however, the unloaded state is characterized via ε_{ij}^p and a fluid volume fraction of $v - v_0 = \delta v^p$. Therefore:

$$\varepsilon_{ij} = \varepsilon_{ij}^e + \varepsilon_{ij}^p \tag{10}$$

$$v - v_0 = \delta v^e + \delta v^p \tag{11}$$

If every solid particle within the REV is experiencing elastic deformations ($f < 0$), the entire domain is elastic and poro-elasticity is applied to describe the coupled behavior. ($f = 0$) indicates that there are regions within the solid phase where the microscopic stress state lies on the boundary of the elastic domain; the REV therefore exhibits poro-elasto-plastic behavior.

2.6 Slurry Injection in Unconsolidated Formations

Injection of large volumes of slurry will significantly alter in situ stress distributions, inducing considerable deformations/dislocations and therefore extensively affecting the mechanical behavior of the media. As a

result of injection, brittle hard rocks typically fail in tension. Unconsolidated formations however, do not exhibit elastic-brittle behavior. Such formations are believed to experience different modes of failure under slurry injection, typically described as: tensile parting; shear failure, plane sliding (mode II) and tearing (mode III); and volumetric strain (Gil et al., 2003; Bohloli et al., 2006; Gil, 2005). Some studies have detected two drops in reservoir's pore pressure time histories during injection with constant injection rate (Olson et al., 2011). The first peak was believed to indicate initial parting due to tensile deformation. The second drop was suspected to take place when shear fractures start to form. Shear failure is generally considered to be the predominant failure mechanism in unconsolidated formations during hydraulic fracturing (Gil 2005; Zhai et al., 2005; Bohloli et al., 2006; Khodaverdian et al. 2009; Xu et al., 2010; Zhou et al. 2010; Olson et al. 2011).

Soft unconsolidated rocks exhibit high permeability, resulting in high leakoff rates during slurry injection. Results from numerous studies indicate that injection of slurry into soft compacting rocks induces plastic deformations, causing compaction in the sand volume surrounding the fracture. This will result in the formation of a shorter and wider fracture, with a more rounded tip compared to fractures induced in hard brittle formations. Creation of wider fractures may prevent the tip screen out (see section 1.1 for details on TSO) from occurring at the predicted time using linear elastic fracture mechanics (Abou-Sayed et al., 2004). Combination of the following characteristics has caused unconsolidated formations to behave entirely differently under slurry injection compared to hard rocks: non-linear rock behavior; large strains caused by low modulus rock; high fluid leak-off rates; non-elastic strains along fracture tip and fracture face; different failure mechanisms; and variations in the effective net pressure due to fluctuations in pore pressure (Gil et al., 2003). An example illustrating the unusual behavior of these formations is the Campos Basin project in Brazil, where produced water was reinjected into the unconsolidated Miocene reservoir (Pedroso et al., 2010). It was reportedly impossible to propagate fracture in one well even with injection pressure of 800 psi (5.5 MPa) above the estimated fracturing pressure. In another well however, an unexpected fracture gradient was attained.

Results from a triaxial test conducted on unconsolidated Athabasca oil sands suggested four possible modes of granular interaction under hydraulic pressure (Samieh et al., 1998): contact elastic deformation, rolling, sliding, and crushing (Figure 2-7). Crushing is not significant for unconsolidated formations during hydraulic fracturing; instead, grain parting is believed to account for fracturing in such media (Xu, 2010). Initiation of hydraulic fracture in particulate material as a result of fluid injection can actually be explained as the "*fluidization*" of the particle-fluid mixture, at which the loss of contact between particles occurs in all directions (Wu, 2006). Lab and field experiments indicate that the following factors significantly affect

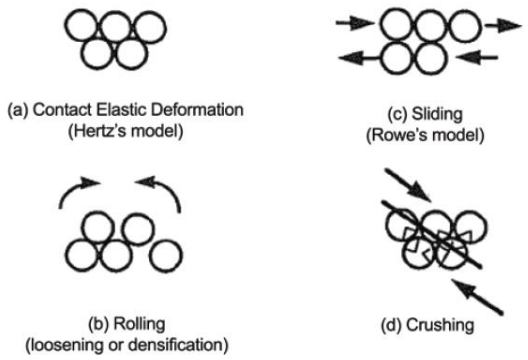

Figure 2-7. Different modes of granular interaction (Wong et al., 1993).

hydraulic fracture initiation/propagation in unconsolidated formations: in situ and confining stresses; k_o value; permeability; slurry type (viscosity); particle size distribution of slurry and reservoir formation; and cementation (Pedroso, 2010).

There are two major hypotheses in the literature describing the reason why huge volumes of solid slurry can be injected into soft formations: mixing/liquefaction; and creation of a disposal domain (Guo et al., 2008).

Liquefaction theory. Slurry's solid particles that are approximately the same size as the reservoir sand particles will be mixed with the formation sand, while smaller particles would fill in the voids between larger formation grains. Although both components (injected slurry, and in situ sand) might have similar porosities, the mixture porosity is proven to be much smaller. The process of intermixing is sometimes predicted using the definition of liquefaction: when effective stress approaches zero in a medium with little tensile resistance, the medium liquefies, increasing the native porosity and facilitating intermixing. This explanation is sometimes used to describe failure in such formations. Regions of induced fractures as a result of slurry injection have also been identified during lab/field experiments.

Disposal domain theory (Moschovidis et al., 1993; Keck 2002). Irregular injections cause multiple or complex fracture systems, modifying characteristics of the disposal domain. During shut in periods, fluids within fractures will leak off into the formation. Injected solids are retained near or inside fractures, reducing the effective exposed surface area, increasing local stresses, and inducing pressure build up and permeability impairment of the surrounding reservoir formation (Abou-Sayed et al., 2005). Plugging continues until pressures within the disposal domain reach a critical value, which is greater than the pressure required to further propagate the existing fracture or to re-fracture the formation.

The main agents causing formation damage in a slurry injection process are total suspended solids, bacteria and oil present within the slurry (Abou-Sayed et al., 2005). Slurry's solid phase is the most damaging component, and is therefore commonly considered to be the critical factor. The solid phase of the slurry is either trapped within the fracture (forming internal filter cake and causing highest damage), trapped within the formation (forming external filter cake), or travels freely through the formation (causing least damage) (Figure 2-8).

In order to better describe formation damage as a result of slurry injection, the reservoir may be divided into three zones: slurry/disposal domain, filter cake, and reservoir formation. The disposal domain is the zone where precipitation of slurry's solid phase takes place. Precipitation and the resulting filtration are the processes of solid-liquid separation. The concentration of solid particles increases in time especially on the boundaries between the disposal zone and reservoir formation, forming a packed bed referred to as the "*filter cake*" (Dong et al., 2009). The structure of the filter cake has a significant effect on important process parameters, such as pressure dissipation within the disposal domain. Filter cake damage occurs in two locations inside the induced fracture: along the fracture walls and at the fracture tip (Abou-Sayed et al., 2005). Previous studies suggest that the thickness of the filter is not even throughout the fracture: it is believed to be thicker near the wellbore and thinner near the fracture tip. The reason is that the accumulation of solid particles is a function of the volume of the leaked fluid and subsequent erosion, which vary at different locations of the fracture face. Figure 2-9 presents a fluid-fracture cross section obtained from injecting two colors of silicon fluid (black fluid following white). Results demonstrate a more active leak off at the tip compared to the fracture opening (Germanovich et al., 2012).

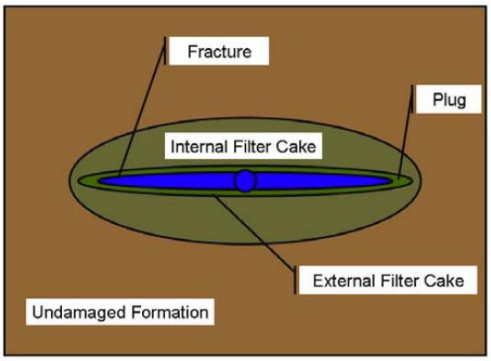

Figure 2-8. A schematic illustration of filter cake formation (Abou-Sayed et al. 2005).

Figure 2-9. Fluid-fracture cross-section indicating more active leak-off at fracture tip (Germanovich et al., 2012).

The motion of solid particles within the disposal domain is controlled by two types of forces: particle-particle forces (i.e., collision); fluid-particle forces (i.e., buoyancy, drag and lift forces) (Dong et al., 2009).

2.7 Classic Fracture Mechanics

The first significant analytical approach for describing fracture propagation mechanics was introduced by Griffith in the 1920s (Gil et al., 2003; Griffith, 1921). Griffith suggested that for an increment of crack extension, the change in potential energy of the deformation must be equal to the amount of energy required to create the new crack surface. The "Griffith Crack" is the basis of Linear Elastic Fracture Mechanics theory (LFEM) (Broek 1986), described as follows:

$$\frac{\partial U}{\partial a} = \frac{2\pi\sigma^2 a}{E} = 2G \tag{12}$$

where E is Young's modulus, σ is the far field stress, a is the characteristic fracture length (Figure 2-10), U is the elastic energy, and G is the elastic energy release rate also known as the crack driving force. The crack driving force is the loss of energy per unit of the new crack separation area formed during an increment of crack extension (Atkinson, 2013).

An essential assumption in developing LEFM theory is that no energy absorption takes place at the crack tip, and that the energy is used to elastically deform the rock or to further break the material and result in fracture propagation. Another intrinsic assumption in Griffith's analysis is that the deformation is infinitesimally small. The "Griffith Failure Criterion" also assumes that $\partial U/\partial a$ is a material constant; there is thus a critical value of stress (σ_c) introduced at which the material will experience instantaneous and brittle failure:

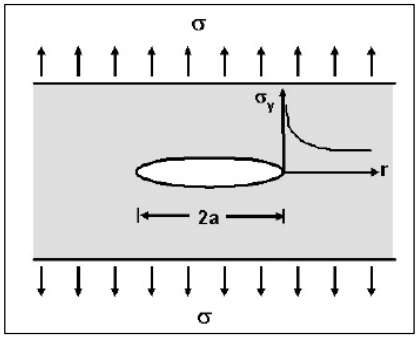

Figure 2-10. Griffith crack.

$$\sigma_c = \sqrt{\frac{E G_{Ic}}{\pi a}} \tag{13}$$

where G_{Ic} – referred to as the critical energy release rate – despite being a function of temperature and fracture geometry, is considered to be a material property.

Based on LEFM, for the plane strain conditions and mode I failure (tensile failure), stress and displacement fields around the crack tip are described as:

$$\sigma_{yy} = \frac{K}{\sqrt{2\pi r}} \tag{14}$$

$$\mathrm{u}_y(\text{displacement}) = \frac{K}{2\mu\sqrt{r/2\pi}} \tag{15}$$

where r is the distance of a given point to the fracture tip; and K is the stress intensity factor, which is the magnitude of the crack tip stress field for a particular mode in a homogeneous linear elastic material (Atkinson 2013). At failure onset, σ_c can be expressed in terms of a critical stress intensity factor, K_{Ic}, also known as fracture toughness. Failure is assumed to occur once stress defined from Eq. 14 exceeds the fracture toughness of the material/formation.

Based on LEFM, $r \rightarrow 0$ results in numerical singularity ($\sigma \rightarrow \infty$). Therefore, fracture tip propagation cannot be described using LEFM. This singularity of the elastic stress field indicates that there should be an inelastic region surrounding the crack tip where failure has occurred. A common approach in LEFM for calculating stress distributions around a propagating fracture is through determining the K-dominant region,

which is the area outside the plastic region, but with small *r* compared to fracture tip (Figure 2-11). Within this region, stresses/displacements are calculated using LEFM (Bruno et al. 2001).

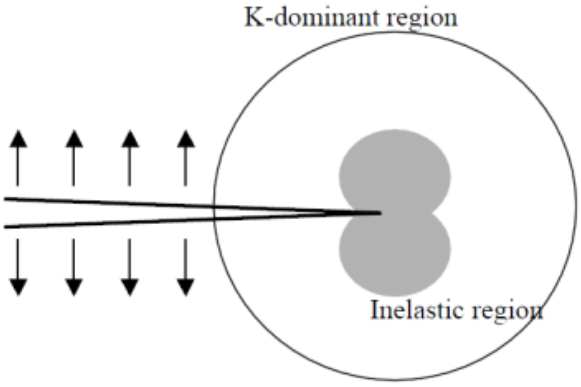

Figure 2-11. K-dominant region surrounding a crack tip outside near-tip inelastic zone (Bruno et al. 2001).

Griffith's work was expanded by Irwin (1948) and Orowan (1948) who recognized that the required energy for fracturing not only includes the surface energy density (γ), but also a dissipative energy (*d*) related to micro-cracking and plastic flow around the fracture tip (*d* is the larger term for most materials) (Bruno et al. 2001).

One of the first ground-breaking models developed for simulating hydraulic fracturing is the **PK** model established by Perkins et al. (1961) based on the LEFM. Later, Nordgren et al. (1972) presented the **PKN** model, which is an update of the PK model applicable for long fractures of limited height and elliptical vertical cross-section, and includes the effects of fluid loss. Khristianovic et al. (1955) and Geertsma et al. (1969) independently developed the so-called **KGD** model, a plane strain model for short fractures (Adachi et al. 2007). Sneddon (1946) presented the **radial or penny-shaped model** with constant fluid pressure applicable in homogeneous reservoir conditions where the injection region is practically a point source. Variations of the KGD, PKN, and radial models were routinely used for treatment designs as recent as 1990s and are only occasionally used nowadays as they have been mainly replaced by the **pseudo-3D (P3D)** models (Adachi et al., 2007). P3D models were developed in the 1980s, and extended the work of Simonson et al. 1978 to multiple layers, and are built on the basic assumption that the reservoir elastic properties are homogeneous, and averaged over all layers containing the fracture height. The planar 3D (PL3D) models were developed in the period of 1980 – 2000, in which it is assumed that the fracture footprint and the

coupled fluid flow equation are described by a 2D mesh of cells, typically a moving triangular mesh (Advani et al., 1990; Ben Naceur et al., 1990; Clifton et al., 1981; Clifton et al., 1991; Vandamme et al., 1989) or a fixed rectangular mesh (Barree, 1983; Siebrits et al., 2002), oriented in a (vertical) plane. There have also been attempts to model fully 3D hydraulic fractures (Carter et al., 2000) with limited success. The computational burden on such coupled systems is still excessive, even with today's powerful computational resources. A schematic of fracture geometry in the aforementioned hydraulic fracturing models is illustrated in Figure 2-12. The governing equations of these hydraulic fracturing models are: elasticity equations which express the mechanical response of the host reservoir to the loading imposed on the propagating fracture surfaces by the pressure due to the injectant; fluid flow equation, which expresses conservation of fluid mass; leak off term which describes the history-dependent loss of the injected fluid from the fracture into the porous reservoir, due to a positive pressure gradient between the fluid-filled fracture and the reservoir; proppant transport equation, describing the time-dependent distribution of the concentration of proppant in the fracture; and fracture growth condition that controls the rate and manner of growth of the hydraulic fracture, typically based on the assumptions of LEFM. These equations must be properly coupled in a stable, robust, and efficient manner.

a) PKN fracture geometry

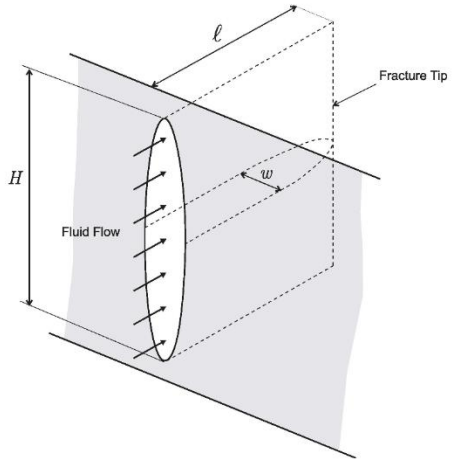

b) KGD fracture geometry

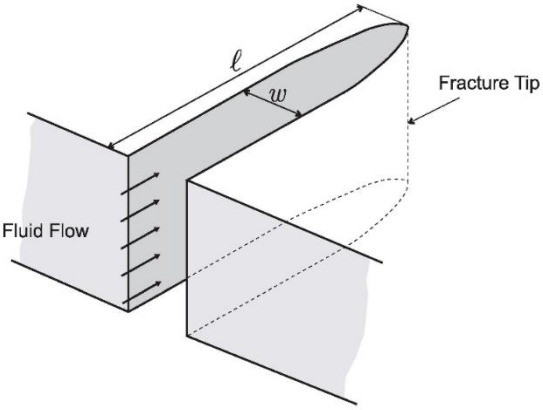

c) Radial Fracture Geometry

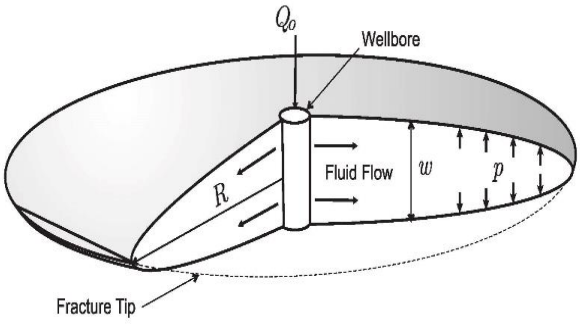

d) Cell-based pseudo-3D fracture geometry

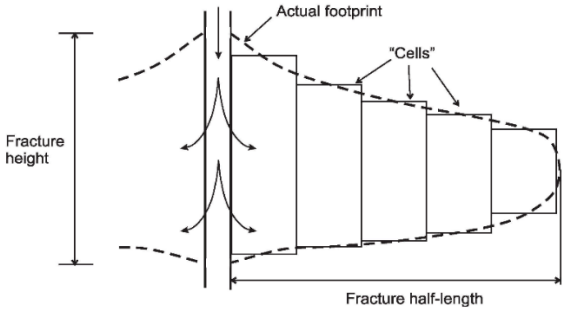

e) Planar 3D fracture geometry based on moving mesh system of triangular elements

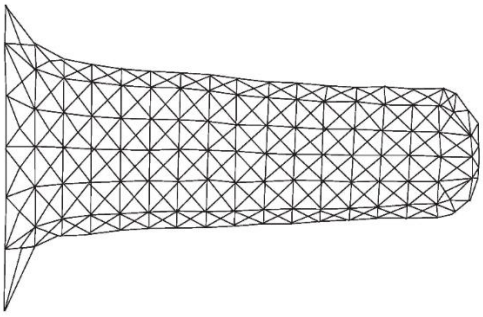

f) Planar 3D fracture geometry based on fixed system of quadrangular elements

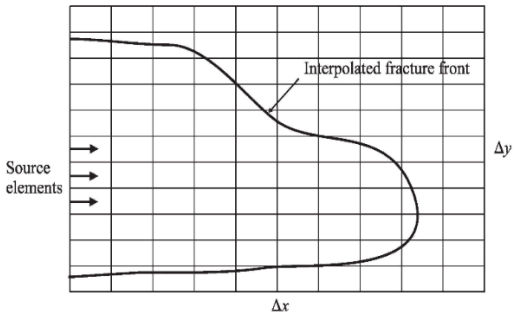

Figure 2-12. Schematic of fracture geometry for different LEFM based models (Adachi et al., 2007).

CHAPTER III

3. Research Objectives

Much effort has been devoted to evaluate coupled soil-fluid interactions in various geological formations triggered as a result of borehole excavation and production operations. However, with regards to injection operations carried out in weakly consolidated strata, practically no fundamental study has been conducted to evaluate the involved geomechanical processes. Peculiarities of such formations under injection flow results in the injection problem in to be highly challenging. Analytical formulation of the coupled behavior of granular media during injection remains intractable, and numerical computations are still challenging. Most previous work on injection processes are developed based on at least one of the following assumptions: uncoupled soil's response with respect to induced pore pressures; uncoupled pressure variations with respect to stresses/strains; elastic behavior of the reservoir rock; presence of a pre-existing fracture prior to injection initiation; plane strain conditions perpendicular to the injection current; independency of in situ conditions in the elastic domain from the plastic zone; and a constant stress pattern throughout the plastic domain. Thus far, practically no comprehensive study exists on the coupled geomechanical response of unconsolidated formations during injection prior to fracture initiation. Typically, runtime of a fully coupled flow-mechanical model is slow even with powerful computers. No in-depth study has thus been reported on the fully coupled response of a confined unconsolidated reservoir formation during a substantial period of injection cycle (or an entire transient state of an injection cycle). Assessments presented in the literature have been carried out at either very early times subsequent to injection initiation, or at steady state. Perhaps the most known work on poroelastic coupling in the content close to this research is that of Detournay and Cheng (1998).

CHAPTER 3. RESEARCH OBJECTIVES

The key objective of the current study is to develop new numerical and analytical tools to examine the time dependent coupled geomechanical processes involved during high pressure fluid injection – pressures high enough to induce plasticity yet not fracturing – in an isotropic, homogeneous unconsolidated porous layer confined with impermeable seal rocks. The permanent induced geomechanical effects of high pressure injection in such formations are also of interest. This research endeavor concentrates on fully penetrating wellbores. Unlike previous studies, impacts of vertical confinement governed by seal rock stiffness on the coupled reaction of the reservoir rock during injection are incorporated and closely evaluated. Variations in stresses, pore pressures, as well as principal planes are assessed throughout an entire transient state of an injection cycle, at steady state, and also during the shut-in period. Evaluations are carried out not only in the immediate area surrounding the injection wellbore but also at farther locations. The goal is to attain novel insights into geomechanics of failure (fracture) initiation during injection operations in various stress regimes, and to quantify the extent of the significant influence zone (plastic domain) induced surrounding an injection wellbore. The assessment carried out during the shut-in period enables evaluation of the permanent geomechanical effects induced within unconsolidated reservoirs as a result of injection operations.

CHAPTER IV

4. Methodology

The current study presents a multi-faceted effort to assess coupled poroelastic and poro-elasto-plastic processes involved during fluid injection from a fully penetrating vertical wellbore into a confined unconsolidated geological reservoir. This dissertation is composed of four main chapters: poroelasticity induced under lower injection pressures (Chapter 5); the poroelastic behavior and failure initiation in various stress regimes (Chapter 6); poro-elasto-plasticity in a confined unconsolidated sand layer under injection pressures that are high enough to induce plasticity, yet not fracturing in the porous medium (Chapter 7); and coupled rock-fluid interactions during the shut-in period and assessment of permanent induced effects of an injection cycle (Chapter 8).

Chapter 5 concentrates on the poroelastic time dependent geomechanical processes involved during fluid injection in confined geological reservoirs. New fully coupled analytical solutions are presented. Impacts of vertical confinement governed by the stiffness of the overburden layer on the coupled reaction of the reservoir rock during injection are incorporated in this dissertation for the first time. The Winkler spring model approximation is implemented to describe the response of the porous strata in the plane perpendicular to injection current. Pore pressures, stresses, strains, and displacements are derived as a function of the vertical confinement of the injection layer in addition to rock-fluid parameters. Next, a fully-coupled axisymmetric numerical model is developed to evaluate injection into a confined geological layer, taking into account interactions between the confining seal rock layers and the reservoir rock. The derived analytical solutions are compared against the numerical model developed in this study. A thorough sensitivity analysis is conducted next to examine the effect of vertical confinement, directly governed via seal rock stiffness, on geomechanics of injection in unconsolidated reservoirs.

Chapter 6 contains a comprehensive assessment of stress modifications surrounding an injection borehole using the analytical solutions derived in Chapter 5. The goal is to evaluate the pre-failure behavior of a confined unconsolidated sand layer under various stress regimes. To obtain a better insight into failure initiation, a comprehensive sensitivity analysis is conducted on impacts of vertical confinement (seal rock stiffness) as well as rock-fluid characteristic parameters on principal planes.

Chapters 7 includes evaluation of the poro-elasto-plastic behavior of an isotropic, homogeneous, unconsolidated soil layer confined by stiff seal rocks under pressures high enough to induce plasticity yet not fracturing in the porous medium. The first part of Chapter 7 involves a new axisymmetric fully coupled numerical model for wellbore injection in a confined unconsolidated reservoir. Multiple simulations with different geometry and mesh settings have been carried out to ensure independence of the qualitative observations with respect to the chosen geometry and mesh dimension. Results from one representative model are presented in this dissertation. A comprehensive assessment of pore pressures, stress patterns, and failure planes is conducted throughout the entire transient period of an injection cycle. The results not only provide a good insight into geomechanics of injection operations below fracturing pressures, but also allow evaluation of fracture initiation in unconsolidated formations under plane strain settings. Pore pressure distributions obtained from the numerical models are compared against the commonly adopted uncoupled pore pressure equation (for steady state), to evaluate applicability and limitations of this simplified theoretical relation during plastic state under plane strain conditions. The second part of Chapter 7 includes derivation of new poro-elasto-plastic analytical solutions for all three stress/strain components as a function of an arbitrary pore pressure function. The approach adopted for analytical derivations is similar to that of Risnes et al. (1982), where knowledge of principal planes is a priori, as yield functions are commonly expressed in terms of principal stresses. The study, however, considered conditions of fluid production. Unlike Risnes et al. (1982) who adopted elastic solutions to define principal planes in the plastic domain thus disregarding plasticity impacts on in situ conditions in the elastic zone, results from the fully coupled numerical models are directly adopted to determine principal planes in this study. Finally, a novel methodology is proposed based on which new weakly-coupled poro-elasto-plastic analytical solutions are derived for all three stress/strain components within plastic and elastic domains. Analytical solutions are verified against the fully coupled numerical models presented in the first part of Chapter 7.

Chapter 8 concentrates on the coupled post-injection behavior of unconsolidated sandstone reservoirs confined with stiff seal rock layers. The numerical model developed and presented in Chapter 7 is implemented for the post-injection evaluation. Injection is ceased once steady state flow condition is reached and a significant plastic domain has already been induced surrounding the wellbore in the reservoir

formation. Pore pressure dissipation, stress variations, and the transition behavior to an elastic state of the plastic domain surrounding the injection wellbore are closely evaluated during the shut-in period. Results present an original insight into the permanent geomechanical effects of injection operations in such formations.

An overview of the research methodology adopted in this study is presented in Figure 4-1.

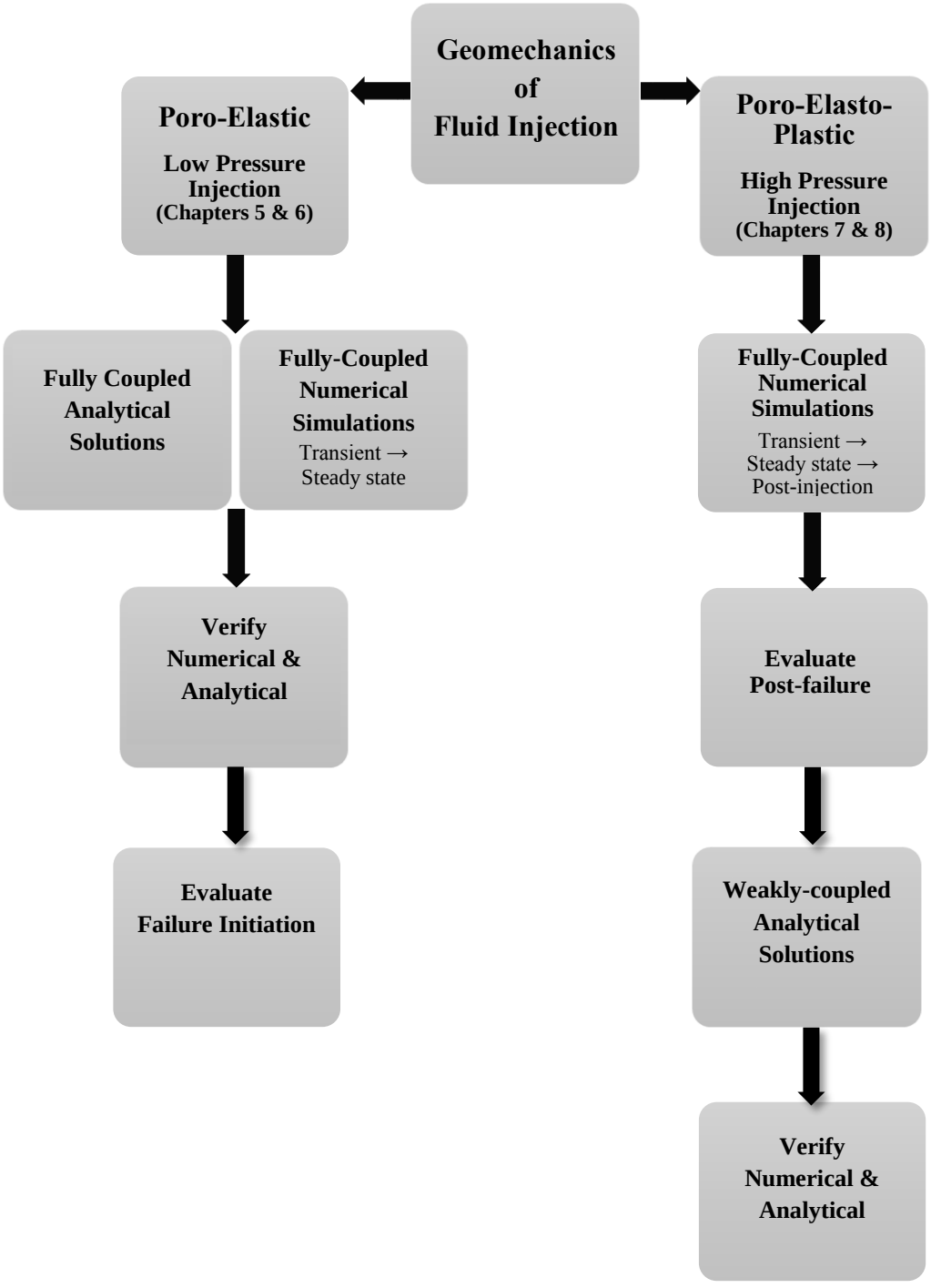

Figure 4-1. Overview of the research methodology.

CHAPTER V

5. Poroelastic Variations

This chapter concentrates on the time dependent poroelastic variations induced in a confined unconsolidated sand layer during radial fluid injection from a fully penetrating vertical wellbore. First, new closed-form analytical solutions are derived. Unlike previous studies, impacts of vertical confinement governed by the stiffness of the overburden layer on the coupled reaction of the injection layer are incorporated via implementation of the Winkler model. To better evaluate the degree of the impact of seal rock stiffness on coupled behavior of geological reservoirs under injection, solutions for two extreme cases are derived and presented as well: a reservoir formation confined by seal rocks with large stiffness values (mechanically fixed boundaries); and a reservoir formation confined with seal rocks exhibiting minimal stiffness (mechanically free boundary). A new expression is derived for the "consolidation coefficient", a common parameter which appears in all standard pore pressure formulations. The new equation is compared in this chapter with some well-known equations presented in the literature.

Next, a new tightly-coupled axisymmetric numerical model is developed to evaluate radial injection from a fully penetrating vertical wellbore into a confined geological reservoir, incorporating the interactions between the reservoir formation and the neighboring seal rock layers. Results from the numerical model are then compared against the new closed-form analytical solutions for verification. A comprehensive sensitivity analysis is carried out to examine the impacts of vertical confinement on the geomechanical parameters which represent the response of the porous medium during fluid injection.

The final part of this chapter includes a brief section on determination of an appropriate far-field reservoir extension for an optimum numerical modeling using the derived analytical solutions.

Reservoir behavior is characterized under fully drained circumstances and adopting pore pressure as the coupling term for analytical formulations. This is a fairly acceptable assumption as injection operations are commonly conducted in naturally fractured or weakly consolidated formations, and are performed in a cyclic routine with periods of shut-in and pre-flush which facilitate drainage. Injectant is assumed to be a Newtonian fluid. The effect of gravity is not incorporated in this work for simplicity. Compression stresses (strains) are taken as a negative sign convention all throughout this study.

5.1 Fully-Coupled Analytical Solutions

5.1.1 Flexible Seal Rocks

The fundamental equations for describing the coupled behavior of geological reservoirs under injection are constitutive, flow, and force balance relations, given as follows. Analytical solutions are obtained for an isotropic, homogeneous semi-finite medium under drained conditions. The coupling term adopted in this study is therefore pore pressure *p*. Solutions are derived for point source injection in a cylindrical coordinate system. Soil's characteristic parameters are presumed not to vary in time during injection. Darcy's law is considered to be valid.

Constitutive Relations. With the convention for compressive stresses (strains) taken as negative, stresses in a cylindrical coordinate system at any given location with radial distance *r* from injection source at time *t* are written as:

$$\Delta\sigma_{ij}^{e} = \frac{E}{1+v}\left[\varepsilon_{ij}^{e} + \frac{v}{1-2v}\left(\varepsilon_{kk}^{e}\delta_{ij}\right)\right] - \alpha p\delta_{ij} \tag{16}$$

where $\Delta\sigma_{ij}^{e}$ is the total induced stress on *ij* plane in the elastic state; ε_{ij}^{e} is the elastic strain component; subscripts i and j correspond to radial, tangential, and vertical directions; *p* is the induced pore pressure; E is Young's Modulus of the formatin; v is soil's Poisson Ratio; α is the Biot coefficient; and δ is Kronecker delta.

Flow Equations. Variations in in situ water content during injection generates both strains and pore pressures in the porous medium. Variations in water content ($\boldsymbol{\omega}$) in terms of volumetric strain ($\boldsymbol{\varepsilon}$)and *p* for any given location in time is given as (Biot 1941, Detournay et al. 1988):

$$\omega = \alpha\varepsilon + p/M \tag{17}$$

where *M* is the Biot modulus defined as the ratio between fluid Bulk modulus (K_f) and porosity (*n*).

The relation between injection rate (*q (m/sec)*) and pore pressures is described using the Darcy law equation:

$$q_i = -k\frac{\partial p}{\partial x_i} \tag{18}$$

where *k* is the permeability coefficient, otherwise referred to as the mobility coefficient ($m^2/(Pa.sec)$).

Conservation of mass specifies that the rate of water content entering a soil element should be equal to the volume of the fluid entering per second through the surface of the element (Eq. 19).

$$\frac{\partial \omega}{\partial t} = -\frac{\partial q_x}{\partial x} - \frac{\partial q_y}{\partial y} - \frac{\partial q_z}{\partial z} \tag{19}$$

Combining Eqs. 18 and 19 result in the following differential relation:

$$\frac{\partial \omega}{\partial t} = k\nabla^2 p \tag{20}$$

Differentiating Eq. 17 with respect to time and combining it with Eq. 20 gives the following $p - \varepsilon$ relation:

$$k\nabla^2 p - \frac{1}{M}\frac{\partial p}{\partial t} = \alpha\frac{\partial \varepsilon}{\partial t} \tag{21}$$

Force Balance Equations. Force balance in the horizontal plane results in the following relation between stress components in radial and tangential directions:

$$\frac{\partial \sigma_{rr}}{\partial r} + \frac{\sigma_{rr} - \sigma_{\theta\theta}}{r} = 0 \tag{22}$$

Due to formation dilation, forces are generated on the seal rock – reservoir interfaces perpendicular to injection (Figure 5-1). The formation's elastic response in this plane can be described using the Winkler soil model. Physically, Winkler's idealization of the soil medium consists of a system of mutually independent spring elements (Selvadurai 1979). It is assumed that the deflection of the soil medium at a given point is directly proportional to the stress applied at that point, and independent of stresses applied at other locations. An important feature of this soil model is that the displacement occurs immediately under the loaded area. Vertical displacement (Δ) of an area experiencing a uniform pressure (σ_{zz}) from a semi – infinite, homogeneous, isotropic mass with linear behavior expressed via Winkler model is given as shown in Eq. 23:

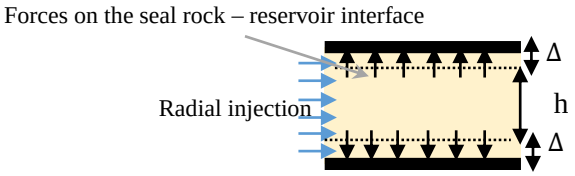

Figure 5-1. Normal displacements induced on seal rock interfaces due to radial injection.

$$\Delta = \frac{\sigma_{zz}}{K_n} \tag{23}$$

where K_n is the overburden's normal stiffness (*Pa/m*), otherwise referred to as the modulus of subgrade reaction in the literature. The Winkler's soil model has widely and effectively been employed in a host of engineering problems: soil-foundation interactions; analysis of floating structures (e.g. bridges, ice sheets) (Wyman, 1950; Meyerhof, 1960; Hutter, 1975); stress analysis of cemented lap joints (Reissner and Goland, 1944; Cornell, 1953); investigation of the state of stress at the tip of a crack in an elastic continuum (Goodier and Kanninen, 1966; Kanninen, 1973); and analysis of cracked plates (Selvaduri 1977, 1978).

Taking into account displacements from the two seal rock interfaces surrounding the reservoir formation (Figure 5-1), the strain along the vertical plane is derived to be:

$$\overline{\varepsilon_{zz}} = \frac{2\Delta}{h} \tag{24}$$

where h = reservoir thickness. Combining Eqs. 23 and 24 gives the following relation in the vertical plane:

$$\Delta\sigma_{zz} = -\overline{\varepsilon_{zz}}K \tag{25}$$

where $\Delta\sigma_{zz}$ is the total induced stress component in the vertical plane, and K is referred to as the overburden Winkler stiffness parameter, defined as $K_n h/2$.

Geomechanical Parameters in Terms of Pore Pressure. Combining Eqs. 16 and 25 after some manipulations gives the following relation for the vertical strain component in terms of horizontal strains and pore pressure:

$$\overline{\varepsilon_{zz}^e} = N(\varepsilon_{rr}^e + \varepsilon_{\theta\theta}^e) - \frac{\alpha}{F}p \tag{26}$$

where N and F *(Pa)* are referred to as material constants in this study and are derived to be:

$$N = -\frac{Ev}{K(1+v)(1-2v) + E(1-2v) + Ev} \tag{27.a}$$

$$F = -\frac{K(1+v)(1-2v) + E(1-2v) + Ev}{(1+v)(1-2v)} \tag{27.b}$$

Substituting constitutive expressions into the force balance equation (Eq. 22), and replacing vertical strains with Eq. 26 results in the following relation between horizontal strains and the induced pore pressure:

$$\frac{E}{1+v}\left\{\frac{\varepsilon_{rr}^{e}}{\partial r}\left[1+\frac{v}{1-2v}(1+N)\right] + \frac{\varepsilon_{\theta\theta}^{e}}{\partial r}\frac{v}{1-2v}(1+N) + \frac{1}{r}(\varepsilon_{rr}^{e} - \varepsilon_{\theta\theta}^{e})\right\} = \alpha\frac{\partial p}{\partial r}\left[1+\frac{Ev}{(1+v)(1-2v)F}\right] \tag{28}$$

Total horizontal strains are described in terms of radial displacements (u_r) as follows:

$$\varepsilon_{rr}^{T} = \frac{du_r}{dr} \tag{29.a}$$

$$\varepsilon_{\theta\theta}^{T} = \frac{u_r}{r} \tag{29.b}$$

Elasticity theory suggests total strains to be equivalent to the elastic strain components, as the plastic components are zero in the elastic state. Thus, substituting strains in Eq. 28 with the equivalent radial displacement terms (Eq. 29.a and Eq. 29.b) leads to the following $u_r - p$ relationship:

$$\frac{\partial^2 u_r}{\partial r^2} + \frac{1}{r}\frac{\partial u_r}{\partial r} - \frac{u_r}{r^2} = \alpha Y\frac{\partial p}{\partial r} \tag{30}$$

where

$$Y = \frac{(1+v)(1-2v)F + Ev}{[1-2v+v(N+1)]FE} \tag{31}$$

is referred to as "*displacement multiplier"* in this study, and has the units of (*1/Pa*). Integration of the above differential equation and implementing boundary conditions at the far field which dictate zero induced pore pressure and displacement for $r \to \infty$, leads to the following relation between $u_r - p$.

$$\frac{\partial u_r}{\partial r} + \frac{u_r}{r} = \alpha Y p \tag{32}$$

Eq. 32 can also be written in terms of horizontal strains as demonstrated in Eq. 33.

$$\varepsilon_{rr}^{e} + \varepsilon_{\theta\theta}^{e} = \alpha Y p \tag{33}$$

The solution to Eq. 32 in terms of pressure for point source injection ($r_o \rightarrow 0$) is derived to be:

$$\mathrm{u}_r(r,t) = \frac{\alpha Y}{r} \int_{r_0}^{r} r p(r) dr \tag{34}$$

Elastic strain components as a function of pore pressures can be computed via the following relations which are derived using Eqs. 26, 29.a, 29.b, and 34:

$$\varepsilon_{rr}^{e} = -\frac{1}{r^2} \alpha Y \int_{r_0}^{r} r p(r) dr + \alpha Y p(r) \tag{35.a}$$

$$\varepsilon_{\theta\theta}^{e} = \alpha Y \frac{1}{r^2} \int_{r_0}^{r} r p(r) dr \tag{35.b}$$

$$\overline{\varepsilon_{zz}^{e}} = \alpha p(r)(NY - \frac{1}{F}) \tag{35.c}$$

Stress – pore pressure relations are computed via substituting Eqs. 35.a, 35.b, and 35.c into constitutive formulas. Induced total stresses in the cylindrical coordinate system as a function of an arbitrary pore pressure function are derived to be:

$$\Delta\sigma_{rr}^{e} = \frac{E}{1+v}\left[-\frac{1}{r^2}\alpha Y \int_{r_0}^{r} r p(r) dr + \alpha Y p(r)\right] + \frac{Ev}{(1+v)(1-2v)} \alpha p(r) \left(Y + NY - \frac{1}{F}\right) - \alpha p(r) \tag{36.a}$$

$$\Delta\sigma_{\theta\theta}^{e} = \frac{E}{1+v}\alpha Y \frac{1}{r^2} \int_{r_0}^{r} r p(r) dr + \frac{Ev}{(1+v)(1-2v)} \alpha p(r) \left(Y + NY - \frac{1}{F}\right) - \alpha p(r) \tag{36.b}$$

$$\Delta\sigma_{zz}^{e} = \alpha p(r) \left[\frac{E}{1+v}\left(NY - \frac{1}{F}\right) + \frac{Ev}{(1+v)(1-2v)}\left(Y + NY - \frac{1}{F}\right) - 1\right] \tag{36.c}$$

Thus far, new general solutions are obtained for displacements, stress, and strain components induced during radial injection based on an arbitrary pore pressure function, incorporating impacts of vertical confinement. In order to compute these geomechanical parameters, in situ pore pressures must be determined in time during injection.

Pore Pressure Equation. The general $p - \varepsilon$ relation is given in Eq. 21, which has already been derived and widely implemented in previous studies (Detournay and Cheng, 1988). Substituting the vertical strain component in Eq. 21 with Eq. 26 results in the following differential relation for pore pressures in terms of horizontal strains:

$$k\left(\frac{\partial^2 p}{\partial r^2}+\frac{1}{r}\frac{\partial p}{\partial r}\right)-\frac{1}{M}\frac{\partial p}{\partial t}=-\frac{\alpha^2}{F}\frac{\partial p}{\partial t}+\alpha(N+1)\frac{\partial}{\partial t}(\varepsilon_{rr}^{e}+\varepsilon_{\theta\theta}^{e}) \tag{37}$$

Pore pressures in this relation can be uncoupled from strains when replacing the horizontal strain components with the equivalent pressure term via Eq. 33. The following relation is thus obtained for pore pressures during injection in a reservoir with flexible seal rocks:

$$\frac{\partial^2 p}{\partial r^2}+\frac{1}{r}\frac{\partial p}{\partial r}=c\frac{\partial p}{\partial t} \tag{38}$$

where

$$c=\frac{1}{k}\left[\frac{1}{M}+\alpha^2\frac{(N+1)YF-1}{F}\right] \tag{39}$$

is in fact the inverse of the consolidation coefficient with units of (sec/m^2).

Assuming a point source injection ($r_o \rightarrow 0$), after some manipulations it can be demonstrated (Appendix 1) that the transient pore pressure solution for Eq. 38 is derived to be:

$$p=CE_1\left(\frac{cr^2}{4t}\right) \tag{40}$$

where $E_1(X)=\int_X^{\infty}\frac{e^{-V}}{V}dV$ is the exponential integral, and C is the integral constant derived to be $Q_o/(4\pi hk)$ via applying boundary conditions at the wellbore (Q_o (m^3/sec) being the total injection rate). It is important to further emphasize that the pore pressure solution is obtained for point source injection ($r_o \rightarrow 0$). Thus, adopting Eq. 40 in order to describe wellbore injection ($r_o \rightarrow r_w$ wellbore radius) brings about a delay in the pore pressure build up on the wellbore interface (Q_{r_w}). This postponement is a function of c, r_w, and t in an exponential manner as demonstrated in the following expression.

$$\frac{Q_{r_w}}{Q_o}=e^{\left(\frac{-cr_w^2}{4t}\right)} \tag{41}$$

An empirical correction can thus be incorporated in the derived analytical expression to compensate for this discrepancy. However, a closer evaluation indicates that Q_{r_w} quickly approaches Q_o due to the exponential relation between the two parameters, as r_w soon becomes trivial compared to t over time. Accordingly, point-source solutions can very well be executed to describe borehole injection in a geological formation.

Summary of General Poroelastic Solutions. Specific solutions for induced stresses, strains, and displacement are obtained via substituting the pore pressure solution (Eq. 40) into the corresponding derived expressions. The closed-form analytical solutions obtained for point source injection in a confined geological reservoir are:

$$\mathrm{u}_r = \frac{\alpha Y Q_o}{8\pi Hk} r \left[E_1(X) - \frac{1}{X}(\exp(-X) - 1) \right] \tag{42}$$

$$\varepsilon^e_{rr} = \frac{\alpha Y Q_o}{8\pi Hk} \left[E_1(X) + \frac{1}{X}(\exp(-X) - 1) \right] \tag{43.a}$$

$$\varepsilon^e_{\theta\theta} = \frac{\alpha Y Q_o}{8\pi Hk} \left[E_1(X) - \frac{1}{X}(\exp(-X) - 1) \right] \tag{43.b}$$

$$\varepsilon^e_{zz} = \frac{\alpha Q_o}{4\pi Hk} \left(NY - \frac{1}{F} \right) E_1(X) \tag{43.c}$$

$$\Delta\sigma'^e_{rr} = \frac{E\alpha Y Q_o}{8\pi Hk(1+v)} \left[E_1(X) + \frac{1}{X}(\exp(-X) - 1) \right] + \frac{Ev\alpha Q_o \left(Y + NY - \frac{1}{F} \right)}{4\pi Hk(1+v)(1-2v)} E_1(X) \tag{44.a}$$

$$\Delta\sigma'^e_{\theta\theta} = \frac{E\alpha Y Q_o}{8\pi Hk(1+v)} \left[E_1(X) - \frac{1}{X}(\exp(-X) - 1) \right] + \frac{Ev\alpha Q_o \left(Y + NY - \frac{1}{F} \right)}{4\pi Hk(1+v)(1-2v)} E_1(X) \tag{44.b}$$

$$\Delta\sigma'^e_{zz} = \frac{E\alpha Q_o}{4\pi Hk} E_1(X) \left[\frac{\left(NY - \frac{1}{F} \right)}{(1+v)} + \frac{v}{(1+v)(1-2v)} \left(Y + NY - \frac{1}{F} \right) \right] \tag{44.c}$$

where $X = cr^2/(4t)$. It can easily be demonstrated that the aforementioned fully coupled analytical solutions are not singular near the injection source ($r \rightarrow 0$). The main assumptions behind these poroelastic solutions are once again presented for further emphasis and clarification of the limitations of these equations: the media is semi-infinite with isotropic and homogeneous characteristic parameters, injectant and formation's characteristic parameters remain constant in time, solutions are obtained for a cylindrical coordinate system, injection is implemented as a point source, injectant is a Newtonian fluid, Darcy law is valid, isothermal conditions stand.

5.1.2 Seal Rocks with Minimal Stiffness

The governing equations applied to examine injection in a reservoir formation confined by seal rocks with minimal stiffness are identical to those of the general case. Substituting zero stiffness ($K_n=0$) in aforementioned relations results in solutions for this case scenario. Solutions will thus be identical to those

already derived (Eqs. 35 – 44). The material constants, being a direct function of K_n will however be as follows:

$$N = -\frac{v}{1-v} \tag{45.a}$$

$$F = -\frac{E(1-v)}{(1+v)(1-2v)} \tag{45.b}$$

5.1.3 Fixed Boundaries.

Particularly stiff seal rocks ($K_n \rightarrow \infty$) represent fixed boundaries. All governing equations applied thus far are still valid in this case senario. Coupled stress, stain, displacement and pore pressure solutions are thus identical to those derived for the general case. Implementing $K_n \rightarrow \infty$ results in the material constants to be: $N=0$, and $F \rightarrow \infty$. Substituting these terms in Eq. 26 results in the vertical component of the strain to approach zero (plane strain), which is expected, as seal rocks in this case scenario are fixed and no vertical movement is allowed. Moreover, since the thickness of geological reservoirs is insignificant compared to their lateral extension, internal vertical deformations will be negligible when compared with horizontal deformations induced under radial injection.

The inverse of the consolidation coefficient "c" for the plane strain condition will be as follows:

$$c = \frac{1}{k}\left[\frac{1}{M} + \alpha^2 \frac{(1+v)(1-2v)}{(1-v)E}\right] \tag{46}$$

The solutions derived for the general case scenario (flexible seal rocks) still stand for the plane strain condition.

5.2 Consolidation Coefficient

In this study, a new expression is derived for the generalized consolidation coefficient (given by equation 39) based on: vertical confinement of the reservoir (overburden stiffness), solid and fluid compressibility, and coupling of flow-displacements. This equation agrees with the general format proposed by Biot (1941). Different expressions have been previously presented in the literature for computing c corresponding to various circumstances. The following paragraphs investigate Eq. 39 derived in this study versus some well-known equations presented in the literature.

Carter and Booker (1982) derived *c* for a limiting case of incompressible fluids and solid particles. The proposed consolidation coefficient is described as a function of Poisson's ratio, fluid unit weight, hydraulic conductivity, and shear modulus of the formation (*G*). Under this condition:

$$c = \frac{1}{2Gk}\frac{(1-2v)}{(1-v)} \tag{47}$$

Detournay and Cheng (1988) presented the consolidation coefficient in terms of drained as well as undrained soil parameters for plane strain conditions, where the coupling effects of soil-fluid interactions are not accounted for.

$$c = \frac{1}{2Gk}\left[\frac{9(1-2v_u)(v_u-v)}{B^2(1+v_u)^2(1-2v)}\right] \tag{48}$$

where v_u is the undrained Poisson's ratio. Eq. 48 can be described in terms of α:

$$c = \frac{1}{2Gk}\left[\frac{3\alpha(1-2v_u)}{B(1+v_u)}\right] \tag{49}$$

Substituting $\frac{3(1-2v_u)}{2G(1+v_u)}$ in Eq. 49 with the equivalent term for the undrained bulk modulus ($\frac{1}{K_u}$), and replacing $\frac{BK_u}{\alpha}$ with M results in the following expression for *c* proposed by Detournay and Cheng (1988) in terms of drained parameters:

$$c = \frac{1}{kM} \tag{50}$$

Eq. 50 does not contain the second term in Eq. 39, as the coupling effects of soil-fluid interactions have not been accounted for.

Rice and Cleary (1976) presented a more generalized *c* in terms of drained and undrained soil parameters, incorporating coupling effects.

$$c = \frac{1}{2Gk}\left[\frac{(1-2v)}{(1-v)}\right]\left[\frac{9(1-v_u)(v_u-v)}{B^2(1+v_u)^2(1-2v)}\right] \tag{51}$$

Eq. 51 can be rewritten as:

$$c = \frac{1}{kM}\left[\frac{(1-2v)}{(1-v)}\right]\left[\frac{(1-v_u)}{(1-2v_u)}\right] \tag{52}$$

Eq. 52 reverts to Eq. 50 under drained conditions, as $v_u \rightarrow v$.

Next, the equivalent diffusion constant obtained in the current study (Eq. 39) is compared with some well-known equations available in the literature: Rice and Cleary (1976), Carter and Booker (1982), and Detournay and Cheng (1988). The aforementioned equations available on the diffusivity constant are in fact obtained for production flow under plane strain conditions. These equations have been widely adopted in the literature to evaluate various soil-fluid problems including injection operations (e.g. Abousleiman and Chen, 2010). The diffusivity constant in the current study is expressed through traditional poroelastic parameters as well as the relative stiffness of reservoir and seal rocks. This equation agrees with the general format proposed by Biot (1941). Figure 5-2 presents *c* given by the aforementioned studies for an incompressible fluid. Due to the explicit structure of the previous solutions which are directly governed by the shear modulus of the reservoir formation (*G*), *c* in Figure 5-2 is plotted versus *G*. The graph demonstrates identical curves obtained from the definitions of Rice and Cleary (1976), and Detournay and Cheng (1988). The shaded area on the graph marks the range of the proposed solution (Eq. 39) based on the vertical confinement setting ($0.0 < K < \infty$). The lower bound of the proposed solution – which corresponds to stiff seal rocks (plane strain, $K \rightarrow \infty$) – is in fact identical to the equation proposed by Carter and Booker (1982). Figure 5-2 clearly illustrates the significance of incorporating the characteristics of vertical confinement in reservoirs with lower elastic moduli. This impact decreases with increase in the reservoir's elastic moduli. Eventually, all the aforementioned solutions yield to a similar value, independent of the vertical confinement setting. A higher c value implies a lower rate of pore pressure generation in time. In other words, under stiffer seal rocks or a lower c value, pore pressures generate at a higher rate specifically in formations with lower elastic moduli.

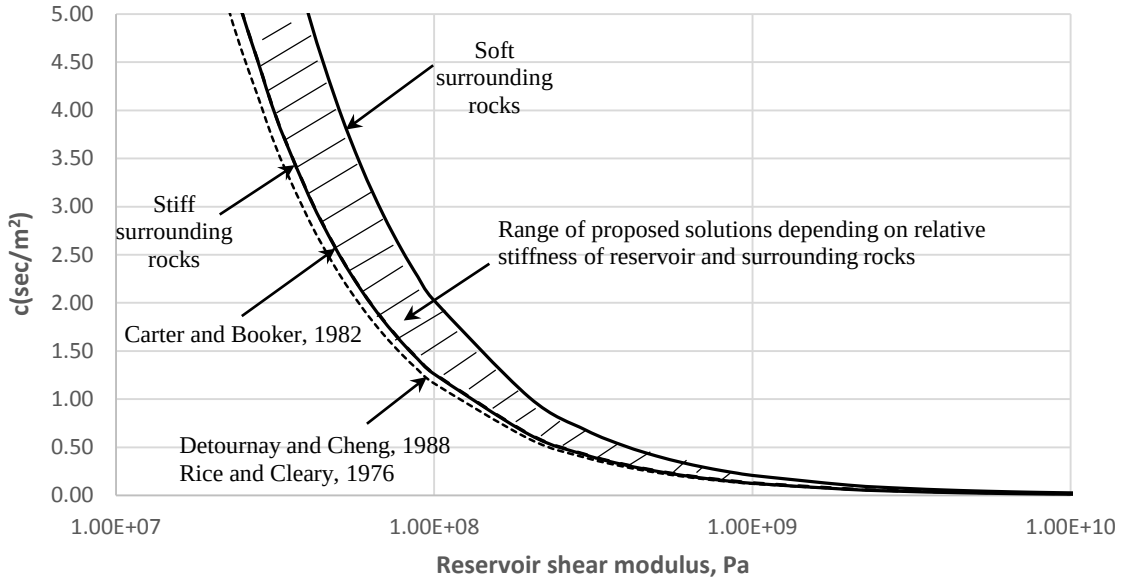

Figure 5-2. "c" for an incompressible fluid: M=5x10^9 Pa; $v = 0.2$; $v_u = 0.4$; $k = 2.98\text{x}10^{-9} m^2/(Pa.sec)$.

5.3 Numerical Simulation

A new tightly-coupled axisymmetric numerical model is developed in this study, using the explicit mode of FLAC3D, to evaluate wellbore injection in a confined geological reservoir. FLAC3D is a finite difference based program for engineering mechanics computation. Flow and mechanical calculations are set to be performed in parallel to capture effects of fluid-solid interactions. In order to numerically replicate interactions of the reservoir formation with the confining seal rocks, "interfaces" are adopted. "Interface" in the Flac3D program represents a plane on which sliding or separation can occur, and is thus defined via normal and shear stiffness values. "Interface" is characterised by Coulomb sliding and/or tensile separation, thus taking the properties of friction, cohesion, dilation, normal and shear stiffness, and tensile strength. Injection is introduced as point sources distributed throughout the thickness of the porous layer to replicated fully penetrating wellbore injection.

Material properties of the unconsolidated sandstone basins are chosen based on typical data reported in the literature (Monicard, 1980; Bratli et al., 1981; Warren et al., 1997; Pape et al., 1998; Hu et al., 2009). Interface properties can be derived from tests on real joints, or from published data. Joint properties (i.e. friction angle, cohesion, dilation angle, tensile strength, joint normal and shear stiffness) are conventionally obtained using the triaxial and direct shear laboratory tests. Values of stiffness for rock joints can reportedly

range from 10 – 100 *MPa/m* for joints with soft clay in-filling, to over 100 *GPa/m* for tight joints in granite and basalt (Flac3D Manual). For the purpose of numerical evaluation in this study, the choice of the material properties adopted for the interface should be such that the joint between the reservoir formation and the neighboring seal rock layers be soft enough to influence the behavior of the system. The maximum stiffness reasonable to use for numerical modeling should be less than 10 times the equivalent stiffness of adjacent zones. The solution time of the numerical model will increase once this ratio exceeds ten. For ratios much higher than ten, the solution time significantly increases without notable change in the behavior of the system. On the other hand, serious consideration must be given to reduce interface stiffness values to improve the solution efficiency. They may be problems with interpretation if the normal stiffness is chosen to be very low. One parameter to be checked is the normal displacement on the joints. If this value is greater than roughly 10% of an adjacent zone size, the stiffness should be increased. Input parameters chosen to model wellbore injection in a reservoir formation confined with flexible seal rocks are presented in Table 5-1.

Table 5-1. Input parameters of the model.

Geometry		**Geomechanical Parameters**		**Injection Related Data**	
		E	1.77×10^8 *Pa*	K_f	2.0e9 *Pa*
r_w	0.5 *m*	K_b	1.18×10^8 *Pa*	k	2.98×10^{-9} $m^2/(Pa.sec)$
r_{out}	400.0 *m*	n	0.4	α	1.0
h	0.67 *m*	K_n	5.8×10^8 *Pa/m*	Q_o	0.007 m^3/sec

The model's initial state was set by confirming equilibrium of the entire porous media prior to injection initiation, and assuring involvement of seal rock layers, interfaces, and reservoir formation with one another. Reservoir formation, interfaces, and the surrounding seal rock layers must initially be generated with some separation between the adjacent surfaces, to enable creation of interface elements. Subsequently, porous layers and interfaces are attached to one another. Next, appropriate stresses should be assigned to each porous layer as well as the interface plane in order to execute the desired initial stress field throughout the reservoir.

Various simulations using different mesh settings were carried out to ensure independence of the quantitative observations with respect to the mesh dimension. To better evaluate near wellbore impacts of injection, the mesh geometry is chosen to be finer at this location. In order to improve the simulation's accuracy at the borehole, the mesh is set so the radial magnitude of the element adjacent to the wellbore be

$r_w\pi/180$ times the angle of the slice that is being evaluated. The far-field reservoir boundary should be chosen distant enough to avoid inducing near wellbore effects. In fact, the extent of the reservoir formation chosen to characterize the behavior of geological strata is a crucial parameter, specifically for studying aquifers. One approach for estimating an appropriate reservoir extension is based upon the final induced pore pressure domain for a given injection interval. Pore pressure distribution can be defined through Eq. 40. The extent of the reservoir formation (r_{out}) can then be computed as the location wherein the induced pore pressure yields zero. An alternate approach for defining r_{out} is based on the induced deformation field. For a given injection interval, induced radial displacements can be analytically computed via Eq. 42. Far-field reservoir boundary can thus be defined such that:

$$\frac{\mathrm{u}_{r_{max}}}{\mathrm{u}_{r_{out}}} \leq 0.01 \tag{47}$$

where $\mathrm{u}_{r_{out}}$ is the radial deformation at the location of r_{out}. As will be demonstrated later in this chapter (section 5.7), at any given time the induced deformation field is a considerably wider zone compared to the generated pore pressure domain. Thus, r_{out} in this study is chosen as the location wherein $u_r \rightarrow 0$. For the given geometry, and input parameters presented in Table 5-1, the far-field reservoir boundary is derived to be $800r_w$. The wellbore boundary is mechanically fixed in the radial direction to prevent inward movement of the porous formation during injection. Far-field boundary is also fixed in the radial direction. A schematic of the geometry mesh is presented in Figure 5-3.

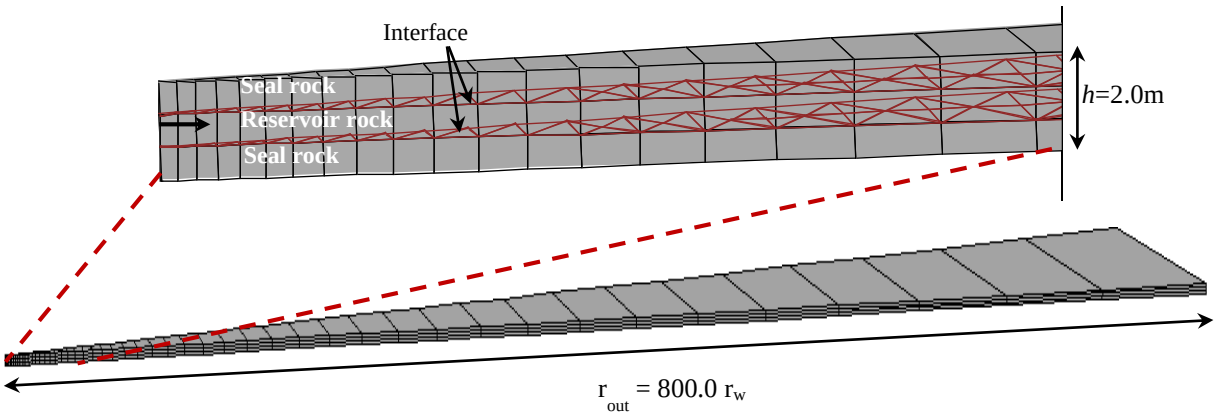

Figure 5-3. Geometry mesh of the numerical model (reservoir depth = 500m; $\gamma_{sat}(reservoir)$= 19 kN/m^3).

In order to numerically evaluate the range of the effect of vertical confinement on the coupled response of an unconsolidated sand layer to injection, two extreme case scenarios are also numerically modeled: unconsolidated reservoir with mechanically fixed upper and lower boundaries, representing stiff seal rock layers; unconsolidated reservoir with an upper stress-boundary (mechanically free), which represents seal rocks with minimal stiffness. These two case scenarios are set using r_{out} obtained from the pore pressure field, a much shorter extension ($r_{out} = 40.0\ r_w$).

Overall three case scenarios with respect to the vertical confinement setting are numerically modeled and compared against the corresponding analytical solutions for verification: the unconsolidated reservoir confined with flexible seal rocks (K_n), the unconsolidated reservoir confined with stiff seal rock layers ($K_n \rightarrow \infty$), and the unconsolidated reservoir confined with seal rocks exhibiting minimal stiffness ($K_n \rightarrow 0$).

5.4 Verification

5.4.1 Flexible Seal Rocks

Induced effective stresses, pore pressures, and radial displacements obtained from the proposed analytical solutions and numerical models are compared for verification. Pore pressures and stresses are normalized with respect to $Q_o/(4\pi hk)$. Displacements are normalized with respect to $Q_o r_w/(4\pi hkE)$. Time history results are presented in terms of a dimensionless time factor T^* computed as $t/(cr_w^2)$. Radial distance from the injection location (r) is normalized with respect to the wellbore radius (r_w). History results are evaluated at three locations ($r/r_w = 1.5;\ r/r_w = 4,\ r/r_w = 6$). The results obtained for the reservoir confined with flexible seal rock layers are presented in this section.

Numerical and analytical pore pressure histories at different locations are illustrated in Figure 5-4.

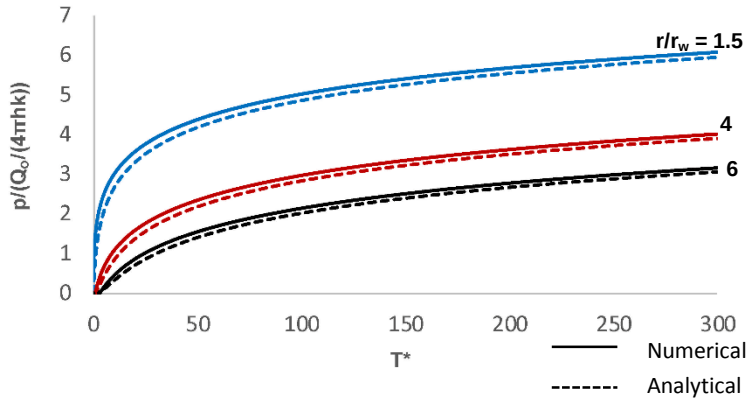

Figure 5-4. Induced pore pressure histories.

Induced effective stress histories are presented in Figure 5-5 through Figure 5-7.

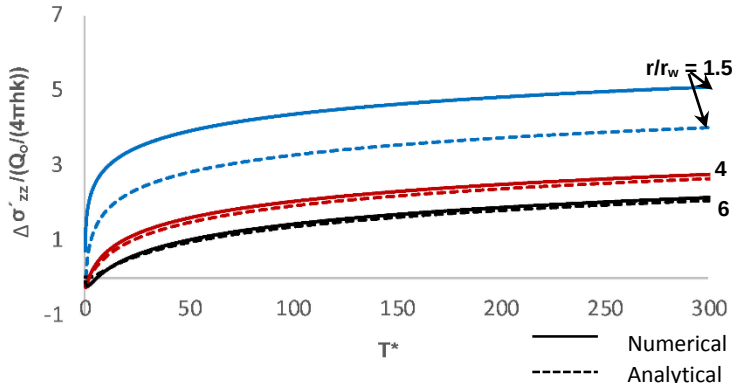

Figure 5-5. Induced effective vertical stress histories.

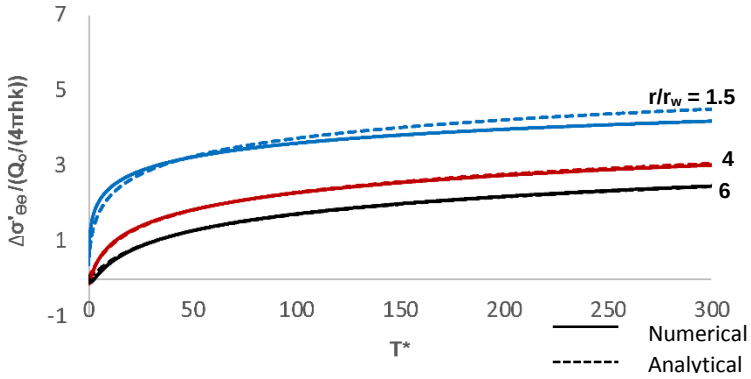

Figure 5-6. Induced effective tangential stress histories.

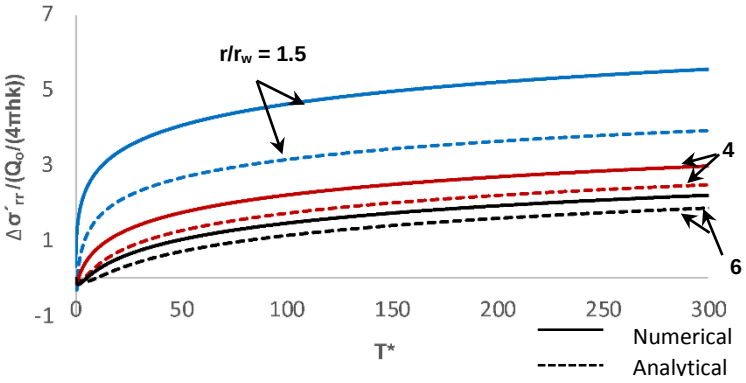

Figure 5-7. Induced effective radial stress histories.

For a more thorough comparison of the analytical solution versus the numerical model, pore pressures, induced effective stress distributions, and radial displacements at different times during an injection cycle are presented in Figure 5-8 through Figure 5-12.

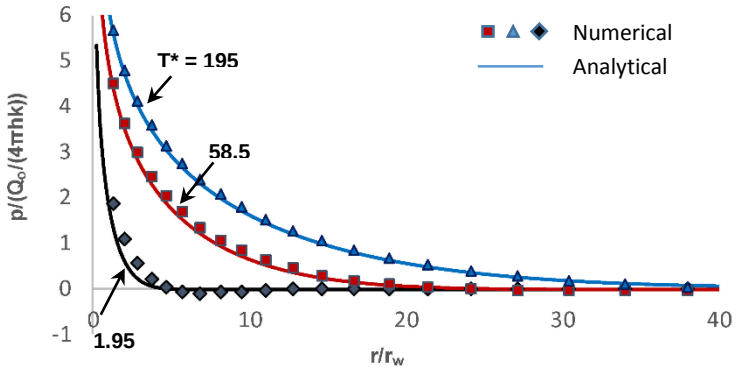

Figure 5-8. Pore pressure distributions at different T^*.

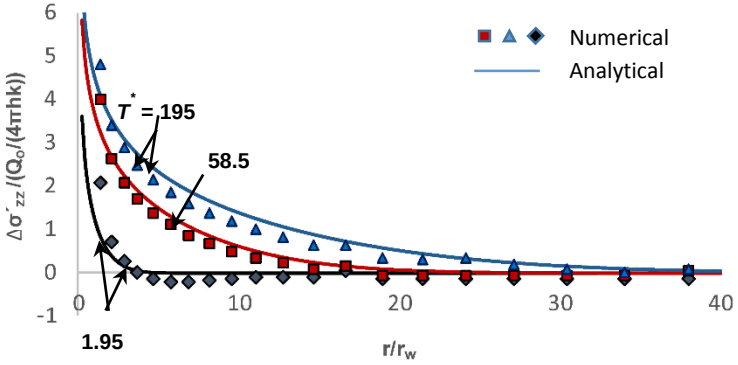

Figure 5-9. $\Delta\sigma'_{zz}$ distributions at different T^*.

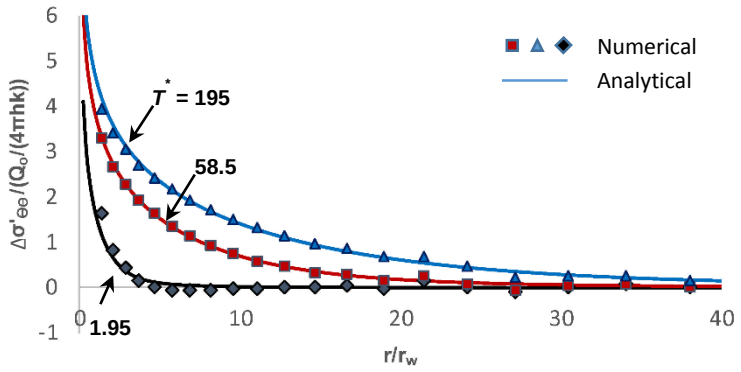

Figure 5-10. $\Delta\sigma'_{\theta\theta}$ distributions at different T^*.

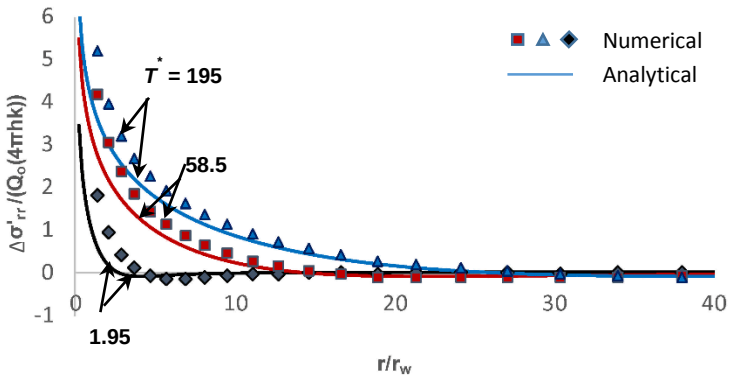

Figure 5-11. $\Delta\sigma'_{rr}$ distributions at different T^*.

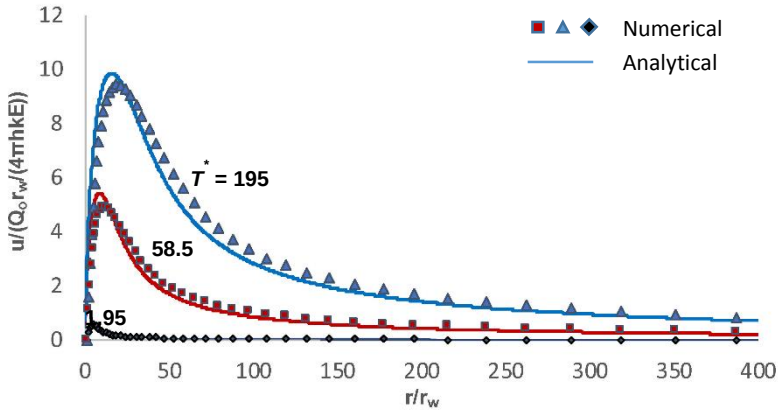

Figure 5-12. Radial displacement distributions at different T^*.

Pore pressure results illustrate an almost perfect match between numerical and analytical values. A reasonable good accordance is detected between analytical and numerical stress results. The substantial discrepancy between analytical and numerical values is detected in the element adjacent to the wellbore ($r/r_w = 1.5$). One reason for this inconsistency is the fact that the analytical solutions are obtained for a point source injection ($r_w \rightarrow 0$), whereas the numerical model simulates wellbore injection ($r_w \neq 0$). Another factor producing divergence between the results is the boundary effect on the element near the borehole in the numerical model.

5.4.2 Stiff Seal Rocks

Numerical results obtained from the case scenario of an unconsolidated sand layer with mechanically fixed upper and lower boundaries are compared against analytical solutions where $K_n \rightarrow \infty$. It must be noted that for the numerical modeling of this case scenario, the outer reservoir boundary has been set to be $40r_w$, which is typically considered to be distant enough to have trivial effects on the near wellbore region, specifically for poroelastic conditions. Pore pressure histories are illustrated in Figure 5-13. Induced effective stress histories are presented in Figure 5-14 to Figure 5-16.

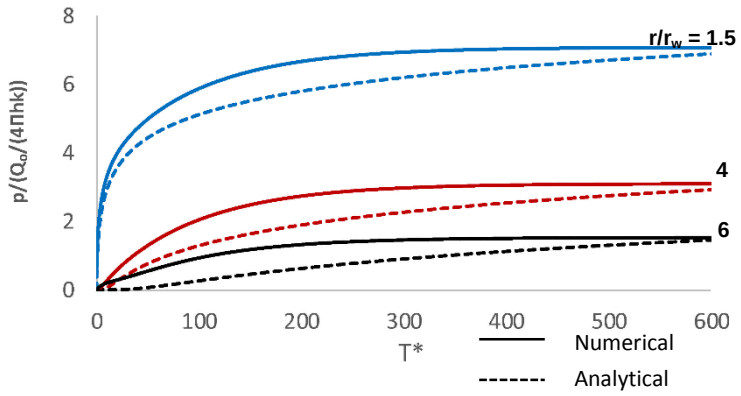

Figure 5-13. Induced pore pressure histories.

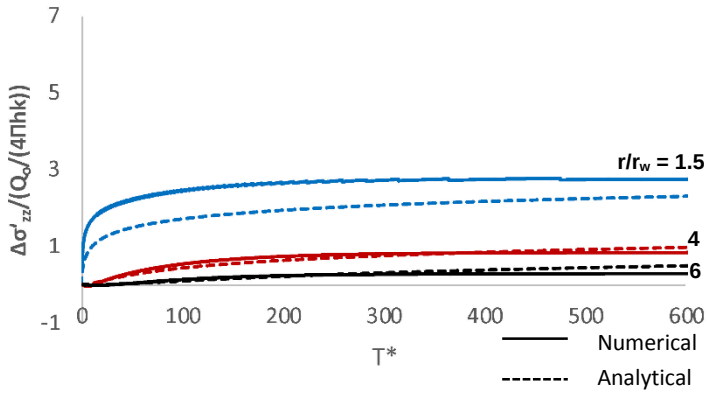

Figure 5-14. Induced effective vertical stress histories.

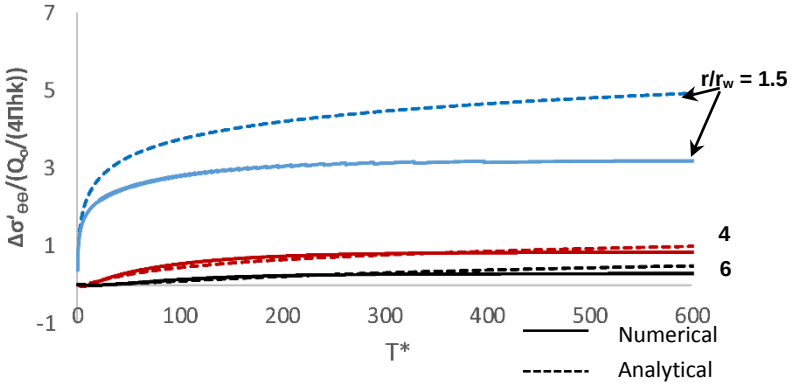

Figure 5-15. Induced effective tangential stress histories.

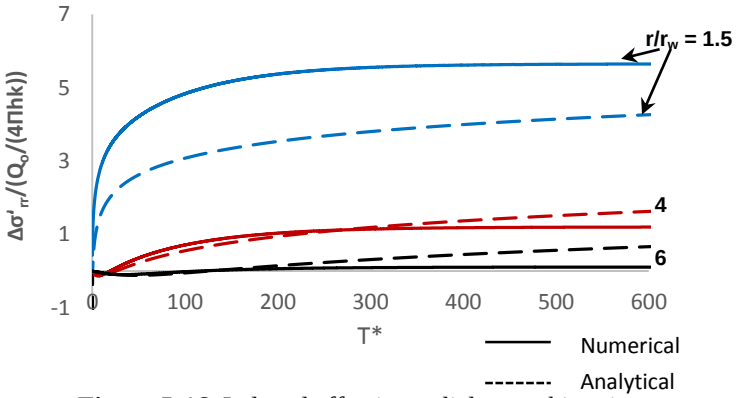

Figure 5-16. Induced effective radial stress histories.

Pore pressure, induced effective stress, and radial displacement distributions at different T^* are presented in Figure 5-17 through Figure 5-21.

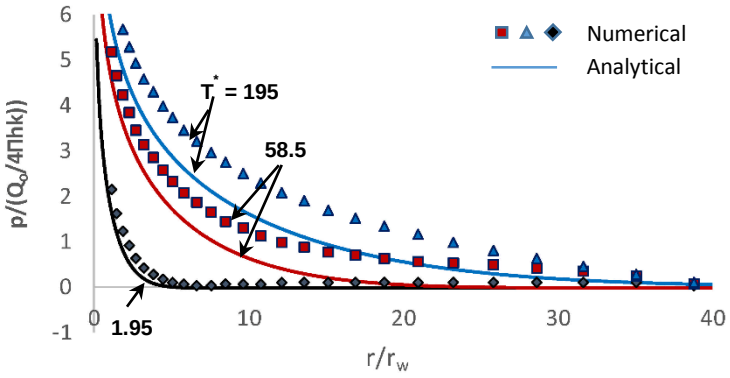

Figure 5-17. Pore pressure distributions at different T^*.

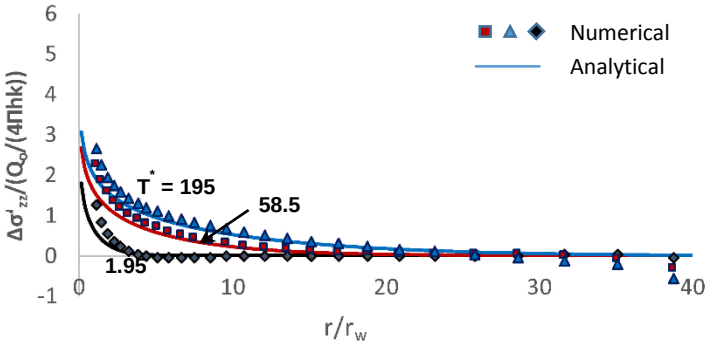

Figure 5-18. $\Delta\sigma'_{zz}$ distributions at different T^*.

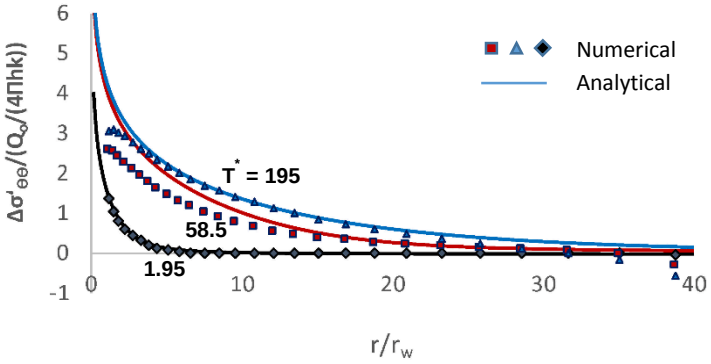

Figure 5-19. $\Delta\sigma'_{\theta\theta}$ distributions at different T^*.

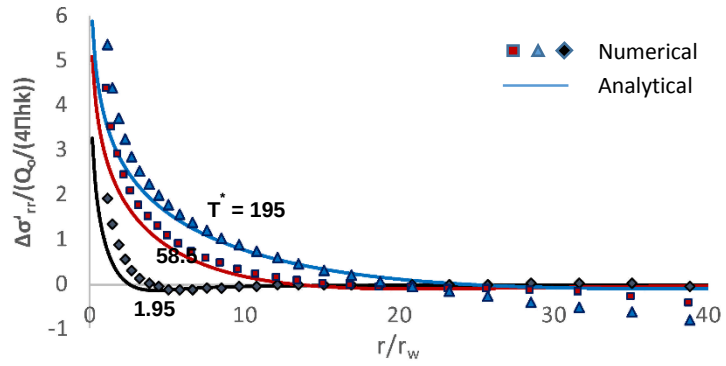

Figure 5-20. $\Delta\sigma'_{rr}$ distributions at different T^*.

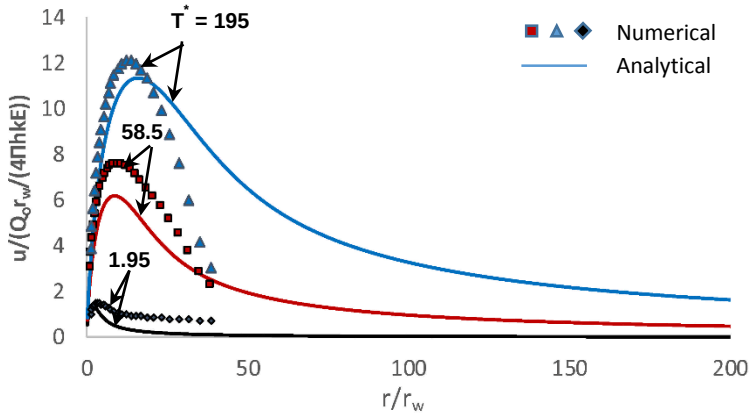

Figure 5-21. Radial displacement distributions at different T^*.

Figure 5-13 and Figure 5-17 clearly illustrate a faster pore pressure build-up obtained via the numerical model compared to the corresponding values attained from the analytical solutions. This discrepancy is in fact a result of the outer boundary effect which was chosen to be $40r_w$, considerably smaller with respect to the entire deformation field computed from the analytical solutions ($800r_w$). As all the boundaries are mechanically fixed in this case scenario, reducing the reservoir extension will result in the injection region behaving in a stiffer manner. This brings about a faster pressure build up in the numerical model. Pore pressure, stress, and displacement results at different times during injection, however, indicate that even though the reservoir extension adopted for numerical modeling was chosen to be *1/20* of the entire impacted region, a somewhat good accordance is still obtainable between analytical and numerical values. The substantial discrepancy between analytical and numerical results is once again detected in the element

adjacent to the wellbore ($r/r_w = 1.5$), due to boundary effects as well as the fact that point source solutions are being compared against wellbore injection.

5.4.3 Seal Rocks with Minimal stiffness

In this section, numerical results obtained for an unconsolidated sand layer confined with impermeable seal rocks of minimal vertical stiffness (upper boundary set as a stress-boundary to replicate the overburden load), are compared against analytical solutions where $K_n \rightarrow 0$. The reservoir extension for the numerical model was set to be $40r_w$, similar to subsection 5.3.2.

Pore pressure histories are illustrated in Figure 5-22. Induced effective stress histories are presented in Figure 5-23 through Figure 5-25.

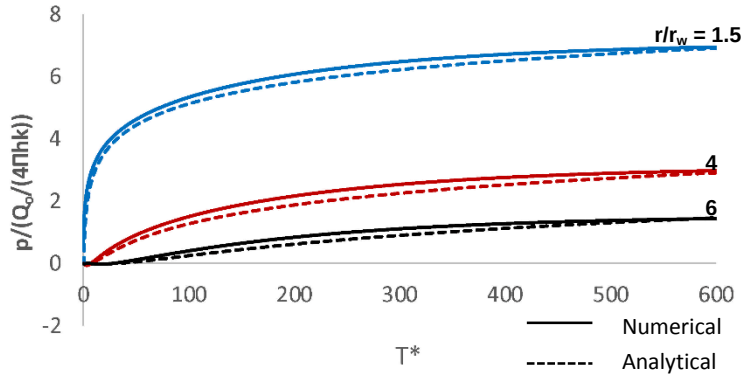

Figure 5-22. Pore pressure distributions at different T^*.

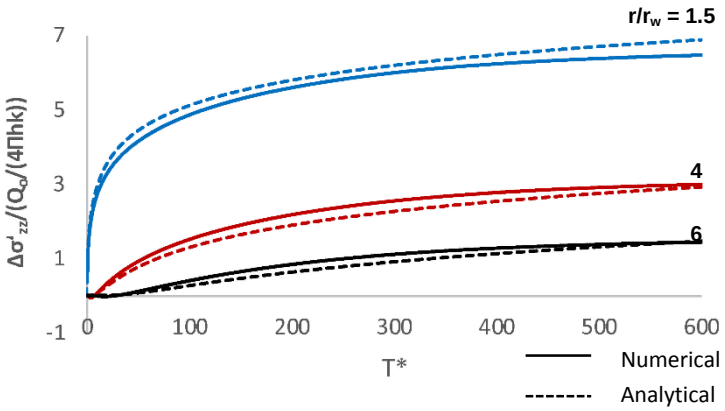

Figure 5-23. Induced effective vertical stress histories.

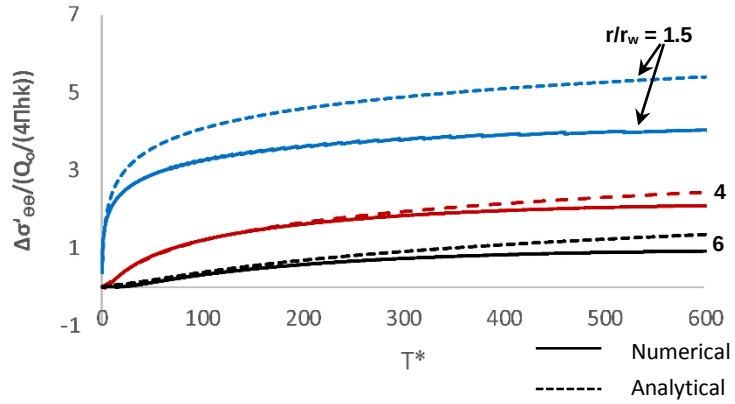

Figure 5-24. Induced effective tangential stress histories.

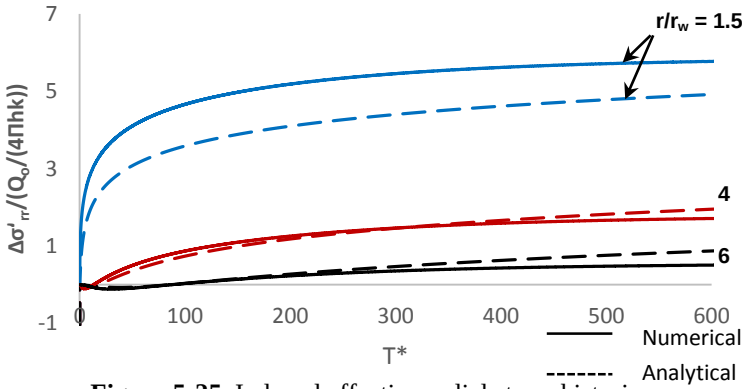

Figure 5-25. Induced effective radial stress histories.

Pore pressures, induced effective stress distributions, and radial displacement distributions at different T^* are presented in Figure 5-26 through Figure 5-30.

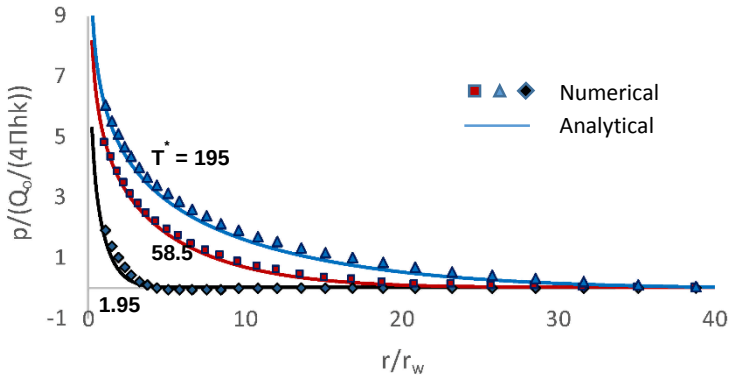

Figure 5-26. Pore pressure distributions at different T^*.

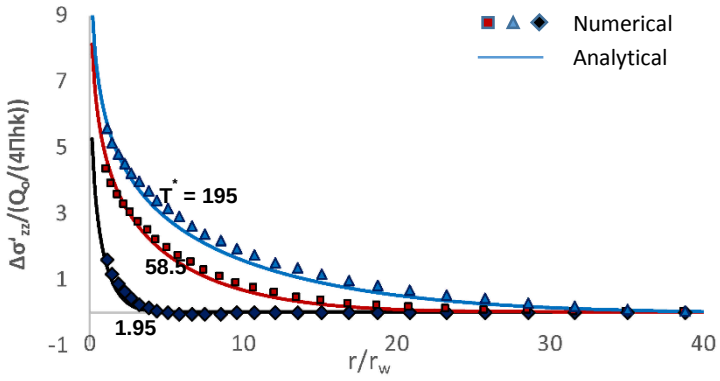

Figure 5-27. Vertical stress distributions at different T^*.

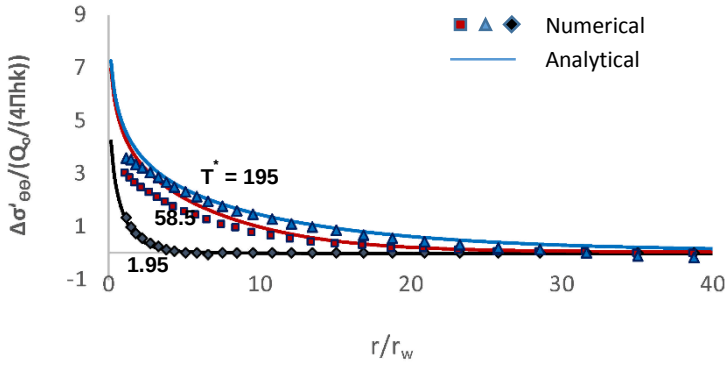

Figure 5-28. Tangential stress distributions at different T^*.

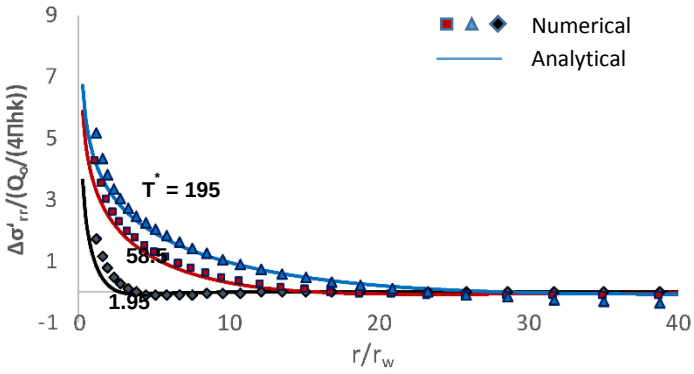

Figure 5-29. Radial stress distributions at different T^*.

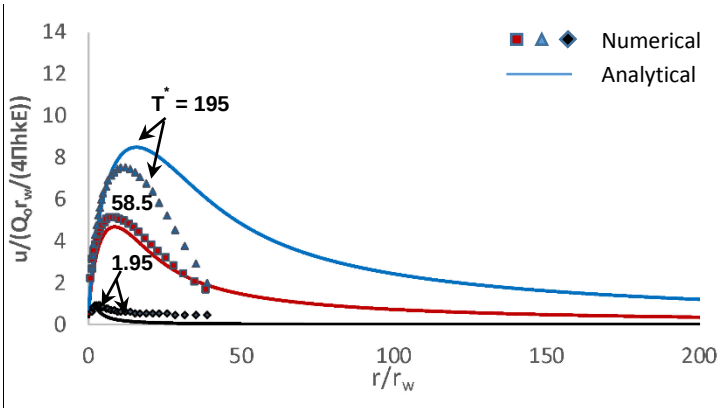

Figure 5-30. Radial displacement distributions at different T^*.

Pore pressure, stress, and displacement results during injection indicate an accordance between numerical and analytical values in spite of the fact that the reservoir extension adopted for the numerical modeling was poorly-chosen to be 1/20 of the impacted region. The rationale behind the better accuracy of the numerical model obtained in this case scenario versus an identical case with stiff seal rocks is the higher degree of freedom in the former. Once the reservoir extension is reduced within a plane strain model, the resulting impacts will be more significant compared to an identical case with flexible seal rocks, or seal rocks containing minimal stiffness. Substantial discrepancy between analytical and numerical values is once again detected in the element adjacent to the wellbore ($r/r_w = 1.5$), due to boundary effects as well as the fact that point source solutions are being compared against wellbore injection.

5.5 Impact of Seal Rock Stiffness upon the Geomechanics of Injection

The impact of vertical confinement controlled by the Winkler stiffness parameter (K) is evaluated in this section using the derived analytical solutions. To attain a feasible understanding of K, the Winkler stiffness parameter is normalized with respect to reservoir formation's Bulk modulus (K_b).

Firstly, the impact of K on the coefficient of consolidation is evaluated. For a porous medium and injectant with υ, E, n, K_f presented in Table 5-1, c variation of c for a range of K from zero to infinity is plotted for both incompressible and a compressible fluid (Figure 5-31). Lowest "c" is obtained under greater vertical confinement, i.e. smaller thickness or higher stiffness. This is consistent with graphs presented in Figure 5-1and Figure 5-2. A closer evaluation reveals that K equal to K_b is in fact an inflection point of the graph. This is an interesting observation as it suggests a physical significance of K/K_b.

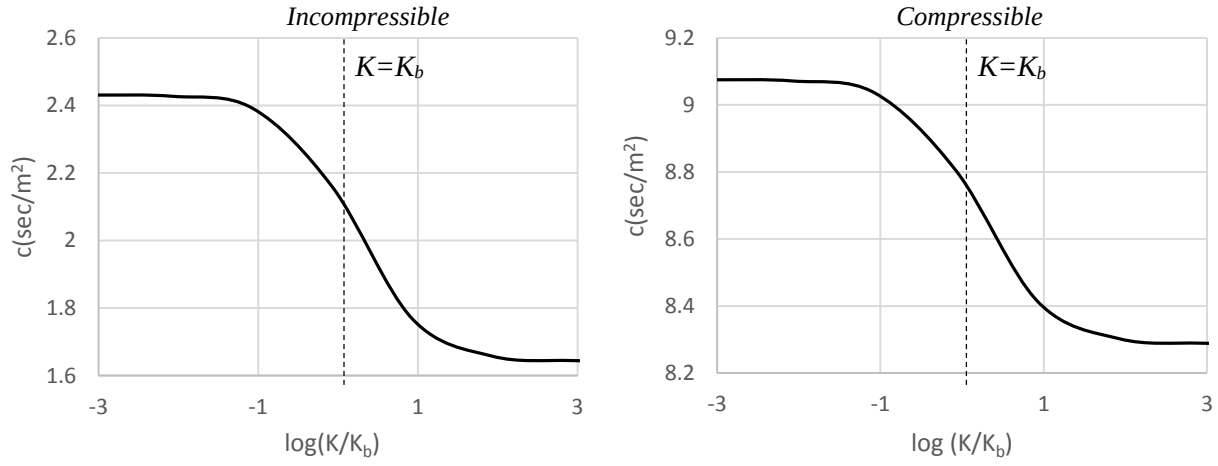

Figure 5-31. Variation of *c* with respect to vertical stiffness: a) Incompressible; b) Compressible.

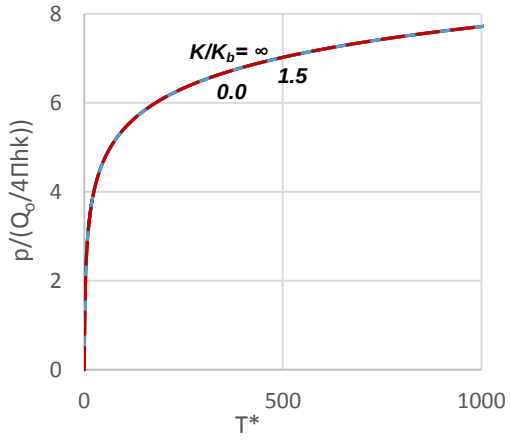

Figure 5-32. Pore pressure history at the wellbore in terms of T^* for various K/K_b.

To study the impact of *K* on pore pressures, pressure histories obtained at $r/r_w \approx 1$ for three case scenarios with different *K* values are presented in Figure 5-32. Once plotted in terms of the stiffness dependent normalized time factor, pressure history results obtained from different *K* values fall into one single curve as the impact of vertical confinement is eliminated in the normalization process (Figure 5-32). Therefore, pore pressure histories in Figure 5-33 are given in terms of real time. Results illustrate highest induced pore pressures in a reservoir with fixed boundaries and lowest generated pressures in a case with no confinement. The sensitivity of the induced pore pressures to *K* is not substantial in the elastic state, as *c* fluctuates in a

limited range for $0 < K < \infty$. It should be noted that at steady state, the right hand side of Eq. 38 approaches zero and thus pore pressures ultimately become independent of "c", or in the vertical confinement condition. The time required for pressures to reach steady state however is dependent upon the vertical confinement. The higher the vertical confinement, the faster the pore pressure increase rate will be (c is lower, see Figure 5-2). Therefore, a shorter period is required for pressures to reach a steady state in case of stiffer sea rock layers.

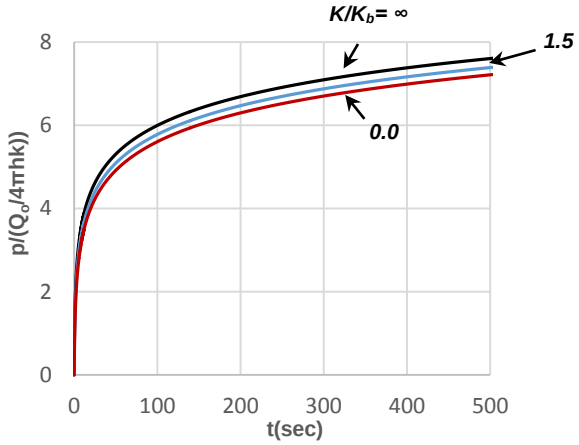

Figure 5-33. Pore pressure history at $r/r_w \approx 1$ for different K/K_b.

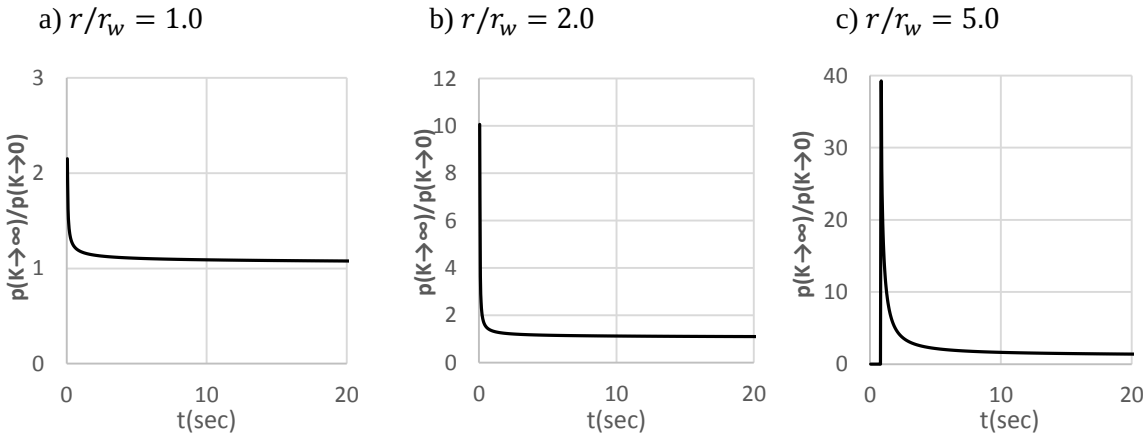

Figure 5-34. $p(K \to \infty)/p(K \to 0)$ histories at different locations.

To further evaluate the qualitative impact of vertical confinement on the induced pore pressures in time during an injection cycle, the ratio of pore pressure in the case of stiff seal rocks (plane strain) to that of a

case with minimal vertical confinement ($p(K \to \infty)/p(K \to 0)$ is computed in time at different locations and plotted in Figure 5-34. The graphs clearly illustrate higher induced pore pressures under stiffer seal rocks. The ratio of $p(K \to \infty)/p(K \to 0)$ is the highest at the moment when pore pressures start to initiate at a given location. This ratio tends to decrease over time and eventually approaches one.

The impact of vertical confinement on the induced effective stress histories at a location close to the injection wellbore ($r/r_w \approx 1$) is presented in Figure 5-35. To better evaluate the extent of the domain throughout which stresses are most sensitive to vertical confinement, stress distributions for different K/K_b at a given time during the injection cycle are offered in Figure 5-36. Results clearly suggest that the horizontal stress components are only slightly impacted at the wellbore, and that vertical confinement has trivial effects in these stresses throughout the remainder of the reservoir formation. The vertical stress component is however found to be substantially sensitive to seal rock stiffness variations. The stress distribution plots demonstrate a notable region surrounding the wellbore ($10r_w$ for this low injection modeling) wherein the vertical stress component is notably affected by the vertical confinement setting.

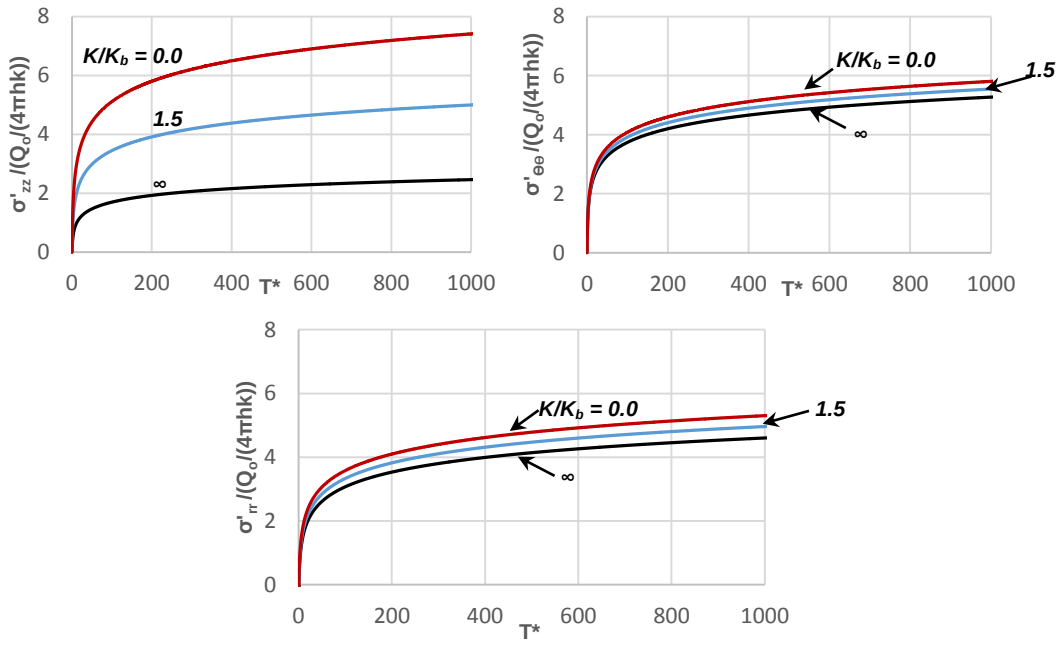

Figure 5-35. Induced effective stress histories at $r/r_w \approx 1$ for different K/K_b.

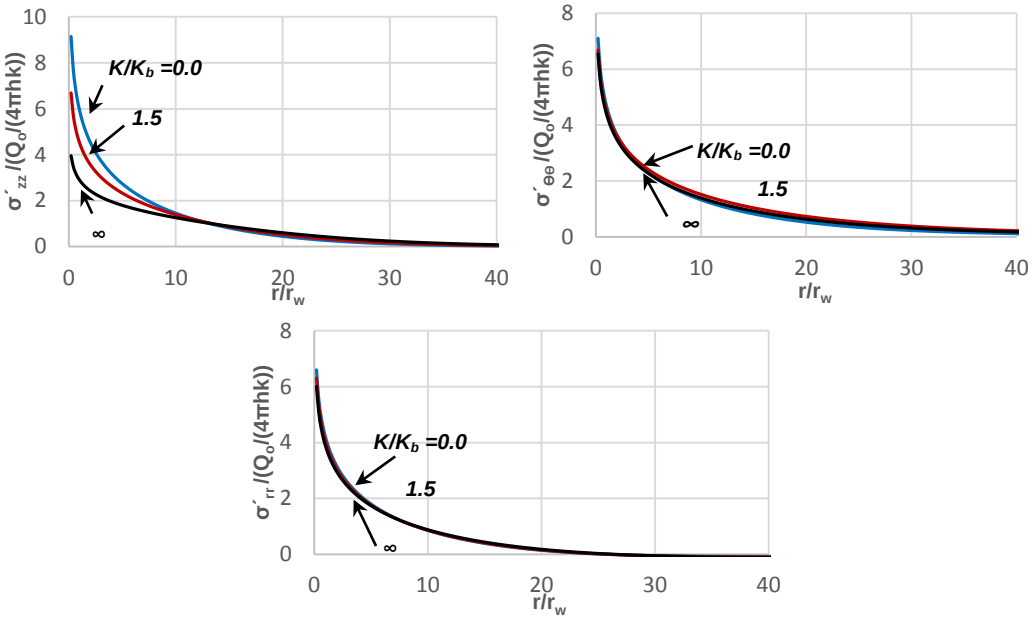

Figure 5-36. Induced effective stress distributions at t = 100 sec for different K/K_b.

The impact of vertical confinement on the induced deformation field is evaluated next. The displacement equations derived in section 5.1.1 (Eqs. 34 and 42) suggest two displacement related parameters that are influenced as a result of vertical confinement: Y (the displacement multiplier) and c (inverse of the coefficient of consolidation). The range of the impact of K_n on induced displacements can be evaluated in terms of variations in YE (a dimensionless quantity) with respect to K/K_b. This is illustrated in Figure 5-37. This plot is quite similar to Figure 5-31, again suggesting the physical significance of K/K_b. It has therefore been reaffirmed that the ratio of the overburden Winkles stiffness parameter to the reservoir's bulk modulus is in fact a limit state parameter. Induced radial displacement distributions obtained for different K/K_b ratios at a given T^* during injection are presented in Figure 5-38. Results illustrate larger deformations in the radial direction induced under stiffer seal rocks.

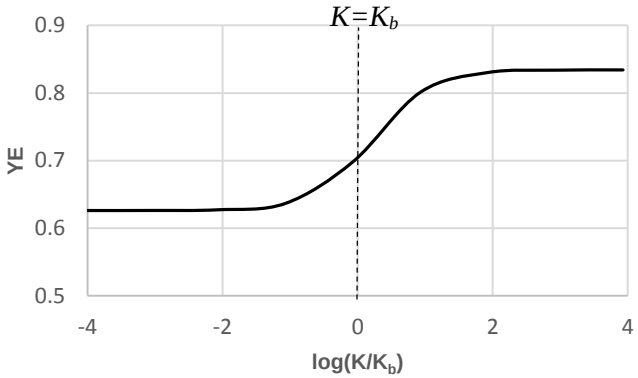

Figure 5-37. Deviation of Y with respect to K/K_b.

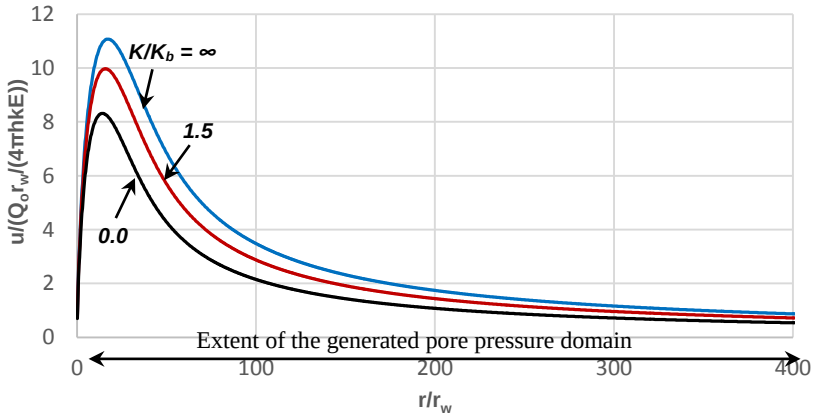

Figure 5-38. Radial displacement distribution for different K/K_b values (T^* = 195).

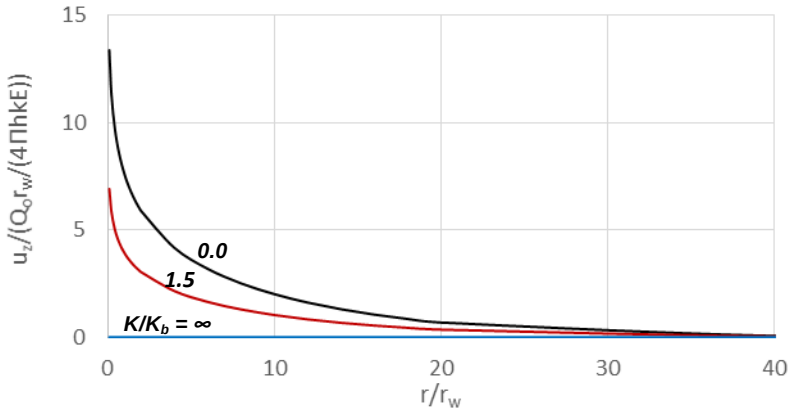

Figure 5-39. Vertical displacement distribution for different K/K_b values (T^* = 195).

Figure 5-39 illustrates sensitivity of induced vertical displacements to the stiffness of the overburden layer (vertical confinement) during the elastic state of radial fluid injection. Vertical displacements are computed using Eq. 26. Results clearly demonstrate that the highest vertical deformations occur under minimal vertical confinement. Induced vertical displacements are trivial in case of stiff seal rock layers, confirming plane strain conditions. A comparison between Figure 5-38 and Figure 5-39 reveals that the area undergoing vertical deformation is notably less in comparison with the area experiencing radial deformation field. However, the sensitivity of the magnitude of deformations in the vertical plane to seal rock stiffness is as significant, if not more, as that of radial displacements. As will be demonstrated in Figure 5-41, the region experiencing nontrivial vertical deformations is in fact the domain within which pore pressures are generated due to injection.

5.6 Magnitude and Location of Maximum Induced u_r

The magnitude and location of the maximum induced radial displacement (u_{rmax}) at any given time during injection can be applied as a valuable control index for prediction of the major impact domain. Moreover, this parameter can be useful for optimization of monitoring strategies, as the subsurface deformations translate into ground surface dislocations. The location of u_{rmax} (r_{Umax}) is obtained from setting $\partial u/\partial r$ to zero in Eq. 42:

$$E_1(X) + \frac{1}{X}[\exp(-X) - 1] = 0 \tag{53}$$

where $X = cr^2/(4t)$. From Eq. 53, X is always *0.32135*, based on which r_{Umax} at time t is derived to be:

$$r_{u_{max}} = 1.134\sqrt{\frac{t}{c}} \tag{54}$$

Substituting Eq. 54 in the displacement equation gives the following relation for u_{rmax} as a function of time:

$$u_{rmax} = \frac{\alpha Y Q_o}{\pi h k}\sqrt{\frac{t}{c}} \tag{55}$$

As presented in Eq. 55, the magnitude of the maximum induced radial deformation is a function of vertical confinement, as the term $Y/\sqrt{c}$ is governed by the overburden stiffness. Figure 5-40 illustrates $u_{rmax}4\pi h\sqrt{k/t^*}$ versus $\log(K/K_b)$ for a range of injection rates. The magnitude of the maximum induced

radial displacement can thus be obtained at any given time, for a given injection rate once *k* and *h* are defined. As already expected, higher injection rates result in greater u_{rmax}. For a given injection rate, a higher vertical confinement (*K)* results in larger induced radial deformations. This influence is magnified under higher injection rates. The graph presented in Figure 5-41 also reaffirms the physical significance of K/K_b.

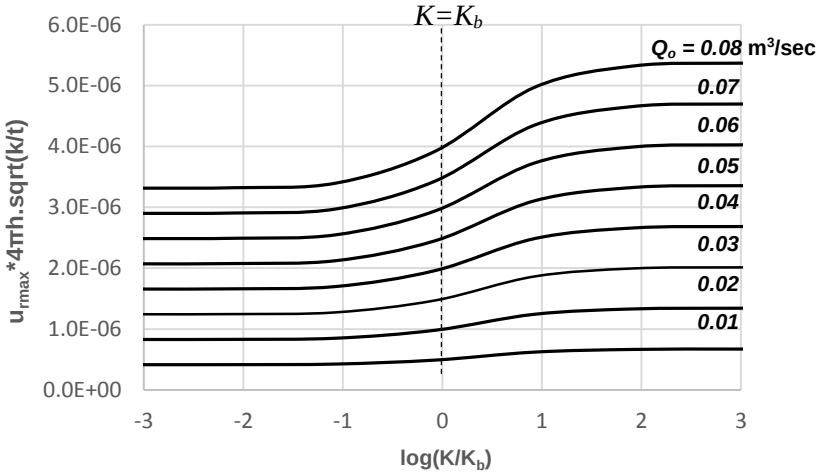

Figure 5-40. Variation of u_{rmax} with respect to vertical confinement for different injection rates: *E = 1.77 x 10^8 Pa; v= 0.25; α=1; n = 0.4.*

5.7 Appropriate Reservoir Extension for Numerical Simulation

The extent of the far-field reservoir boundary chosen to numerically evaluate the behavior of a geological reservoir is an important parameter, specifically where the location of faults or any other wellbore (e.g. production, injection, monitoring) within the injection layer can be considered infinite with respect to the wellbore of interest. A far-field reservoir boundary should be chosen distant enough to avoid inducing near wellbore effects during numerical modeling. Meanwhile, selecting an extensive outer boundary leads to a much wider domain which translates into a larger number of model elements, more degrees of freedom, and thus a computationally more intensive model. It is therefore useful to be able to determine an appropriate far-field boundary for an optimal numerical simulation. As previously mentioned in section 5.3 of this dissertation, extension of the reservoir can be determined analytically either from the induced pore pressure field or the induced deformation field. r_{out} for numerical simulation can be chosen as the location subsequent to which trivial pore pressures or displacements are generated as a result of injection flow. Figure **5-41** illustrates the induced pore pressure distributions under various vertical confinement settings

at a given time (T^*= *195*) subsequent to injection initiation. A comparison between pore pressure distributions presented in Figure 5-41 and displacement distributions at T^* = *195* given in Figure 5-38 clearly indicates that at any given time during the injection cycle, the induced deformation field is a considerably wider zone compared to the generated pore pressure domain. This observation is not only important for optimized modeling, but is also of value for monitoring purposes.

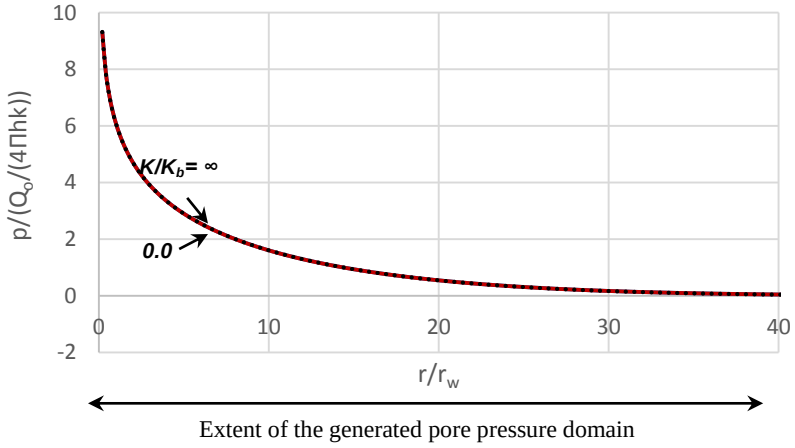

Figure 5-41. Pore pressure distribution for different K/K_b values (T^* = 195).

CHAPTER VI

6. Geomechanics of Injection Prior to Failure

The current chapter is concerned with the geomechanics of fluid injection prior to the state of limiting shear resistance in various stress regimes (isotropic, anisotropic) under different vertical confinement settings. The key objective is to assess failure initiation (both the failure mechanisms and failure planes) in various stress regimes during fluid injection.

In order to examine the response of the porous strata during injection, the in situ stress regime (σ_{ij}) that is a function of both initial (σ_{ij}^{o}) and induced stresses ($\Delta\sigma_{ij}$) must be evaluated in time ($\sigma_{ij} = \sigma_{ij}^{o} + \Delta\sigma_{ij}$). The influence of the initial stress state (prior to injection initiation) on the behavior of the geological medium is of practical importance. A correct representation of in situ stresses is therefore of great significance for appropriate evaluation of geomechanics of injection. Drilling and excavation of the borehole can influence the stress regime surrounding an unprotected borehole (Detournay et al., 1988; Kirsch, 1898). Detournay and Cheng (1988) examined coupled effects induced as a result of borehole excavation in a saturated layer surrounding an unprotected cavity. It was demonstrated that excavation has nontrivial impacts only in a small region surrounding the borehole (on the order of twice the wellbore radius). These induced stress effects were found to dissipate rather quickly in time. In practical geotechnical engineering projects which involve production and injection operations, wellbores with casing are a common practice. Once the casing is set and cemented, the cement column in the well will result in an increase in the pressure against the formation (Risnes et al., 1982). A study of stress distributions subsequent to excavation surrounding both a cemented cased borehole and an open borehole was conducted by Risnes et al. (1982). Results demonstrated generation of plasticity surrounding the open borehole. However, a

drastic reduction of the extent of the plastic zone as a result of the increase in stress levels due to casing was detected. It was concluded that most of the originally plastic zone returns to an elastic state of stress once casing is installed.

Mud drilling is a common technique implemented for excavation of deep cased wellbores. The main advantages of this practice include exerting sufficient hydrostatic pressures against subsurface geological layers to prevent borehole instability as well as avoiding formation fluids from entering the wellbore. The main controllable parameter during drilling operations is the mud unit weight. The optimum mud unit weight is chosen high enough to prevent wellbore collapse, yet low compared to that of the geological formation to prevent inducing notable alterations in the stresses which might ultimately result in formation damage, lost circulation, and an increase rate of penetration (Salehi et al., 2010; Gholami et al., 2014). In cases where the mud pressure is maintained during drilling such that no active yield occurs, no pre-yielded zone will exist in the reservoir formation (Gnirk, 1972; Wang and Dusseault, 1991). In this event, it can be inferred that horizontal stresses surrounding the wellbore will only drop slightly (remaining in the elastic state) during borehole excavation, depending on the mud unit weight. Once the casing is installed, stresses are eventually expected to increase to the initial state due to far field stresses. In the event where minor plasticity is induced in the borehole vicinity during mud drilling process, the plastic zone is expected to eventually return to an elastic state of stress once casing is installed (Risnes et al., 1982). The casing itself, typically cemented to the borehole, is perceived to have trivial effects on the stress state (Morita et al., 1989). Since there is normally a time period between the drilling operation and initiation of the fluid injection process, it is not unrealistic to assume a homogeneous initial in situ stress field in the immediate area surrounding a cased wellbore.

The current chapter focuses on evaluating the coupled geomechanical response of a homogeneous porous layer from an initial elastic state during fluid injection. The objective is to assess failure initiation due to injection in an elastic stress regime. The initial in situ stress surrounding the wellbore is therefore considered to be elastic. It is thus assumed that the mud pressure during drilling process is maintained such to avoid plastic yielding, and that the time period between drilling/casing-completion and initiation of fluid injection is long enough for in situ stresses to return to their initial state surrounding the cased wellbore. Numerous studies presented in the literature on production and injection operations do not incorporate pre-existence of plastic yielding as a result of borehole excavation (Paslay et al., 1963; Bratli et al., 1981; Rudnicki, 1999; Soltanzadeh et al., 2008).

Initial in situ stress components at any given location are related as follows:

$$\sigma'^{o}_{rr} = K_o \sigma'^{o}_{zz} \tag{56.a}$$

$$\sigma'^{o}_{\theta\theta} = K_{r\theta} \sigma'^{o}_{rr} \tag{56.b}$$

where $\sigma'^{o}_{rr}, \sigma'^{o}_{\theta\theta}, \sigma'^{o}_{zz}$ are initial effective stresses in radial, tangential, and vertical planes respectively; K_o is the at-rest earth pressure coefficient; and $K_{r\theta}$ is referred to as the horizontal stress coefficient in this study. In order to evaluate failure initiation, geomechanical response of the formation surrounding an injection wellbore is closely assessed. Various stress fields are examined including: isotropic; normal stress regime with uniform stresses in the horizontal plane; and anisotropic. Fields of active tectonic compression, where the minimum principal stress is in vertical direction, is not a topic of evaluation in this dissertation, as the focus is deep geological formations where the stress field commonly follows a normal stress regime.

The Mohr-Coulomb failure criterion commonly used to describe failure initiation of geomaterials (Risnes et al., 1982; Hsiao, 1988; Rudnicki, 1993; Han et al., 2003; Soltanzadeh et al., 2007) is implemented for states of limiting shear resistance (shear failure) in the reservoir formation. Eqs. 42 – 44 are applicable for computing induced elastic stress-strain-pore pressures, independent of the initial stress regime. The aforementioned point source solutions are found to be a good approximation of wellbore injection ($r_o \rightarrow r_w$) (section 5.4). Results obtained from these equations can be superimposed with initial state values to provide in situ conditions at any given time during injection. It should be emphasized that only normal interactions between the reservoir formation and neighboring seal rock layers are incorporated in this study (via Winkler soil model approximation), and that the shear forces on the interfaces are considered to be trivial. The basic assumptions behind the derived solutions are once again stated as follows: analytical formulations are presented for a semi-finite medium; soil's characteristic parameters are presumed not to vary during injection; soil's behavior is characterized under fully drained circumstances; injectant is assumed to be a Newtonian fluid; effect of gravity is not incorporated for simplicity; shear forces between the reservoir formation and the confining seal rock layers are assumed to be trivial and only vertical interactions are incorporated. Compression stresses (strains) are taken as a negative sign convention in this Chapter.

In order to obtain a generalized insight of the reservoir's response, evaluations are done for a full range of vertical confinement: $K(0 - \infty)$. A zero *K* represents minimal confinement, while $K \rightarrow \infty$ represents seal rocks with notable stiffness. The Winkler stiffness parameter is normalized with respect to the reservoir's bulk modulus (K/K_b) to attain a feasible understanding of vertical confinement in terms of compressibility of the porous layer. In this chapter, stresses are normalized with respect to the initial in situ stress in the vertical plane. Time history results are presented in terms of a normalized time factor T^* computed as

$t/(cr_w^2)$. Evaluations are carried out for the material properties given in Table 6-1, which represent typical characteristic parameters for hydrocarbon reservoirs, and water as the injectant. Finally, to obtain a generalized theorem on failure initiation, a comprehensive analysis is carried out to assess the sensitivity of stress behavior to rock and injectant characteristic parameters.

Table 6-1. Material properties applied for evaluation (Base case).

K	$2.98\text{x}10^{-9}$ $m^2/(Pa.sec)$	n	0.4
α	1.0	E	$1.77\text{x}10^{8}$ Pa
K_f	$2.0\text{x}10^{9}$ Pa	K_b	$1.18\text{x}10^{8}$ Pa

6.1 Stress Modification Surrounding an Injection Wellbore

6.1.1 Uniform In Situ Horizontal Stress Field

In a uniform horizontal stress field, $K_{r\theta} = 1$. Stress modifications surrounding an injection borehole in both isotropic ($K_o = 1$) and normal stress regimes($K_o < 1$), otherwise referred to as tectonically relaxed basins, are assessed in this section.

Isotropic Stress Field($K_o = 1$). Stress paths at the wellbore prior to failure initiation are evaluated for different vertical confinement settings. Results from three limiting cases are presented in Figure 6-1: $K/K_b = 1.5\text{x}10^{-3}$, representing minimal confinement; $K/K_b = 1$; and $K/K_b > 10^3$, replicating stiff seal rocks. Independent of the vertical confinement setting, continuous dilation is detected in the porous formation near the wellbore with injection initiation. However, in each case scenario, a distinctive response is observed at this location.

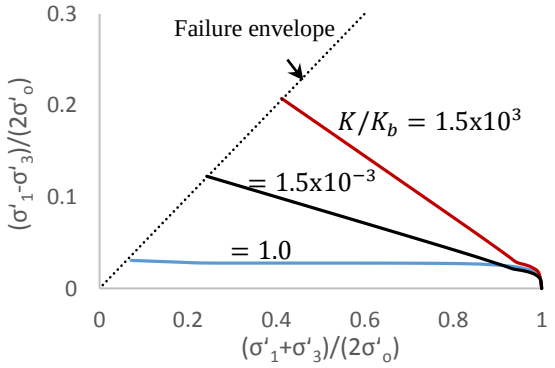

Figure 6-1. Stress paths at $r/r_w \cong 1$ during radial injection; $K_o = 1$.

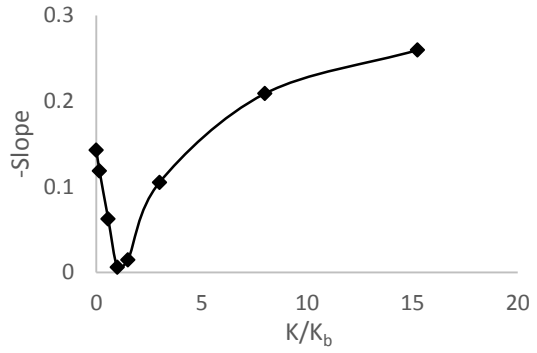

Figure 6-2. Stress path slope variations at $r/r_w \cong 1$ with respect to K/K_b.

Each stress path in **Figure 6-1** can well be represented through a line with a given slope. Therefore, to better explain stress variations as functions of vertical confinement, slope deviations with respect to K/K_b are plotted in Figure 6-2. With an increase in vertical confinement from a state of minimal seal rock stiffness, induced deviatoric stresses tend to decrease. If the overburden Winkler stiffness parameter is comparable to the reservoir's bulk modulus, the generated deviatoric stresses during injection are minimal. Further increasing K once again results in an increase in shear stresses. Highest deviatoric stresses are generated under stiff seal rocks ($K \gg K_b$). These results again clearly suggest that K/K_b is in fact a limit state parameter, having a physical significance.

To further evaluate the reason behind the dissimilar stress behavior observed for different K/K_b values, principal stress histories prior to failure initiation are studied for three case senarios (Figure 6-3): $K < K_b$, $K = K_b$, and $K > K_b$. Results suggest three distinctive stress patterns corresponding to each case: for $K < K_b$, $\sigma_z' < \sigma_\theta' < \sigma_r'$; for $K \approx K_b$, $\sigma_\theta' \leq \sigma_z' < \sigma_r'$; and for $K > K_b$, $\sigma_\theta' < \sigma_r' < \sigma_z'$.

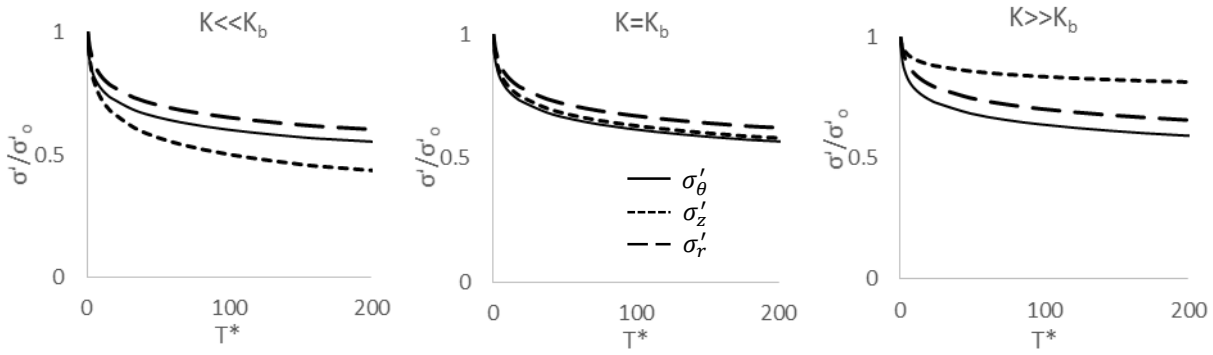

Figure 6-3. Effective stress histories at $r/r_w \cong 1$ prior to failure initiation; $K_o = 1$.

Figure 6-3 illustrates stress patterns corresponding to the stress paths given in Figure 6 – 1. Results clearly indicate that in case of $K \approx K_b$, principal stresses vary in a manner such that the difference between the two remains almost constant (Figure 6-4). As a result, minimal variations in deviatoric stresses are induced during injection. However, the difference between major and minor principal stresses increases in time during injection once $K > K_b$ or $K < K_b$, indicating an increase in shear stresses over time. Nevertheless, the failure initiation plane is found to be a function of K/K_b: where $K < K_b$, failure is induced in $z - r$ plane; for $K \approx K_b$, failure is generated in the $r - \theta$ plane; once $K > K_b$, formation fails in $\theta - z$ plane. These results provide a better insight of the plane where fracture initiates. Principal planes near the wellbore are found to be notably influenced by the vertical confinement setting, or more specifically the ratio of the overburden stiffness to the reservoir bulk modulus. Inaccurate representation of vertical stiffness may lead to misjudgments about seal rock breakthrough and the resulting leakage of injectant into neighboring layers.

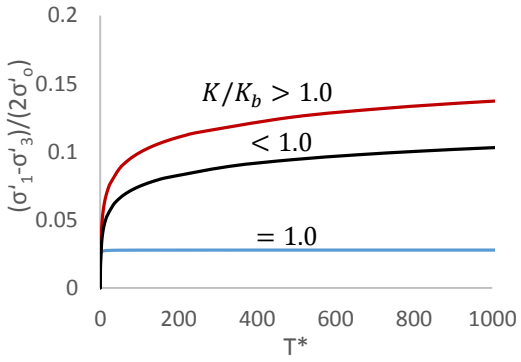

Figure 6-4. Deviatoric stress histories at $r/r_w \cong 1$; $K_o = 1$.

Normal Regime ($\sigma_z > \sigma_r = \sigma_\theta$). Two general case scenarios are examined: $K_o = 0.9$; and $K_o < 0.9$. Figure 6-5 presents stress paths close to the injection source for $K_o = 0.9$. Even though continuous dilation is detected under different vertical confinement settings, graphs once again indicate a notable impact of K/K_b on the stress behavior at this location. Highest deviatoric stresses are once more generated under stiff seal rocks ($K \gg K_b$). For $K \approx K_b$, minimal variations in deviatoric stresses are observed. Figure 6-5 clearly illustrates a complicated stress behavior induced in a case where the reservoir compressibility is lower compared to the vertical confinement ($K < K_b$): deviatoric stresses undergo an initial decrease after which they remain constant for a short period before experiencing an eventual increase.

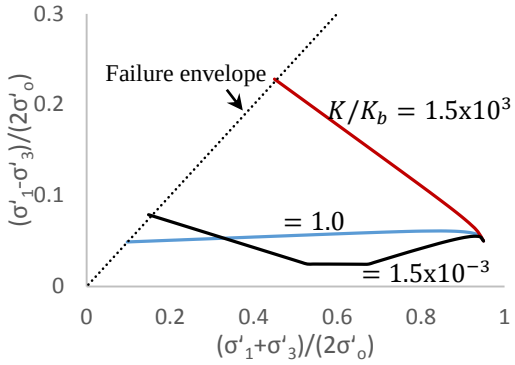

Figure 6-5. Stress path at $r/r_w \cong 1$ during radial injection; $K_o = 0.9$.

To further evaluate the effects of vertical confinement setting on the poroelastic response of the formation at the wellbore, histories of principal stresses at this location are plotted in Figure 6-6. Different stress patterns and dissimilar principal planes induced under various ratios of K/K_b explain the diverse stress paths detected in Figure 6-5 under various vertical confinment settings. Stress histories illustrated in Figure 6-6 clearly show redirection of principal planes where the Winkler stiffness parameter is weaker relative to reservoir's bulk modulus: $\sigma'_\theta < \sigma'_r < \sigma'_z \rightarrow \ \sigma'_\theta < \sigma'_z < \sigma'_r \rightarrow \ \sigma'_z < \sigma'_\theta < \sigma'_r$. Results illustrate the dependence of failure plane on the vertical confinement for $K_o = 0.9$.

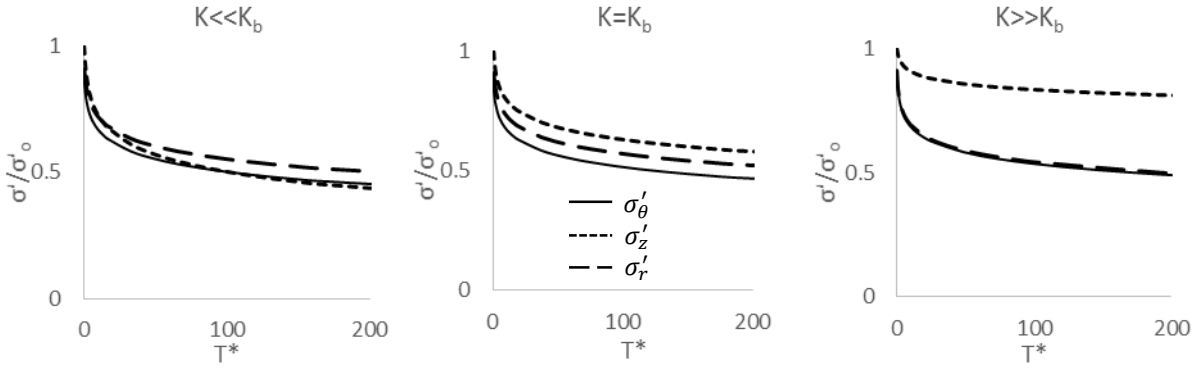

Figure 6-6. Effective stress histories prior to failure initiation at $r/r_w \cong 1$; $K_o = 0.9$.

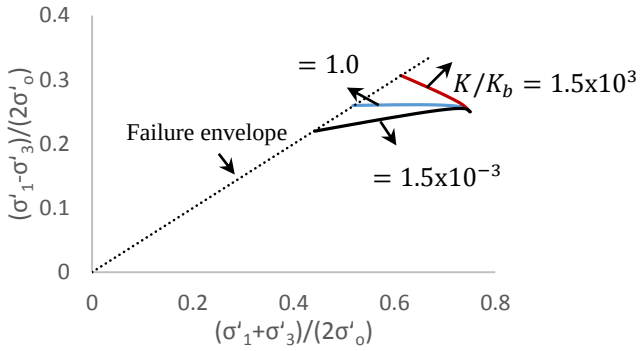

Figure 6-7. Stress path at $r/r_w \cong 1$ during radial injection; $K_o = 0.5$.

In case of $K_o < 0.9$, the stress behavior is found to be similar for all K_o values. Therefore, results obtained for $K_o = 0.5$ is only presented in this section. Stress paths once again demonstrate substantial sensitivity to K/K_b (Figure 6-7). Similar to previous case scenarios, largest deviatoric stresses are generated under stiff seal rocks ($K \gg K_b$). In case of $K \approx K_b$, deviatoric stresses remain constant as variations induced in major and minor principal stresses are fairly identical. For $K < K_b$, a gradual decrease in deviatoric stresses is detected during injection.

As each stress path given in Figure 6-7 can be represented by a straight line, the variation of stress path slope as a function of K/K_b is plotted in Figure 6-8 for better assessment. The graph clearly indicates positive slopes for $K < K_b$, implying a decrease in deviatoric stresses under injection. For $K = K_b$, the slope is zero, suggesting trivial variations in the deviatoric stress. For $K > K_b$ the slope is always negative, indicating an increase in deviatoric stresses as a result of injection.

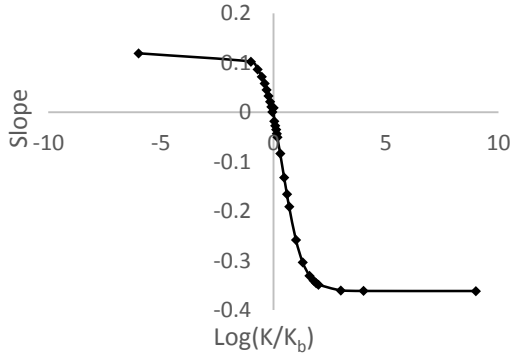

Figure 6-8. Stress path slope at $r/r_w \cong 1$ as a function of K/K_b; $K_o = 0.5$.

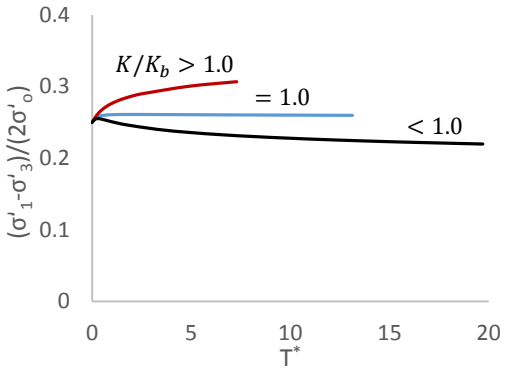

Figure 6-9. Difference between major and minor principal stresses; $K_o = 0.5$.

In this given stress regime, the stress pattern is found to be independent of vertical fixity. It is in fact a dissimilar variation in the induced deviatoric stress under different confinements that creates distinctive stress behaviors (Figure 6-9). The difference between major and minor principal stress: increases for $K > K_b$; decreases for $K < K_b$; and remains constant for $K = K_b$. Results indicate that in a given stress regime, failure initiates sooner under a stiffer vertical confinement (higherK/K_b). It should also be noted that even though the stress behavior for all $K_o < 0.9$ is similar, failure initiation is enhanced under lower K_o values. Stress paths results also demonstrate enhanced failure initiation under stiffer seal rock layers (larger vertical confinement).

6.1.2 Non-Isotropic In Situ Stress Field

In case of a non-isotropic initial stress regime, Eqs. 51 still stand, however $K_{r\theta} \neq 1$. In this section, we evaluate the geomechanical response of various normal stress fields ($K_o \leq 1$) for both $K_{r\theta} < 1$ and $K_{r\theta} > 1$. Results are presented for $K_o = 1, = 0.9, < 0.9$. Figure 6-10 presents stress modifications at the borehole for $K_o = 1$ and $K_{r\theta} < 1$ ($\sigma'_{zo} = \sigma'_{ro} > \sigma'_{\theta o}$). For this given stress regime, $K_{r\theta} > 1$ is not evaluated as this results in horizontal stresses exceeding stresses in the vertical plane, which is not typical in deep geological formations. Similar to the abovementioned case scenarios, minimal deviatoric stresses are generated under $K \cong K_b$. A complicated stress path is detected only in case $K_{r\theta} = 0.9$, where a change in principal planes occurs prior to failure initiation (θr switches to zr) (Figure 6-11). In the case of $K_{r\theta} < 0.9$, the stress behavior is the same for all $K_{r\theta}$. Stress paths reveal an enhanced failure initiation in case of a lower $K_{r\theta}$ value, or in other words an increase in stress anisotropy.

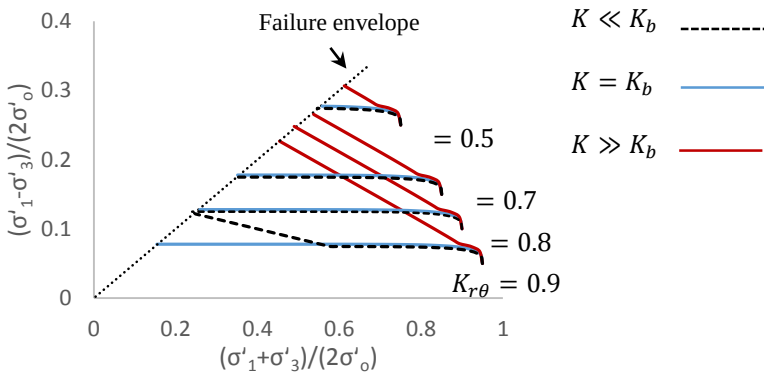

Figure 6-10. Stress paths at $r/r_w \cong 1$; $K_o = 1, K_{r\theta} < 1$.

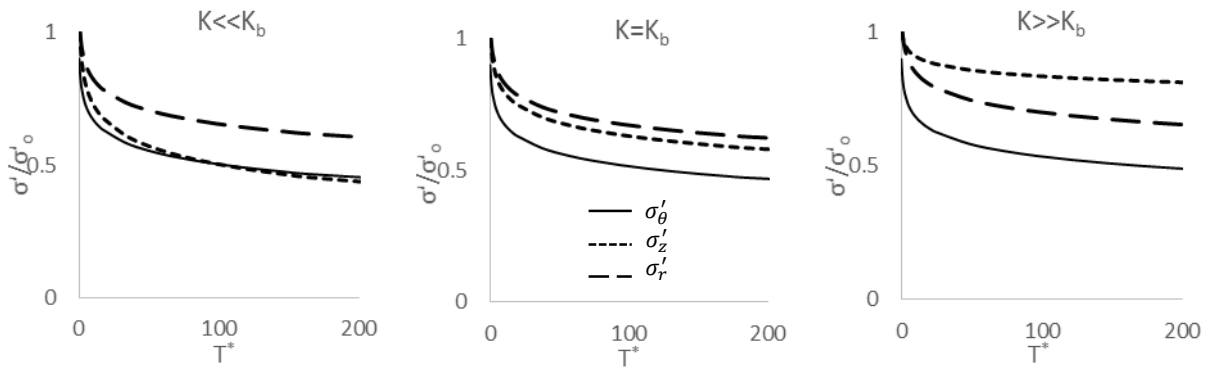

Figure 6-11. Effective stresses prior to failure initiation at $r/r_w \cong 1$; $K_o = 1, K_{r\theta} = 0.9$.

Stress behavior induced in a normal stress regime where $K_o = 0.9$ and $K_{r\theta} < 1$ is presented in Figure 6-12 ($\sigma'_{zo} > \sigma'_{ro} > \sigma'_{\theta o}$). Stress paths as well as stress distributions prior to failure state are similar for all $K_{r\theta} < 0.9$. The only complicated stress path is detected under $K < K_b$, where principal planes change direction during the elastic state (Figure 6-13). Higher anisotropy due to a reduction in $K_{r\theta}$ results in the initial state to be closer to the failure envelope, causing an enhanced failure initiation.

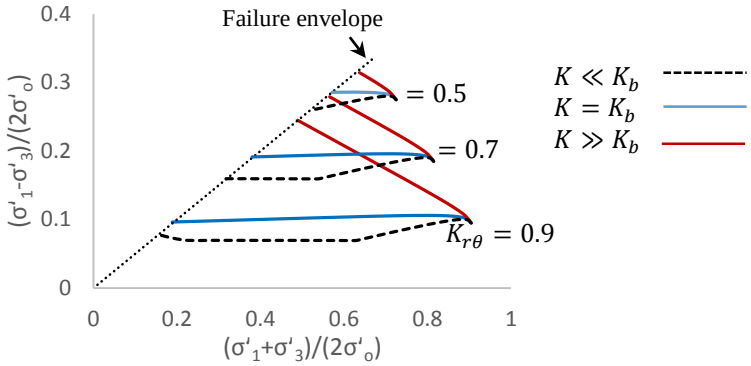

Figure 6-12. Stress paths at $r/r_w \cong 1$; $K_o = 0.9, K_{r\theta} < 1$.

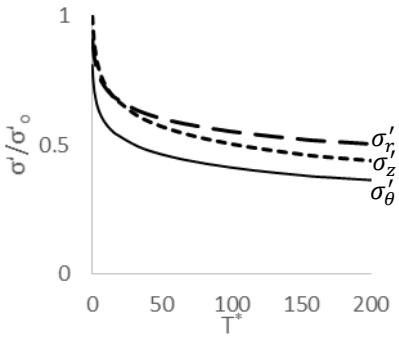

Figure 6-13. Effective stress histories at $r/r_w \cong 1$; $K_o = 0.9$, $K_{r\theta} = 0.9$, $K < K_b$.

Figure 6-14 and Figure 6-15 present the stress behavior for $K_o = 0.9$ in case of $K_{r\theta} > 1$ ($\sigma'_{zo} > \sigma'_{\theta o} > \sigma'_{ro}$). A $K_{r\theta} > 1.1$ results in horizontal stresses exceeding those of the vertical plane, and thus are not evaluated. The stress path corresponding to $K < K_b$ is once again found to be complicated, where multiple changes in principal planes are detected prior to failure ($r-z \rightarrow r-\theta \rightarrow z-\theta$). In the case $K = K_b$, failure is anticipated to initiate near the liquefaction state. The corresponding principal stress histories presented in Figure 6-15 also confirm this speculation.

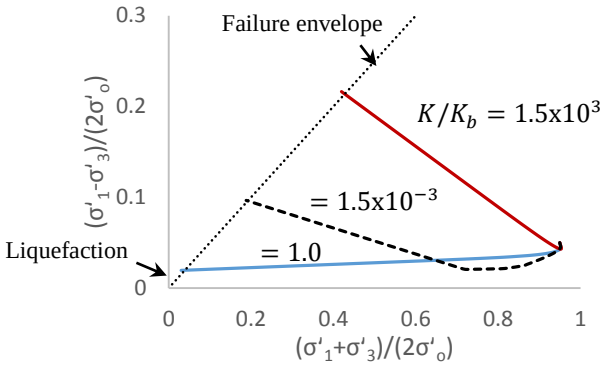

Figure 6-14. Stress paths at $r/r_w \cong 1$; $K_o = 0.9, K_{r\theta} = 1.1$.

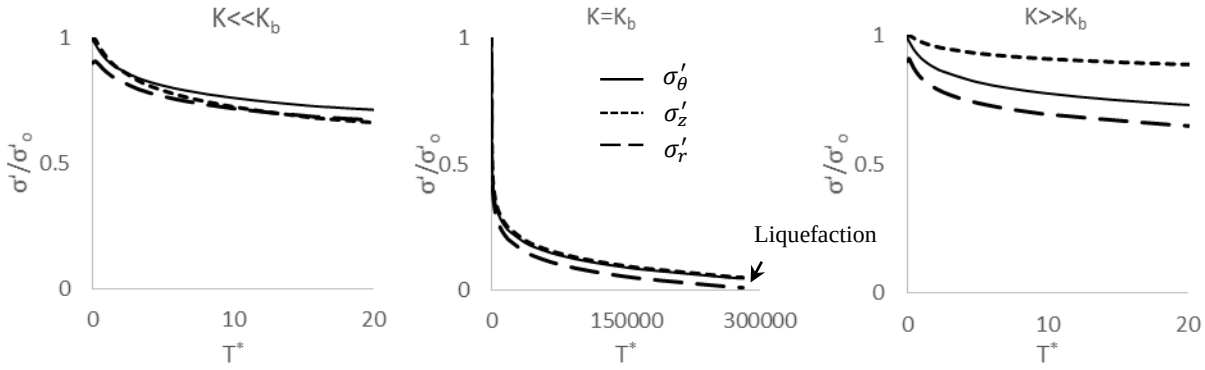

Figure 6-15. Stress distributions prior to failure initiation at $r/r_w \cong 1$; $K_o = 0.9, K_{r\theta} = 1.1$.

Figure 6-16 presents stress variations in a normal stress regime where $K_o = 0.5$ (as a representative illustration for all $K_o < 0.9$), and $K_{r\theta} < 1$ ($\sigma'_{zo} > \sigma'_{ro} > \sigma'_{\theta o}$). Stress path and stress distributions are similar for all $K_{r\theta} < 1$. However, failure initiates sooner in case of higher anisotropy. Stress paths once again demonstrate sensitivity to of the rock response to K/K_b. In case of $K \approx K_b$, deviatoric stresses pretty much remain constant. For $K < K_b$, a gradual decrease in deviatoric stresses is detected during injection. For $K > K_b$, a gradual increase in deviatoric stress takes place during injection. The distinctive stress behavior is associated with dissimilar variations in deviatoric stresses.

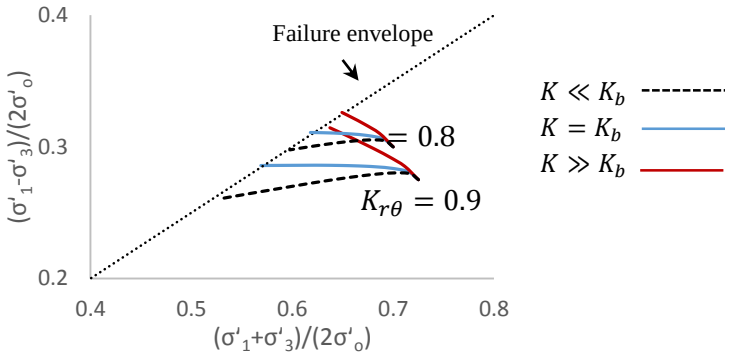

Figure 6-16. Stress paths at $r/r_w \cong 1$; $K_o = 0.5, K_{r\theta} < 1$.

6.1.3 Summary of Principal Planes in Various Stress Regimes

A summary of results is presented in Table 6-2. This study demonstrates for the first time through fundamental geomechanics, the reorientation of the minimum principal plane from horizontal to vertical which takes place once the reservoir's bulk modulus exceeds the vertical confinement stiffness. Under prolonged injection cycles, compressibility of the injection layer decreases in time, resulting in the bulk modulus to exceed the confinement stiffness. If so, depending on the initial stress regime, fracture redirection might occur from horizontal to vertical direction resulting in the injectant moving upwards into the overlaying layer. Problems in the target formation during injection operations and possibility of vertical propagation of fractures during radial injection have been reported in the Celtic SFI Project (Dusseault et al., 1997).

Table 6-2. Summary of stress patterns and failure initiation planes during injection.

K_o	$K_{r\theta}$	Principal Plane ($\sigma_3' - \sigma_1'$)			Minimum Stress		
		$K < K_b$	$K = K_b$	$K > K_b$	$K < K_b$	$K = K_b$	$K > K_b$
1	1	$z-r$	$\theta-r$	$\theta-z$	*vertical*	*horizontal*	
	0.9	$\theta-r$ $z-r$	$\theta-r$	$\theta-z$	*horizontal* *vertical*		
	<0.9	$\theta-r$	$\theta-r$	$\theta-z$	*horizontal*		
0.9	1	$\theta-z$ $\theta-r$ $z-r$	$\theta-z$	$\theta-z$	*horizontal* *vertical*		
	≤ 0.9	$\theta-z$ $\theta-r$	$\theta-z$	$\theta-z$	*horizontal*		
	1.1	$r-z$ $r-\theta$ $z-\theta$	$r-z$ & $r-\theta$	$r-z$	*horizontal* *vertical*		
<0.9	1	$\theta-z$			*horizontal*		
	≤ 0.9	$\theta-z$					
	1< <1/K_o	$\theta-z$ & $r-z$					
	1/K_o	$r-z$					

6.2 Sensitivity Analysis

To obtain a generalized insight into failure initiation in geological reservoirs during fluid injection, a comprehensive sensitivity analysis is carried out with respect to rock-fluid characteristic parameters. The poroelastic response of the porous medium to fluid injection, described via Eqs. 42 – 44, is in fact a function of six variables in addition to the overburden Winkler parameter (as demonstrated in Table 6-1): $n, E, K_b, k, \alpha, and\ K_f$. In this section, the sensitivity of the stress paths presented in section 6.1 are inspected with respect to each of these variables.

Porosity (n). Porosity of deep geological formations is typically in the range of 0.1 – 0.4. It is detected that variation of porosity, even in a wider range, has almost no impact on the stress behaviors which have been presented thus far.

Biot coefficient (α). The Biot coefficient, with a value in the range of zero to unity, reflects the degree of coupling which exists between the porous formation and fluids. The shape of the stress path is found to be insensitive to variations in α, while shorter stress paths are detected under a reduced degree of coupling. Higher injection rates or longer injection periods are required to initiate failure under weaker coupling.

Figure **6-17** illustrates the relation obtained between the degree of coupling (α/b, where b is the inverse of the degree of coupling, $1 \leq b$) and the required increase in injection rate to initiate failure at the wellbore ($Q_{failure}/Q_{org}$; where q_{org} is the injection rate resulting in failure initiation at the wellbore in case of α =1).

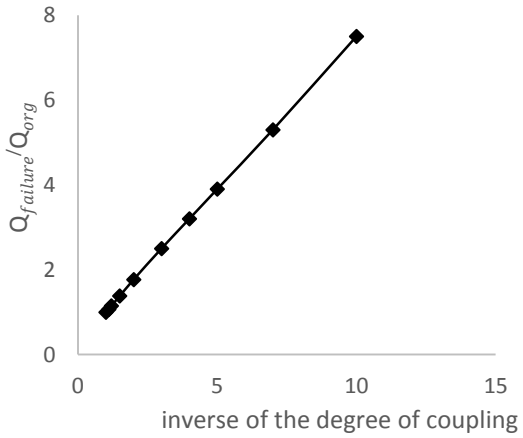

Figure 6-17. Required increase in injection rate to initiate failure.

Bulk modulus of the injectant (K_f). The solutions presented in this study are obtained for single phase flow, and assuming that the injectant possesses similar properties to those of the in situ fluid. With respect to water, K_f is 2.2×10^9 Pa and is expected to increase at higher pressures. Bulk modulus of fluids is typically in the range of 1×10^9 Pa (Benzene) – 3.4×10^9 Pa (Water – glycol). Results of the sensitivity analysis indicate that stress paths are not notably impacted by variations in K_f in this range.

Elastic modulus. Sensitivity of stress paths and stress patterns are evaluated for the following range of elastic moduli: $K_b(0.12 - 1180\ MPa)$, and $G(0.07 - 710\ MPa)$. Results clearly indicate that the quality of stress paths presented thus far is not notably impacted as a result of variations in elastic moduli. However, failure is detected to initiate sooner in formations with higher elastic moduli. As a representative example, the stress behavior at the wellbore in case $K_o = 1$ and $K_{r\theta} = 0.9$ are provided in Figure 6-18 for a formation with high elastic moduli, formation with typical elastic moduli given in Table 6-1, and formation with low elastic moduli. The injection rate and time period chosen for all three cases are identical.

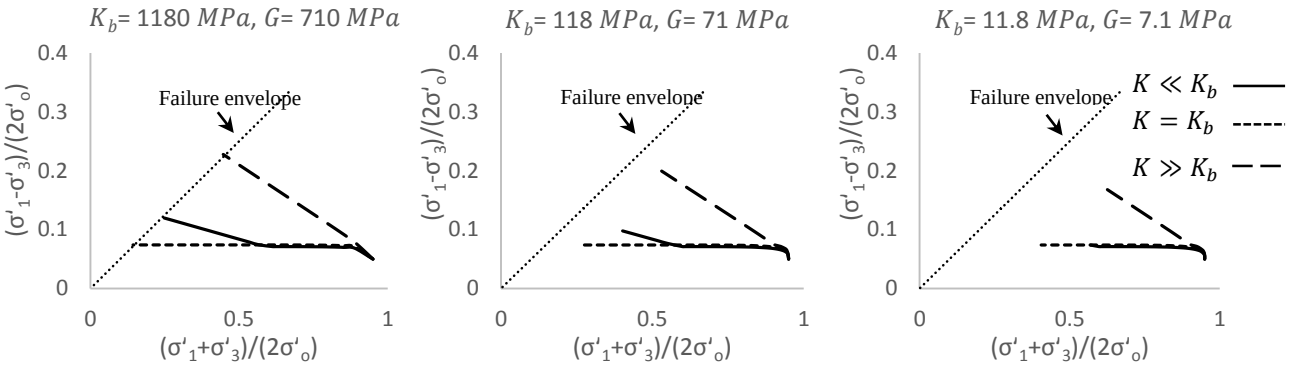

Figure 6-18. Sensitivity of Stress paths to elastic moduli: $K_o = 1$; $K_{r\theta} = 0.9$. .

Permeability. Thus far in this study, an intrinsic permeability (k_{in}) of 3 Darcy is adopted for evaluations. A comprehensive analysis of stress path sensitivity to reservoir permeability was carried out. Results from this sensitivity analysis reveal that under a constant injection rate, failure is initiated sooner in formations with lower permeability. Increasing permeability will postpone failure initiation to a great extent; nevertheless, stress paths and stress patterns presented thus far are nearly unaffected for $k_{in} \leq 10$ Darcy. As a representative example, the stress behavior at the wellbore in cases $K_o = 1$ and $K_{r\theta} = 0.9$ are provided in Figure 6-19 for two identical cases with different permeability. The injection rate and time period chosen for the two cases are identical.

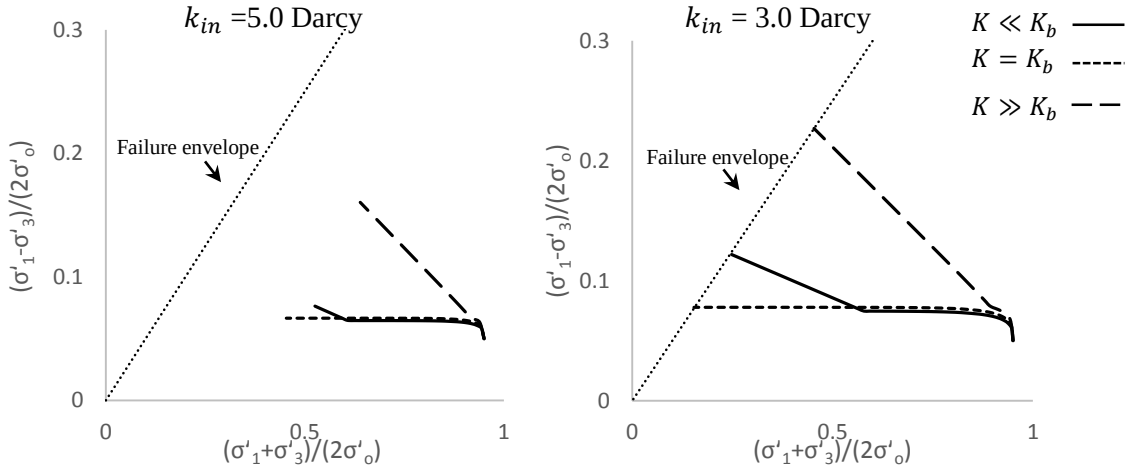

Figure 6-19. Sensitivity of Stress paths to elastic moduli: $K_o = 1$; $K_{r\theta} = 0.9$. .

For $k_{in} \geq 0.5$ Darcy, the overall stress paths presented thus far are not notably impacted as a result of permeability variations. Once $k_{in} \leq 0.03$ Darcy, vertical confinement is found to have trivial impacts on stress patterns (Figure 6-20 through Figure 6-22). It is thus demonstrated that the poroelastic response of a low permeable rock layer to injection is not influenced by seal rock properties, and failure initiation is localized. Therefore, the poroelastic behavior of a rock layer with a permeability lower than 0.03 Darcy can be simulated well via a plane strain approximation.

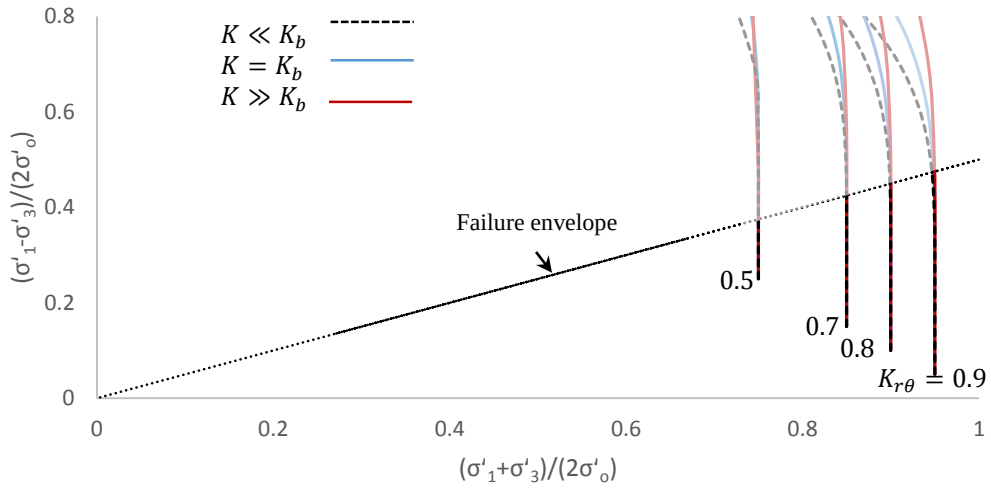

Figure 6-20. Stress paths in a low permeability formation ($k_{in} = 0.03$ Darcy); $K_o = 1$, and $K_{r\theta} < 1$.

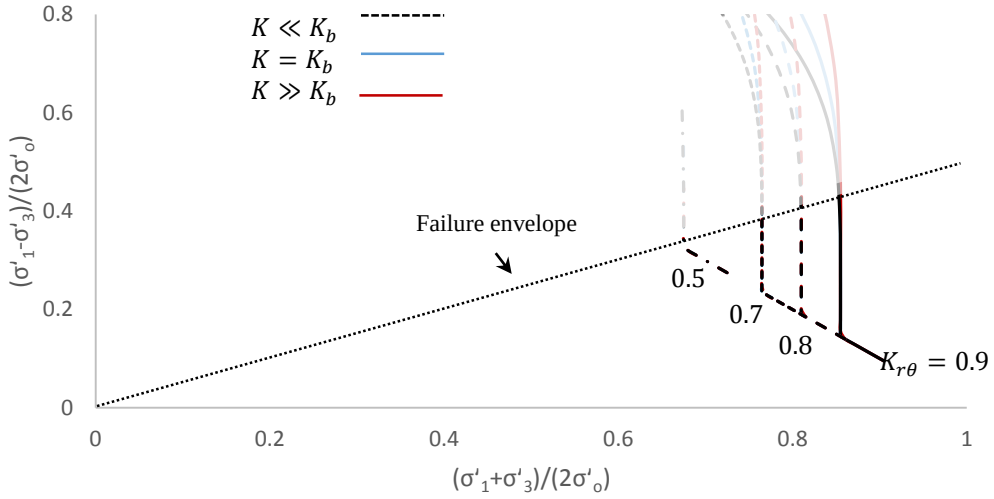

Figure 6-21. Stress paths in a a low permeability formation ($k_{in} = 0.03$ Darcy); $K_o = 0.9$, and $K_{r\theta} < 1$.

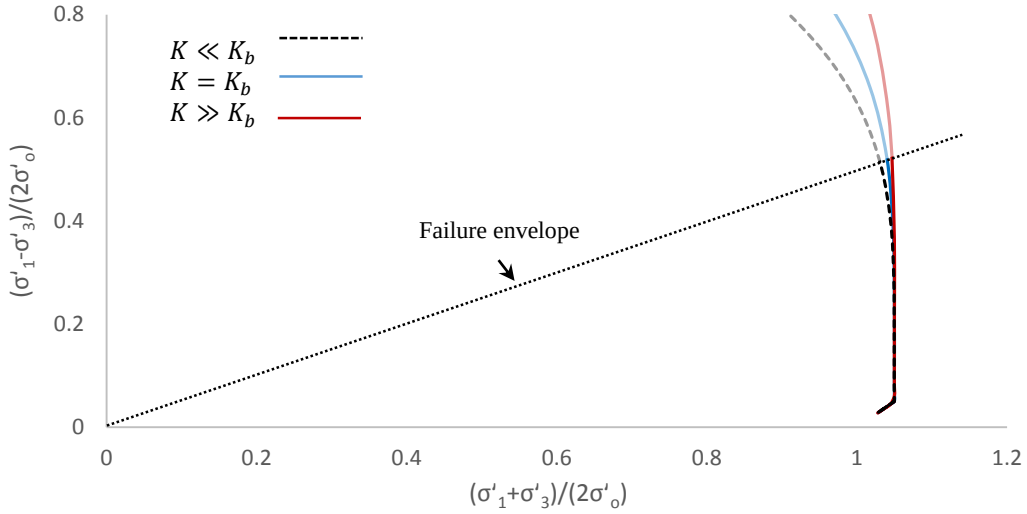

Figure 6-22. Stress paths in a low permeability formation ($k_{in} = 0.03$ Darcy); $K_o = 0.9$, and $K_{r\theta} > 1$.

6.3 Required Pore Pressure to Initiate Failure

The key intention of this section is to predict the pore pressure required to initiate failure within a confined, unconsolidated reservoir as a result of radial fluid injection from a fully penetrating wellbore. At the instant of failure initiation, poroelastic solutions are still valid. Therefore, the analytical solutions derived in Chapter 5 may be applied for evaluating conditions at the moment of failure initiation.

Eq. 21 is the general pore pressure equation, relating the induced pore pressures to the coupled variations in volumetric strains at any given state or time within the porous medium. As demonstrated in Chapter 5, this general equation can be rewritten in the form of Eq. 38 for poroelastic conditions. The general pore pressure equation solution for constant rate point source injection approaches a pseudo steady state when $\frac{\partial p}{\partial t} \cong 0$ (steady state). The variation of pore pressure with distance from the well is logarithmic, i.e., satisfying:

$$\frac{\partial p}{\partial r} = \frac{Q_o}{2\pi k h}\frac{1}{r} \tag{56}$$

where *r(m)* is the radial distance from the injection well. Eq. 56 clearly indicates that pore pressures are independent of the vertical confinement setting, or more specifically the stiffness of the confining seal rocks, at steady state. A common simplifying assumption adopted in previous studies is that flow

approaches steady state for appropriate injection periods, and that the volumetric strain rate becomes trivial (Risnes et al., 1982; Hsiao, 1988; Smith, 1988; Wang et al., 1991; Han et al., 2003). Consequently, Eqs. 21 and 38 revert to Eq. (56).

In order to determine the pore pressure corresponding to failure initiation, stress paths are plotted at a location near the wellbore using analytical effective stress histories. The pore pressure resulting in shear failure initiation ($p(yield)$) is plotted as a function of injection rate, for a range of vertical confinement settings: $K/K_b = \infty, 10.0, 1.0, 0.0$ (Figure 6-23). The graphs indicate that the pore pressure resulting in initiation of failure in the porous medium is mainly governed by the relative stiffness of the reservoir and seal rocks: a higher pore pressure is required to initiate failure under a stiffer seal rock. Results also demonstrate that where the vertical stiffness of the surrounding medium is greater compared to that of the reservoir formation, the pore pressure required to initiate failure is to some extent a function of the injection rate, i.e. with an increase in the injection rate, the pore pressure required to initiate failure slightly decreases. The graph demonstrates independency of $p(yield)$ to the injection rate, in case of minimal vertical confinement setting ($K/K_b = 0.0$).

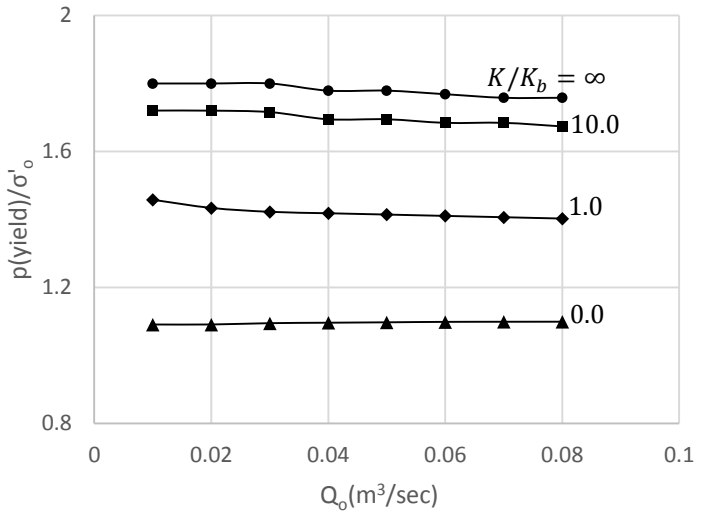

Figure 6-23. Pore pressure at the yield state as a function of injection rate for various relative stiffness values.

CHAPTER VI

7. Poro-Elasto-Plastic Response

The pre-conditioning phase of injection operations in weakly consolidated reservoirs involves fluid injection at high but not fracturing pressures. Although the induced pressures are not high enough to result in initiation and propagation of fractures, notable stress modifications are generated, mainly in the area surrounding the borehole. The resulting intricate behavior of unconsolidated formations (i.e. plasticity, non-linear deformations, strong flow-stress coupling) is commonly associated with high permeability, no cementation, a Young's modulus less than 1 *GPa* , and low mechanical strength.

Most previous work on evaluating injection processes was developed based on at least one of the following assumptions: uncoupled rock reaction with respect to induced pore pressures; elastic behavior of reservoir rock; uncoupled pressure variations with respect to stresses/strains; presence of a pre-existing fracture prior to injection initiation; independency of in situ conditions in the elastic domain from the plastic zone; and a constant stress pattern throughout the plastic domain. Thus far, practically no comprehensive study exists on the coupled geomechanical response of unconsolidated formations during injection prior to fracture initiation and the permanent induced effects. Typically, runtime of a fully coupled flow-mechanical simulation is slow even with powerful computers (the runtime of the numerical model in the current study is 6 months, 661 million steps, on an Intel® i7 processor, 3.33 GHz using FLAC3D version 3.0). Consequently, no comprehensive study has been reported on the coupled response of an unconsolidated reservoir during an entire transient state of an injection cycle. Assessments presented in the literature have been carried out at either very early times subsequent to injection initiation, or at steady state. Furthermore, no comprehensive study has been reported thus far on the behavior of weakly consolidated formations during a shut-in period, and the permanent induced geomechanical effects of injection.

CHAPTER 7. PORO-ELASTO-PLASTIC RESPONSE

The objective of this chapter is to examine geomechanics of high pressure injection – high enough to induce plasticity but not fracturing – in an isotropic, homogeneous unconsolidated rock layer. The chapter concentrates on fully penetrating wellbores, intended for relatively thin reservoir formations. The overall response of a geological formation to injection is indeed impacted by the behavior of the confining seal rock layers. This chapter focuses on unconsolidated formations confined by stiff seal rocks, where the ratio of formation bulk modulus to seal rock stiffness approaches zero. In such reservoirs, radial injection results in trivial strain components on the plane perpendicular to injection current (plane strain) (Chapter 5). Most previous studies on coupled rock-fluid interactions are in fact developed for plane strain conditions (Rice et al., 1976; Carter et al., 1982; Risnes st al., 1982; Detournay et al., 1988; Wang et al., 1991). The porous medium is assumed to be fully saturated and to follow a Mohr Coulomb failure criterion subsequent to failure.

The first part of this chapter involves a new axisymmetric fully coupled numerical model. A comprehensive assessment of pore pressures, stress patterns, and failure planes is performed for the entire transient period of an injection cycle. Multiple simulations with different geometry and mesh settings have been carried out to ensure independence of the qualitative observations with respect to the chosen geometry and mesh dimension. Results of a representative simulation are presented. The results not only provide good insight into geomechanics of injection operations below fracturing pressures, but also allow evaluation of fracture initiation in unconsolidated formations under plane strain settings.

The second part of this chapter includes the derivation of new poro-elasto-plastic analytical solutions for the three stress/strain components as a function of an arbitrary pore pressure function. The approach adopted for analytical derivations is similar to that of Risnes et al. (1982), where knowledge of principal planes is a priori, as yield functions are commonly expressed in terms of principal stresses. Unlike Risnes et al. (1982) who adopted elastic solutions to define principal planes in the plastic domain, thus disregarding plasticity impacts on in situ conditions in the elastic zone, in this study results from the fully coupled numerical simulations are adopted to determine principal planes. Finally, a novel methodology is proposed based on which new weakly-coupled poro-elasto-plastic analytical solutions are derived for all three stress/strain components within plastic and elastic domains. Solutions are verified against the fully coupled numerical simulations.

7.1 Numerical Simulation

7.1.1 Model Development

In order to simulate radial fluid injection from a fully penetrating wellbore into a confined unconsolidated geological formation, a tightly-coupled axisymmetric poro-elasto-plastic numerical model is developed using the explicit mode of FLAC3D. Flow and mechanical calculations are set to be performed in parallel to capture effects of fluid-solid interactions. Injection is introduced as point sources distributed throughout the thickness of the porous layer. Injection rate is chosen high enough to induce plasticity. To determine whether or not the formation has failed in a specific plane at a given location (to determine the extent of the plastic domain), a parameter named "Plasticity Factor" (*PF*) is introduced based on Mohr failure criterion and applied to the model.

$$PF = \frac{\tau}{\tau_f} = \frac{\tau}{C + \sigma' tan\varphi} \tag{57}$$

where φ and C are formation friction angle and cohesion respectively, τ is the acting shear at a given location, and τ_f is the shear strength at the same location according to the Mohr Coulomb criterion. Pressures, stress/strains, displacements, and *PF* values are recorded at different observation points during an entire transient period and at steady state. All results are normalized. Pore pressures and stresses are normalized in terms of the initial in situ stress. History results are normalized and presented with respect to a characteristic time factor, $T^* = ct/r_w^2$.

Various simulations using different mesh settings were carried out to ensure independence of the quantitative observations with respect to the mesh dimension. Results of one representative simulation are presented. To better evaluate near wellbore impacts of injection, mesh geometry is chosen to be finer at this location. In order to improve simulation accuracy at the borehole, the mesh is set in a manner such that the radial magnitude of the element adjacent to the wellbore is $r_w\pi/180$ times the slice angle. The far-field reservoir boundary is chosen to be $r_{out}/r_w = 40$, distant enough to avoid inducing near-wellbore effects. The rationale behind choosing a shorter reservoir extension compared to that of the poroelastic case scenario is to be able to evaluate the fully coupled poro-elasto-plastic behavior of the confined unconsolidated reservoir during an entire transient state of an injection cycle. This is not feasible for cases where the far-field reservoir boundary is chosen to be too distant from the injection source, as the run time of the fully coupled fluid-mechanical model is slow. Upper and lower boundaries are mechanically fixed in the vertical direction to replicate stiff seal rocks. The wellbore boundary is mechanically fixed in the radial direction to

prevent from inward movement of the formation during injection. A schematic of the geometry mesh is presented in Figure 7-1. Material properties of the unconsolidated sandstone layer are chosen based on typical data reported in the literature (Warren et al., 1997; Bloch et al., 2002). Model inputs are presented in Table 7-1.

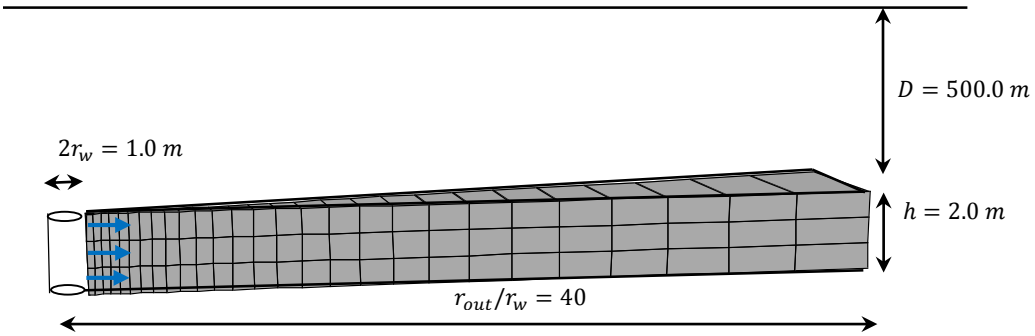

Figure 7-1. Schematic of the geometry mesh of numerical simulation (not to scale).

Table 7-1. Inputs of the numerical model.

Reservoir properties	
Density	19.0e3 *N/m*^{3}
At-rest earth pressure coefficient (K_0)	1.0
Porosity (n)	0.4
Elastic Properties	
Bulk Modulus (K)	11.8e7 *Pa*
Shear Modulus (G)	7.1e7 *Pa*
Mohr Properties	
Friction Angle(φ)	30°
Cohesion (C)	0.0
Plastic Properties	
Dilation Angle (ϑ)	20°
Flow properties	
Biot Coefficient (α)	1.0
Intrinsic Permeability (κ_{in})	3.0 *Darcy*
Fluid Bulk Modulus (K_f)	2.0e9 *Pa*
Fluid viscosity (μ)	9.93e-4 *Pa.sec*

7.1.2 Numerical Results and Discussion

Pore pressure history during the entire transient period of an injection cycle in the element adjacent to the injection wellbore is presented in Figure 7-2. A gradual increase in pore pressures is observed with injection initiation. A closer evaluation at early times (Graph 3.b) reveals two breaks on the graph (A_1 and A_2), after which a reduction in the pore pressure increase rate is detected. To further study this observation, effective stress histories along with Plasticity Factor variations in time are evaluated at the borehole (Figure 7-3).

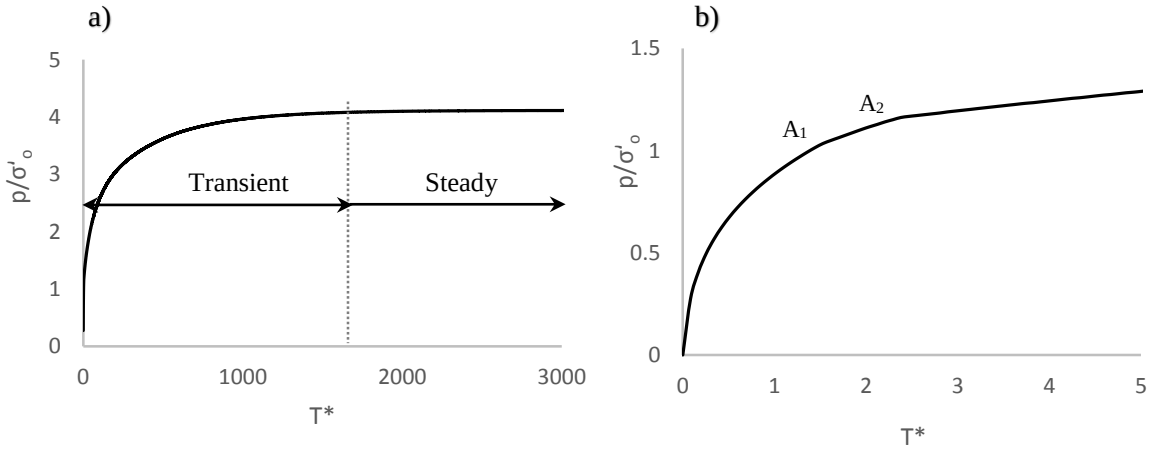

Figure 7-2. Normalized pore pressure history in the element adjacent to the borehole.

Figure 7-3 clearly illustrates a gradual decrease in effective stresses with injection initiation. In spite of an isotropic initial stress field, reduction in effective stresses is not identical in different directions, resulting in stress anisotropy at this early state: $\sigma_r' < \sigma_\theta' < \sigma_z'$. This induced anisotropy escalates up to a certain time (Point A_1), after which it attenuates. Point A_1 on the graph is suspected to correspond to initiation of shear failure due to the deviatoric stress induced in $r - z$ plane. As pore pressures accelerate in time, effective stresses at the borehole continue to decrease, approaching a zero state (Point A_2). This state of zero effective stress, zero stiffness and strength, is referred to as liquefaction. The plasticity factor history at the borehole further confirms these assertions. Graph 7-3 illustrates a rather quick growth in the Plasticity Factor with injection initiation, approaching unity at very early times and thus suggesting occurrence of shear failure (Point A_1). For a short period subsequent to failure initiation, *PF* remains constant after which becomes undefined (Point A_2). The reason behind this is the numerical instability caused by division of zero by zero at the moment of liquefaction. The rock matrix at the borehole does in fact continue to remain in the plastic state (liquefaction) as long as injection is sustained.

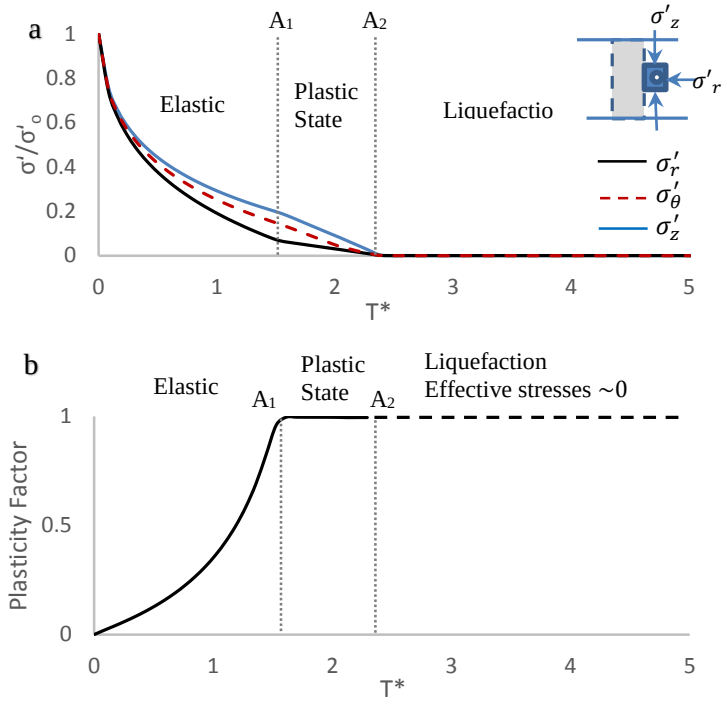

Figure 7-3. Time history results at the borehole: a) effective stress; b) Plasticity Factor.

Based on aforementioned observations, failure mechanisms near an injection borehole in an unconsolidated formation under plane strain conditions is shear, followed by liquefaction. Occurrence of liquefaction in an unconsolidated formation is an indication of fracture initiation (fracture tip). A comparison between Figure 7-2 and Figure 7-3 reveals that the first and second break detected on the pore pressure history at the borehole respectively corresponds to occurrence of shear failure and liquefaction at this location.

Total stress histories at the borehole are given in Figure 7-4. A gradual increase is observed in all three components of the total stress with injection initiation. The radial component of the total stress continues to grow during the transient period, as it is a direct function of radial injection. Once shear failure is initiated in the formation, vertical and tangential components of the total stress tend to decline, indicating a release in the reservoir formation. At the moment of liquefaction, stress components become equal, and increase identically during further injection.

To obtain a better understanding of reservoir behavior, stress paths at different observation points are computed using stress histories (Figure 7-5). For locations chosen near the injection borehole ($r/r_w =$

1.2 ,1.5), a continuous decrease in effective stresses and thus dilative behavior is detected with injection initiation. After failure onset – intersection of a stress path with the failure envelope – effective stresses continue to decrease along the yield envelope for the near borehole locations. In the case of high enough injection rates, the stress path at the wellbore will eventually approach zero, indicating a state of liquefaction and suggesting initiation of parting/fracture in the unconsolidated formation. As for more distant locations, even though an initial dilative behavior is detected with injection initiation, the corresponding stress paths change direction at some point during injection, demonstrating compaction.

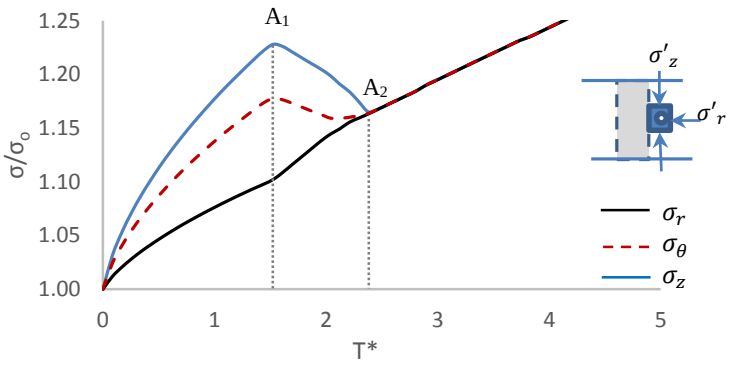

Figure 7-4. Normalized total stress histories during injection at the borehole.

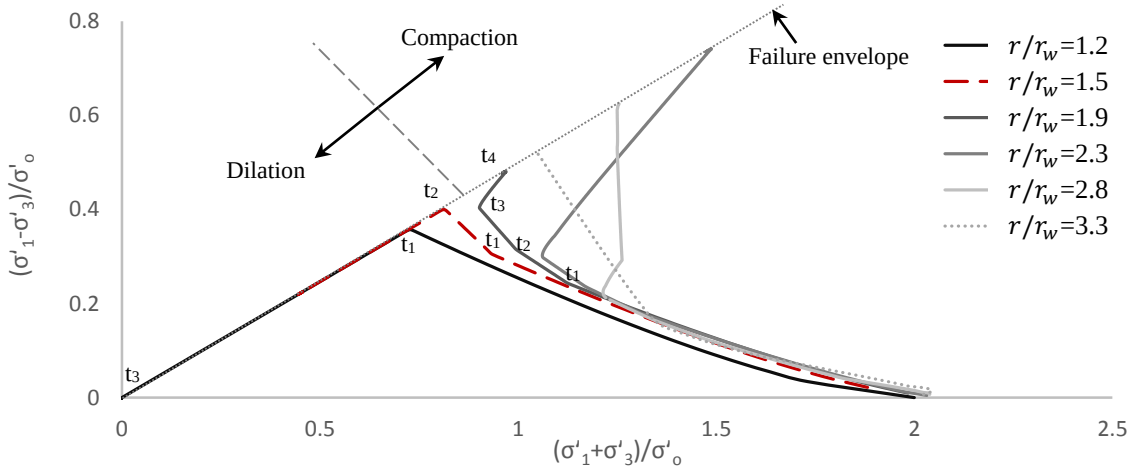

Figure 7-5. Stress path at different locations. t_1, t_2, t_3, t_4 correspond to the instance of: shear failure at wellbore, shear failure near the wellbore ($\boldsymbol{r/r_w = 1.5}$); liquefaction at wellbore; and shear failure in 3rd element ($\boldsymbol{r/r_w = 1.9}$).

This qualitative assessment of stress paths at different locations reveals two different patterns induced during injection: continuous reduction in effective stresses and a tendency towards liquefaction near the wellbore; and an eventual increase in effective stresses for other observation points, indicating compaction. Stress paths demonstrate generation of shear stresses throughout the entire formation, even at far field locations. This is due to anisotropic variations induced in effective stresses in a confined unconsolidated sand during radial injection.

A closer look at stress paths reveals multiple breaks on the graphs besides those of the failure onset state. Stress histories suggest these breaks correspond to occurrence of failure in the adjacent elements. In Figure 7-5, only breaks corresponding to the first three observation points are labeled: t_1, t_2, t_3, t_4 respectively correspond to onset of: shear failure at the wellbore, shear failure near the wellbore (2nd element), liquefaction at the wellbore, and shear failure in 3rd element. This observation confirms the influence of plasticity on conditions in the elastic domain.

Stress paths are further evaluated to obtain insight into the post-yield behavior of constrained unconsolidated sand under high injection pressures. Figure 7-5 demonstrates insignificant movement of stresses along the failure envelope subsequent to failure onset in all locations except for the first couple of elements near the wellbore where $r/r_w \leq 1.5$. This observation, which suggests minor stress variations post failure onset state, is adopted later in this chapter for the development of analytical solutions.

Propagation of the plastic domain during injection is evaluated by plotting the Plasticity Factor distribution at different times (Figure 7-6). For a particular injection rate in a reservoir with given geometry and geomechanical parameters, r_p reaches a certain value at pseudo steady state. The final extension of the plastic domain for this simulation is found to be $20r_w$.

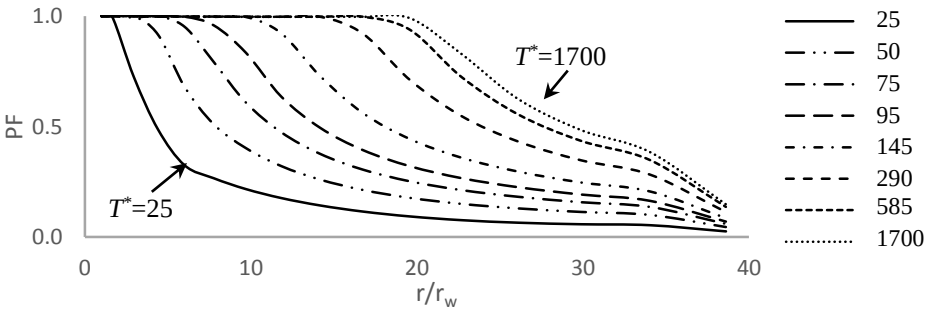

Figure 7-6. Plastic zone extension at different T^*.

Valuable information on the behavior of the rock matrix within the plastic domain can be obtained from tracking principal stresses, as they provide insight into failure planes. In order to track redirection of principal planes and to evaluate failure in the porous medium, Plasticity Factor histories are computed using stresses on the main planes in the cylindrical coordinate system ($PF_{r-\theta}, PF_{r-z}, PF_{\theta-z}$), and compared to values obtained from major and minor principal stresses (PF_{1-3}). Results indicate principal stresses to be along the main planes in the cylindrical coordinate system, as PF_{1-3} is identical to at least one of the computed *PF* curves using stresses on the main planes. A comprehensive assessment of *PF* histories at different locations throughout the reservoir formation reveals an extremely complex induced behavior, specifically within the plastic domain. In fact, results display development of five distinctive zones of various plasticity states during high pressure injection: wellbore surface where the soil matrix liquefies; two inner plastic domains where the formation fails along two planes and the major principal stress (σ_1') is in vertical direction (zone I, zone II); the rest of the plastic domain, where the formation fails along one plane of $r-\theta$ (zone III) and σ_1' is in radial direction; and the non-plastic region (zone IV).

Bratli et al. (1981), and Risnes et al. (1982) anticipated existence of an "inner plastic zone" surrounding a producing borehole, where two of the stress components (tangential and vertical) are bound to be identical. Results for our study indicate the presence of two inner plastic domains: the immediate area adjacent to the wellbore (zone I), where $\sigma_r' = \sigma_\theta'$; and a more distant region (zone II), where $\sigma_r' = \sigma_z'$. A schematic plan illustrating existence of the zones with dissimilar plasticity states during injection is presented in Figure 7-7 as well as *PF* histories obtained at five locations chosen in each zone.

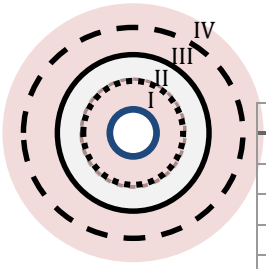

Zone	Major	Minor
Wellbore	$\sigma_r' \sim \sigma_\theta' \sim \sigma_z' \sim 0$	
I	σ_z'	$\sigma_r' = \sigma_\theta'$
II	$\sigma_r' = \sigma_z'$	σ_θ'
III	σ_r'	σ_θ'
IV	σ_r'	σ_θ'

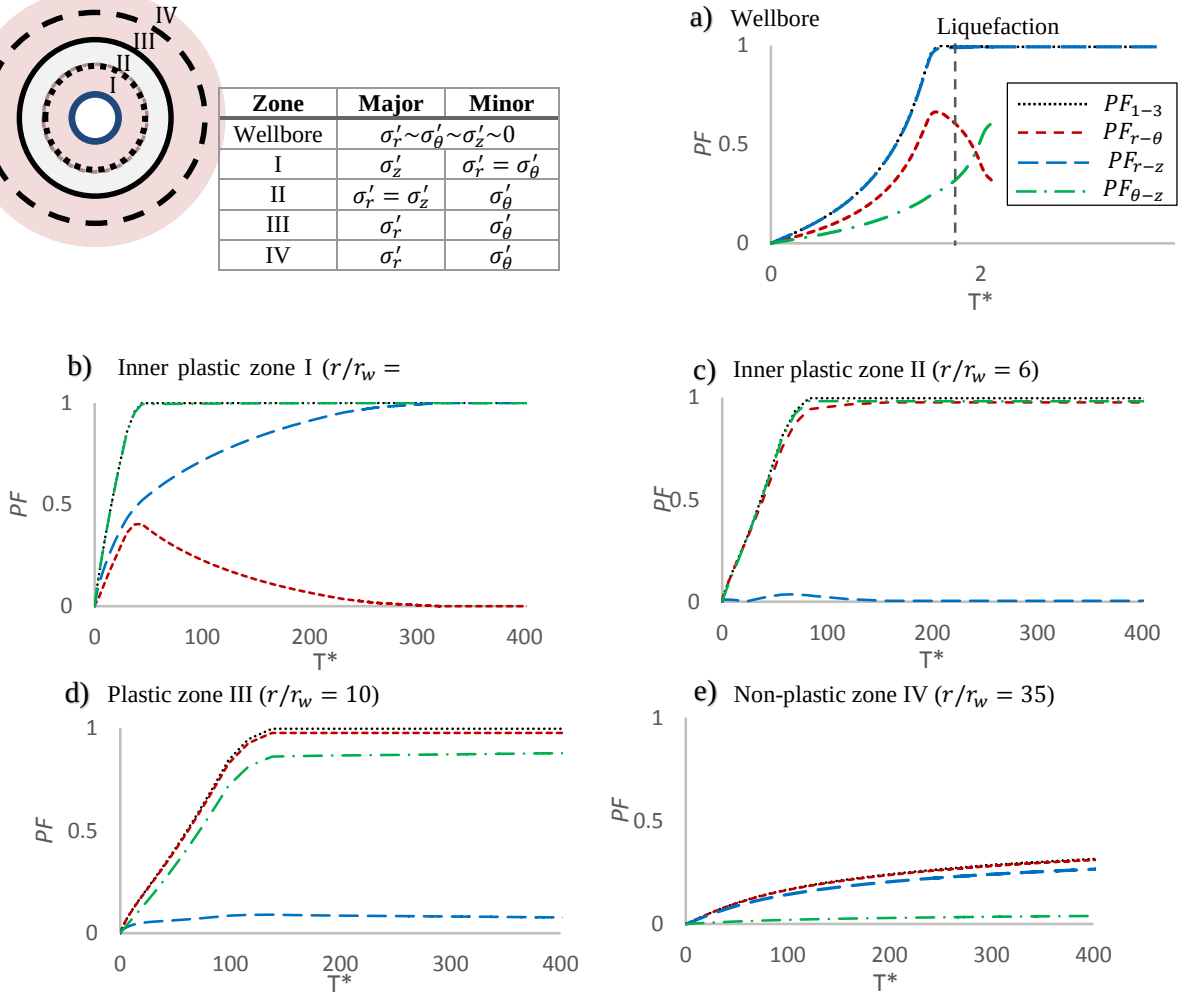

Figure 7-7. Development of different plasticity states during injection at various locations.

The development and propagation of regions with different plasticity states during injection is assessed in Figure 7-8. The graph clearly demonstrates initiation of shear failure at the wellbore at early times. Shortly after, the soil matrix at the wellbore experiences liquefaction ($\sigma'_\theta \sim \sigma'_r \sim \sigma'_z \sim 0$) and continuous to remain in the liquefied state as long as injection is sustained. Not long into the injection cycle, plasticity tends to propagate with an extension of r_p, wherein σ'_z is the major principal stress and σ'_r is the minor principal stress. A short time into the injection cycle, two inner plastic domains are formed in the immediate area surrounding the wellbore: zone I, where $\sigma'_\theta = \sigma'_r$; and zone II where $\sigma'_r = \sigma'_z$. The vertical effective stress component is the major principal stress within both inner plastic zones. Subsequent to formation of

the inner plastic regions surrounding the wellbore, σ'_r becomes the major and σ'_θ the minor principal stress in the remainder of the propagating plastic zone (zone III).

To further evaluate stress patterns during injection, effective stress distributions are examined at different times. Figure 7-9 and 7-10 respectively present effective stresses prior to and subsequent to the onset of liquefaction. Figure 7-9 suggests a gradual decrease in all effective stress components near the borehole with injection initiation. At this early state, two distinctive zones are quite evident throughout the reservoir formation: a dilation region in the immediate area surrounding the borehole which propagates over time; a compaction region subsequent to the dilated area. Figure 7-10 however, illustrates a much more complicated pattern after liquefaction. With respect to the horizontal effective stress components, a decrease is always detected in the immediate area surrounding the borehole throughout injection (dilation). As for the radial effective stress component, a compaction region is generated in the area adjacent to the dilated zone. The tangential component of effective stress however experiences a decrease pretty much all throughout the formation at all times. Contrary to the horizontal stress components, the vertical effective stress tends to notably increase, specifically near the borehole, subsequent to liquefaction initiation. An increase is detected in vertical effective stress components all throughout the reservoir formation at all times subsequent to liquefaction.

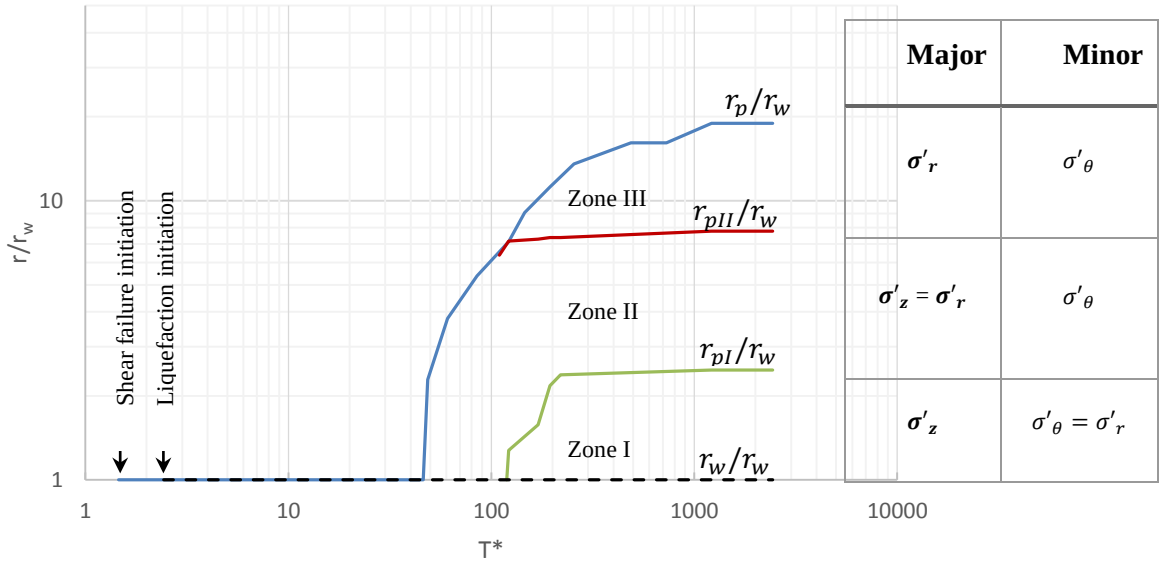

Figure. 7-8. Formation and propagation of zones with different plasticity states in time.

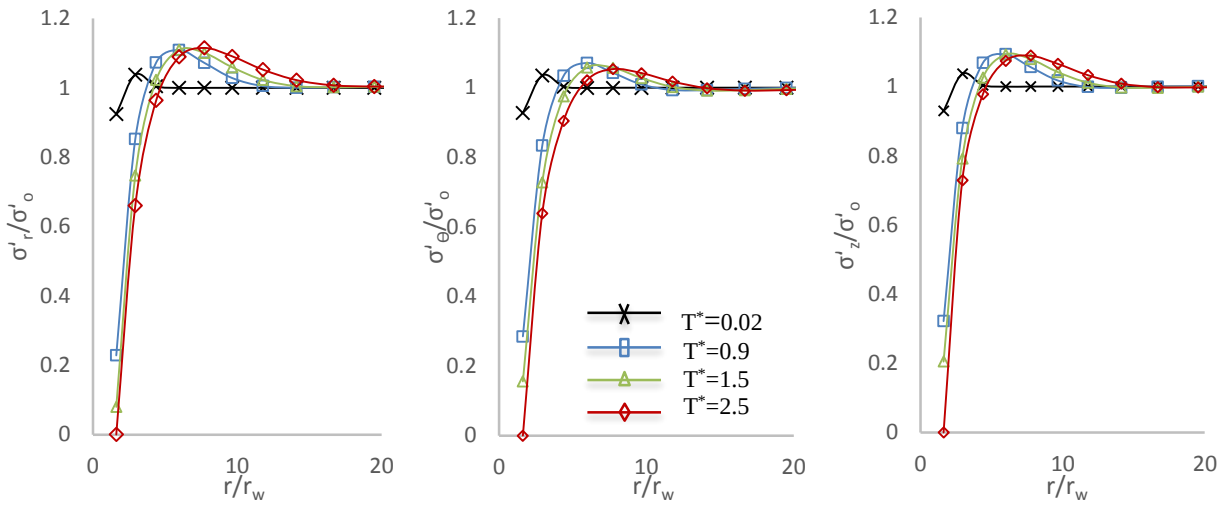

Figure. 7-9. Normalized effective stress distributions at different T^*, pre-liquefaction.

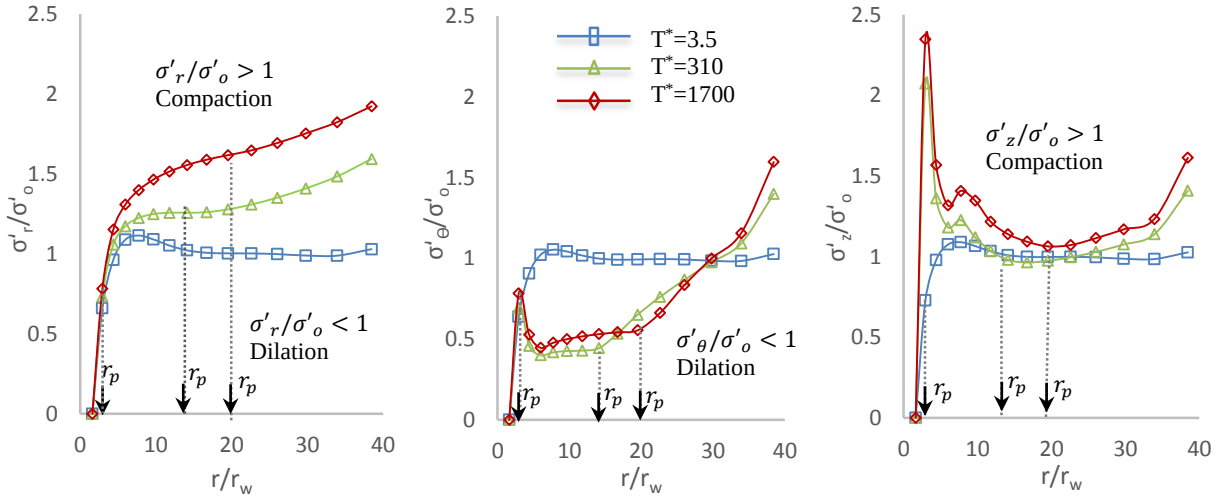

Figure. 7-10. Normalized effective stress distributions at different T^*, post-liquefaction.

The extent of the plastic domain (r_p) at different times is presented in Figure 7-10. A closer look at the plots reveals that the radial component of the effective stress is always continuous, specifically in the plastic domain. This is expected, as the radial stress is a direct function of induced pressures during radial injection. On the other hand, an apparent complicated pattern is detected with respect to tangential and vertical stress components, specifically within the plastic domain. An assessment of stresses together with principal and

failure planes at different times obtained from *PF* results suggests these complicated trends to be associated with different zones with dissimilar plasticity states induced in the porous medium during injection (I – IV). At a given time into the injection cycle, the sin situ tress pattern will be dissimilar even within the plastic domain itself. To better visualize stress patterns throughout the reservoir formation at a given time, the in situ stress field at steady state is presented in Figure 7-11. The boundaries between zones I – IV shown on the graph clearly illustrate the link between redirection of principal planes and the complicated stress trend specifically within the plastic domain.

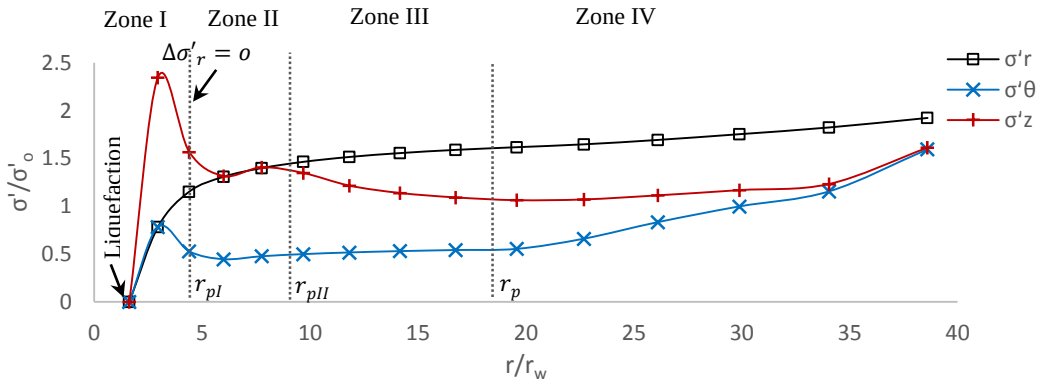

Figure 7-11. Normalized effective stress distribution at steady state *($T^* = 1700$)*.

An interesting detail is revealed by further evaluating σ'_r distributions at different times. A decrease in σ'_r is detected at all times in the immediate area surrounding the wellbore. As for the remainder of the formation, an increase in σ'_r takes place. The radial stress component is bound to be always continuous throughout the reservoir formation during radial injection. Inevitably, at any given time during injection, there is a location wherein the induced radial stress component is zero ($\Delta\sigma'_r = o$). In other words, during an injection process, there always exists a location where σ'_r is equal to the initial in situ stress. The area prior to this location experiences a decrease in σ'_r, whereas an increase in σ'_r takes place in the remainder of the medium. Stress pattern results at different times during injection suggest that the location of zero induced σ'_r corresponds to the boundary between the two inner plastic domains. This observation is of value specifically for analytical formulation, as will be demonstrated later on in this section 7.3.

7.2 Evaluation of the Simplified Pore Pressure Equation

The simplified pore pressure equation obtained for steady state (Eq. 56), is a common relation adopted in the literature for analysis of induced pore pressures during production or injection processes, and is also frequently applied in the field for control purposes. Applicability and limitations of the simplified theoretical logarithmic equation for estimating in situ pore pressures during high pressure injection are evaluated by comparing the theoretical values with those of the numerical models.

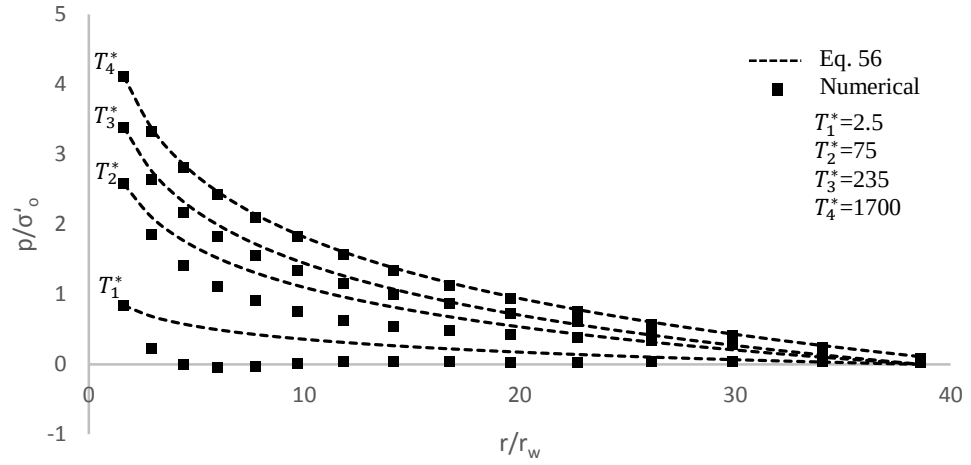

Figure 7-12. Normalized pore pressure distributions at different T^*.

Figure 7-12 indicates that the steady state solution overestimates pore pressures at early times when pressures have not yet propagated throughout the reservoir. Moreover, lower in situ pressures obtained from the coupled numerical model imply occurrence of volumetric expansion in the unconsolidated sand which is not incorporated in the steady state solution. Not long into the injection cycle, the formation slowly ceases to dilate as it is constrained. Due to this as well as an increase and propagation of the induced pore pressures, accuracy of Eq. 56 improves at longer times. A good approximation of in situ pore pressures in both elastic and plastic domains can be obtained via Eq. 56 long before steady state condition is reached. To evaluate the suitability of Eq. 56, the relative error of the analytical values (p_{anal}) is computed with respect to those of the numerical model (p_{num}) (Figure 7-13). Results suggest a good approximation of pore pressures using the steady state solution not long into the injection cycle.

$$err = (p_{anal} - p_{num})/p_{num} \tag{58}$$

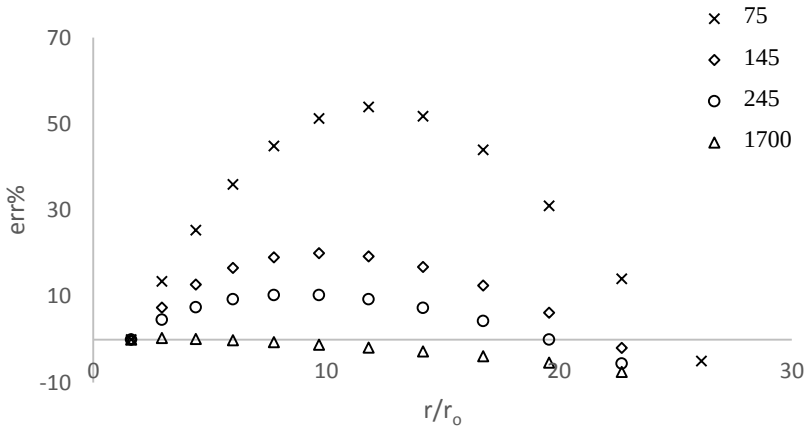

Figure 7-13. err % at different T^*.

7.3 Analytical Derivations

This section presents derivation of new poro-elasto-plastic analytical solutions for high pressure injection (without fracturing) in unconsolidated reservoirs under plane strain conditions. Rock characteristic parameters are presumed not to vary in time during injection. The stress dependent aspect of porosity and permeability in an unconsolidated porous layer can be assumed to be negligible when evaluated in terms of pore pressure variations as far as stress analysis is concerned (Han et al., 2003). The effect of gravity is not incorporated for simplicity. Compressive stresses and strains are taken as positive sign convention in this Chapter.

Governing equations are force balance and constitutive relations. In the cylindrical coordinate system, force balance along the horizontal plane results in Eq. 59:

$$\frac{d\sigma_r'}{dr} + \frac{\sigma_r' - \sigma_\theta'}{r} = -\alpha \frac{dp}{dr} \tag{59}$$

The time factor is not incorporated in this section to avoid further complications. Instead, calculations are performed for three states: elastic, failure onset, and plastic. At any given time or state, in situ stresses can be described in terms of an initial stress and an induced stress increment. Stresses at elastic, failure onset, and plastic states can therefore be respectively described as $\sigma_o' + \Delta\sigma'^e$; $\sigma_o' + \Delta\sigma'^y$; and $\sigma'^y + \Delta\sigma'^p$.

Here, $\Delta\sigma'^{e}$ is the induced elastic stress component, $\Delta\sigma'^{y}$ is the induced stress increment at failure onset state, σ'^{y} is effective in situ stress at failure onset, and $\Delta\sigma'^{p}$ is the plastic stress component.

Under plane strain conditions, radial displacement (u_r) can be related to strains via Eqs. 60.

$$\varepsilon_r^T = \frac{du_r}{dr} \tag{60.a}$$

$$\varepsilon_\theta^T = \frac{u_r}{r} \tag{60.b}$$

$$\varepsilon_z^T = 0 \tag{60.c}$$

where ε_r^T, ε_θ^T, and ε_z^T are total strain components in radial, tangential, and vertical directions respectively.

The analytical procedure involves describing the induced stress increments at each state (elastic, failure onset, plastic) in terms of an arbitrary pore pressure function. To effectively utilize the Mohr-Coulomb yield criterion for obtaining stress components in the non-elastic state, directions of principal stresses are to be defined. Results from the fully coupled numerical model presented is Section 7.1 are directly adopted to define principal planes during injection. Therefore, analytical derivations are carried out for two distinctive stress patterns in terms of the direction of σ_1': $\sigma_1' = \sigma_z', \sigma_3' = \sigma_\theta'$(near the borehole); $\sigma_1' = \sigma_r', \sigma_3' = \sigma_\theta'$(in the remainder of the formation). All possible failure planes are incorporated and corresponding stress solutions are obtained. Analytically computed stresses are then applied to define strain components using appropriate constitutive relations, based on which displacements are derived. Solutions are obtained with respect to stresses that are statically determinant, i.e. they satisfy the equation of equilibrium and the yield condition.

7.3.1 Elastic State

Hooke's law is applied to describe linear-elastic behavior of unconsolidated sand. Stress-strain relations in the elastic state are thus described as:

$$\varepsilon_{ij}^e = \frac{1}{E}\left[\Delta\sigma_{ij}'^{e} - v\left(\Delta\sigma_{kk}'^{e}\delta_{ij} - \Delta\sigma_{ij}'^{e}\right)\right] \tag{61}$$

$$\Delta\sigma'^{e}_{ij} = \frac{E}{1+v}\left[\varepsilon_{ij}^e + \frac{v}{1-2v}\varepsilon_{kk}^e\delta_{ij}\right] \tag{62}$$

As total strain is equivalent to the elastic strain increment in the elastic state ($\varepsilon^p = 0$), Eq. 60.c results in $\varepsilon_{zz}^e = 0$. Substituting constitutive expressions into the force balance equation and assuming constant $E$and v results in the following strain-pore pressure relation:

$$\frac{E}{1+v}\left[\frac{1-v}{1-2v}\frac{d\varepsilon_r^e}{dr}+\frac{v}{1-2v}\frac{d\varepsilon_\theta^e}{dr}+\frac{\varepsilon_r^e}{r}-\frac{\varepsilon_\theta^e}{r}\right]=-\alpha\frac{dp}{dr} \tag{63}$$

Replacing strains with equivalent displacement terms (Eqs. 60) results in the following displacement-pore pressure relation:

$$\frac{d^2\mathrm{u}_r}{dr^2}+\frac{1}{r}\frac{d\mathrm{u}_r}{dr}-\frac{\mathrm{u}_r}{r^2}=-\frac{\alpha}{F}\frac{dp}{dr} \tag{64}$$

where $F=\frac{E(1-v)}{(1+v)(1-2v)}$. The general solution of equation 65 can be described as:

$$\mathrm{u}_r(r)=C_1(r)r+\frac{C_2(r)}{r}$$

where $C_1(r)$ and $C_2(r)$ can be determined using the Wronski method (Appendix II). The general displacement-pore pressure relation in the elastic state is therefore derived to be:

$$\mathrm{u}_r(r)=\frac{\alpha}{2F}[-r\int\left(\frac{dp}{dr}\right)dr+\frac{1}{r}\int\left(r^2\frac{dp}{dr}\right)dr] \tag{65}$$

Stresses in the elastic state can subsequently be derived using Eqs. 65, 60, and 62.

7.3.2 Failure Onset

Stresses should satisfy the yield criterion at the failure onset state. The Mohr-Coulomb yield function for the unconsolidated sand is written as follows:

$$f=\sigma_1'-K_P\sigma_3'=0 \tag{66}$$

where K_P is the "passive earth pressure coefficient" and a function of the medium's friction angle ($K_P=(1+sin\varphi)/(1-sin\varphi)$).

a) $\boldsymbol{\sigma_r'>\sigma_z'>\sigma_\theta'}$

Applying Mohr-Coulomb failure criterion for $\sigma_1'=\sigma_r'$ and $\sigma_3'=\sigma_\theta'$ results in:

$$\Delta\sigma_\theta'^{y}=\frac{1}{K_P}\Delta\sigma_r'^{y}-(1-\frac{1}{K_p})\sigma_o' \tag{67}$$

Substituting Eq. 67 into the force balance relation results gives the following expression between the maximum elastic radial stress component and pore pressures:

$$\frac{d(\Delta\sigma_r'^y)}{dr}+\frac{\Delta\sigma_r'^y}{r}\left(1-\frac{1}{K_P}\right)=-\alpha\frac{dp}{dr}-\frac{\sigma_o'}{r}(1-\frac{1}{K_P}) \tag{68}$$

The maximum elastic radial stress increment is therefore solved to be:

$$\Delta\sigma_r'^y=-\frac{\alpha}{r^{\left(1-\frac{1}{K_P}\right)}}\int\left(r^{\left(1-\frac{1}{K_P}\right)}\frac{dp}{dr}\right)dr-\sigma_o' \tag{69}$$

In Eqs. 67 – 69, p is the pore pressure that results in failure initiation: $\sigma_r'^y+\sigma_o'=\sigma_r'^e+\sigma_o'$. This condition leads to the following relation through which p at failure onset could be determined:

$$\frac{\alpha}{2(1-v)}[\int\frac{dp}{dr}dr-\frac{1-2v}{r^2}\int(r^2\frac{dp}{dr})dr]=-\frac{\alpha}{r^{\left(1-\frac{1}{K_P}\right)}}\int\left(r^{\left(1-\frac{1}{K_P}\right)}\frac{dp}{dr}\right)dr-\sigma_o' \tag{70}$$

In order to compute the vertical stress component, the following two case scenarios are considered:

a.1) σ_z' also contributes to failure. Possible failure planes and corresponding σ_z' are:

i. $r-\theta$ and $z-\theta\rightarrow\sigma_z'=\sigma_r'$

ii. $r-\theta$ and $r-z\rightarrow\sigma_z'=\sigma_\theta'$

a.2) σ_z' doesn't contribute to failure. Plastic strain component in the vertical direction is therefore zero. Subsequently, $\varepsilon_z^e=0$. Constitutive relations thus result in:

$$\Delta\sigma_z'^y=v\left(\Delta\sigma_r'^y+\Delta\sigma_\theta'^y\right) \tag{71}$$

b) $\boldsymbol{\sigma_z'>\sigma_r'>\sigma_\theta'}$

Applying Mohr-Coulomb failure criterion for $\sigma_1'=\sigma_z'$ and $\sigma_3'=\sigma_\theta'$ gives the following:

$$\Delta\sigma_z'^y=K_p\Delta\sigma_\theta'^y+(K_p-1)\Delta\sigma_o' \tag{72}$$

In order to determine σ_r', the following case scenarios are considered:

b.1) σ_r' also contributes to failure. Possible failure planes, and the corresponding $\Delta\sigma_r'$ derived via Eq. 66, are presented in the following:

i. $z-r$ and $z-\theta\rightarrow\sigma_r'=\sigma_\theta'$

$$\Delta\sigma_r'^y=-\alpha\int\frac{dp}{dr}dr \tag{73}$$

ii. $r-\theta$ and $z-\theta \rightarrow \sigma_r' = \sigma_z'$

$$\Delta\sigma_r'^{y} = -\frac{\alpha}{r^{(1-K_P)}}\int\left(r^{(1-K_P)}\frac{dp}{dr}\right)dr - \sigma_o' \tag{74}$$

b.2) σ_r' does not contribute to failure. This stress pattern corresponds to the zone where induced radial stress is zero (boundary between the two inner plastic domains). The elastic strain component in radial direction is thus zero. Vertical and tangential stress components can therefore be derived via Eqs. 68 and 71.

$$0 = v\left(\Delta\sigma_z'^{y} + \Delta\sigma_\theta'^{y}\right) \tag{75}$$

7.3.3 Plastic State

Stress Calculations

a) $\boldsymbol{\sigma_r' > \sigma_z' > \sigma_\theta'}$

Applying the Mohr-Coulomb failure criterion and the force balance equation results in:

$$\Delta\sigma'^{p}_{r} = \frac{C(r)}{r^{\left(1-\frac{1}{K_P}\right)}} \tag{76}$$

where $C(r) = -\alpha\int\left(r^{\left(1-\frac{1}{K_P}\right)}\frac{dp}{dr}\right)dr - \int\left(r^{\left(1-\frac{1}{K_P}\right)}\frac{d\sigma'^{y}_{r}}{dr}\right)dr - (1-\frac{1}{K_P})\int\left(r^{-\frac{1}{K_P}}\sigma_r'^{y}\right)dr.$

As for the vertical stress, the following scenarios are considered:

a.1) σ_z' also contributes to failure. Possible failure planes are:

i. r – θ and z – $\theta \rightarrow \sigma_z' = \sigma_r'$

ii. r – θ and r – z $\rightarrow \sigma_z' = \sigma_\theta'$

a.2) σ_z' doesn't contribute to failure ($\varepsilon_z^e = \varepsilon_z^p = 0$). Eq. 61 is thus applied to derive σ_z'.

b) $\boldsymbol{\sigma_z' > \sigma_r' > \sigma_\theta'}$

The relation between σ_z' and σ_θ' is determined using Mohr failure criterion. With respect to radial stress, the following case scenarios are taken into account:

b.1) σ_r' also contributes to failure. Possible failure planes and the corresponding σ_r' are:

i. z – θ and r – z $\rightarrow \sigma_r' = \sigma_\theta'$

$$\Delta\sigma_r'^p = -\alpha \int \frac{dp}{dr} dr - \int \frac{d\sigma_r'^y}{dr} dr \tag{77}$$

ii. z – θ and r – $\theta \rightarrow \sigma_r' = \sigma_z'$

$$\Delta\sigma_r'^p = -\frac{\alpha}{r^{1-K_P}} \int \left(r^{(1-K_P)} \frac{dp}{dr} \right) dr - \frac{1-K_P}{r^{1-K_P}} \int (r^{-K_P}\, \sigma_r'^y) dr - \frac{1}{r^{1-K_P}} \int \left(r^{(1-K_P)} \frac{d\sigma_r'^y}{dr} \right) dr \tag{78}$$

b.2) σ_r' doesn't contribute to failure. The solution is then identical to that of Section 7.3.2 – b.2.

Displacement Derivation

Most geotechnical materials, specifically sand, follow the non-associative flow rule. The plastic potential function differs from the yield function in these materials. An appropriate potential function must therefore be defined to determine stress-strain relations in the plastic state using the flow rule. In case of sand, the following relation is commonly applied as the potential function:

$$g = \sigma_1' - K_D \sigma_3' \tag{79}$$

where K_D is a function of the soil's dilation angle, determined through experimental tests. Typically, $K_D < K_P$. Applying $K_D = K_P$ results in over prediction of volumetric strains.

In order to compute displacements, both elastic and plastic strain increments must be defined. Therefore, the first step in calculating displacements involves determining an appropriate potential function using proper stress patterns. If a principal stress doesn't contribute to failure, the plastic component of the corresponding strain would be zero. ε^p is otherwise defined using the flow rule. Once strain components are determined, displacement-stress relations are derived for each zone. Finally, general $u - p$ equations are defined using the derived stress equations. Solutions obtained for different possible stress patterns are presented next.

a) $\sigma_z' \geq \sigma_\theta' > \sigma_r'$

The following relations are derived for plastic strain components using the flow rule:

$$\varepsilon_r^p = \lambda \frac{\partial g}{\partial \sigma_r'} = -K_D \lambda \tag{80.a}$$

$$\varepsilon_\theta^p = \lambda \frac{\partial g}{\partial \sigma'_\theta} = \lambda \tag{80.b}$$

where λ is a nonnegative scalar factor. Displacements are related to strains as follows:

$$\frac{\partial \mathrm{u}_r}{\partial r} = \varepsilon_r^e - K_D \lambda \tag{81.a}$$

$$\frac{\mathrm{u}_r}{r} = \varepsilon_\theta^e + \lambda \tag{81.b}$$

It can be demonstrated that the general displacement-strain equation is derived to be:

$$\frac{\partial \mathrm{u}_r}{\partial r} + K_D \frac{\mathrm{u}_r}{r} = \varepsilon_r^e + K_D \varepsilon_\theta^e \tag{82}$$

Substituting the elastic strain components in Eq. 83 with equivalent stress terms and solving the subsequent differential equation results in the general displacement-stress equation:

$$\mathrm{u}_r(r) = \frac{A_1}{E r^{K_D}} \int_{r_o}^{r} (\Delta \sigma'_r r^{K_D}) dr + \frac{A_2 \sigma'_o}{E r^{K_D}} \int_{r_o}^{r} r^{K_D} dr \tag{83}$$

where $A_1 = 1 - vK_D + K_p(K_D - 2v - vK_D)$; and $A_2 = (K_D - 2v - vK_D)(K_P - 1)$.

b) $\boldsymbol{\sigma'_z > \sigma'_\theta = \sigma'_r}$

Displacement-strain relations in vertical and tangential directions are derived using the flow rule:

$$0 = \varepsilon_z^e + \lambda \tag{84.a}$$

$$\frac{\mathrm{u}_r}{r} = \varepsilon_\theta^e - K_D \lambda \tag{84.b}$$

It can be demonstrated that the displacement-stress equation is as follows:

$$\mathrm{u}_r(r) = \frac{r}{E}[A_3 \Delta \sigma'_r + A_4 \sigma'_o] \tag{85}$$

where $A_3 = 1 - v - 2vK_D + K_p(K_D - v)$; and $A_4 = (K_D - v)(K_p - 1)$.

c) $\boldsymbol{\sigma'_z > \sigma'_r > \sigma'_\theta}$

Variations induced in the radial stress component are minimal in this domain. This is in fact the boundary between the two inner plastic domains. The zone located in front of this region experiences dilation; the adjacent zone located beyond this area experiences compaction. It is can thus be interpreted

that ε_r^e is zero in this zone. Elastic and plastic strain components are derived using Hooke's law and the flow rule for the given stress pattern. The following displacement-strain relations are determined in tangential and vertical directions.

$$\frac{\mathrm{u}_r}{r} = \varepsilon_\theta^e - K_D\lambda \tag{86.a}$$

$$0 = \varepsilon_z^e - \lambda \tag{86.b}$$

It can be demonstrated that:

$$\mathrm{u}_r(r) = \frac{r\sigma_o'}{E}\left[\frac{1-K_P}{1+K_P}\left(1-vK_D+K_P(K_D-v)\right)+(K_P-1)(K_D-v)\right] \tag{87}$$

d) $\boldsymbol{\sigma_z' = \sigma_r' > \sigma_\theta'}$

Displacement distribution equation for this given stress pattern is derived via a similar approach.

$$\mathrm{u}_r(r) = \frac{A_5}{EK_D r^{\frac{1}{K_D}}}\int \Delta\sigma_r' r^{\frac{1}{K_D}}\,dr + \frac{A_6\sigma_o'}{EK_D r^{\frac{1}{K_D}}}\int r^{\frac{1}{K_D}}\,dr \tag{88}$$

where $A_5 = K_D - vK_D - 2v + \frac{1}{K_P}(1-vK_D)$; $A_6 = (1-vK_D)(1-K_P)$

e) $\boldsymbol{\sigma_r' > \sigma_z' > \sigma_\theta'}$

The general displacement equation for this zone is identical to equation 84. Constants A_5 and A_6 are however different and derived to be $A_5 = K_D - v + \frac{1}{K_P}(1-vK_D) - v^2(1+K_D)\left(1+\frac{1}{K_P}\right)$; $A_6 = (1-vK_D)\frac{(1-K_P)}{K_P} - \frac{v^2}{K_P}(1-K_P)(1+K_D)$

7.4 Weakly-Coupled Analytical Solutions

In section 7.3, general elasto-plastic analytical solutions were derived based on an arbitrary pore pressure function for different stress patterns, and taking into account all possible failure planes. In this section, a novel methodology is presented based on which specific analytical solutions are obtained for stresses and displacements throughout an unconsolidated reservoir formation during fluid injection under plane strain conditions. Solutions are obtained for times when the two inner plastic domains have already been generated surrounding the wellbore. Formulations from the failure onset state are adopted to describe stresses and strain within the plastic region, based on observations from fully coupled numerical models which suggest insignificant variations of stresses subsequent to failure onset. In order to be able to derive

closed-form solutions, the simplified logarithmic equation 56 is applied as the pore pressure function. The rationale behind this simplification is that a good approximation of pore pressures can still be obtained not long into the injection cycle due to the porous layer being constrained (Figure 7-12 and Figure 7-13). It should be noted that many of the previous studies on coupled soil-fluid interactions are developed based on this logarithmic equation which is obtained for steady state (Risnes et al., 1982; Hsiao 1988; Smith 1988; Wang et al., 1991; Han et al., 2003).

Failure planes and stress patterns in each inner plastic domain differ from one another and from the remaining of the plastic region. Therefore, radii of inner plastic zones (r_{pI}, r_{pII}) must be determined for correct utilization of the yield function to be able to obtain stress components throughout the plastic domain. Numerical results suggest the induced radial stress to be zero at the boundary between the two inner plastic domains. Radial stress distribution, being always continuous throughout the reservoir formation, can be analytically computed from the equilibrium equation and the yield function. Therefore, the extension of zone I (r_{P1}) is simply obtainable from σ_r' ($\sigma_r'(r = r_{p1}) = \sigma_o'$). Determination of the exact extent of zone II using analytical calculations is practically impossible. Nevertheless, stress pattern results obtained from coupled numerical models suggest that radial and tangential stress solutions are identical in zones II and III, as they remain to be major and minor principal stresses correspondingly in the two domains. Therefore, σ_r' and σ_θ' are determined using equations 59 and 66 throughout zones II and III. Complete solutions are thus obtainable for these two stress components throughout the plastic domain. It is the vertical stress component however, that differs in these two regions. σ_z' is statically indeterminate in zone III. Consequently, a numerical approach is required for exact determination of the stress component in the vertical direction. However, σ_z' in zones II and III will be in the range between two sets of solutions: the upper bound solution, which corresponds to when σ_z' contributes to failure (zone II; $\sigma_z' = \sigma_r' > \sigma_\theta'$); and the lower bound solution, corresponding to when σ_z' doesn't contribute to failure (zone III; $\sigma_r' > \sigma_z' > \sigma_\theta'$).

Complete derived analytical solutions are presented as follows.

A. Elastic zone ($r \geq r_p$)

$$\mathrm{u}(r) = -\frac{\alpha B}{2}\frac{(1+v)(1-2v)}{E(1-v)}\left[-r\ln(r) - rG_1 + \frac{r}{2} + \frac{G_2}{r}\right] \tag{89}$$

$$\Delta\sigma_r^{e\prime} = -\frac{\alpha B(1-2v)}{2(1-v)}\left[-\ln(\mathrm{r}) - 0.5 - \mathrm{G}_1 - \frac{\mathrm{G}_2}{r^2} + \frac{v}{1-2v}(-2\ln(r) - 2G_1)\right] \tag{90}$$

$$\Delta\sigma_\theta^{e\prime} = -\frac{\alpha B(1-2v)}{2(1-v)}\left[-\ln(\mathrm{r}) + 0.5 - \mathrm{G}_1 + \frac{\mathrm{G}_2}{r^2} + \frac{v}{1-2v}(-2\ln(r) - 2G_1)\right] \tag{91}$$

$$\Delta\sigma_z^{e\prime} = -\frac{\alpha B v}{2(1-v)}[-2\ln(\mathrm{r}) - 2\mathrm{G}_1] \tag{92}$$

B. Plastic region ($r \le r_p$)

I. σ_r'

$$\Delta\sigma_r^{p\prime} = -\frac{\alpha B}{\left(1-\frac{1}{K_P}\right)}\left[1-\left(\frac{r_o}{r}\right)^{\left(1-\frac{1}{K_P}\right)}\right] - \sigma_o' \tag{93}$$

II. σ_θ'

a. $r < r_{p1}$

$$\Delta\sigma_\theta^{p\prime} = \alpha B[\ln(r) + d] \tag{94}$$

d is determined using boundary condition at the wellbore.

b. $r = r_{p1}$

$$\Delta\sigma_\theta^{p\prime} = -\left(\frac{K_P-1}{K_P+1}\right)\sigma_o' \tag{95}$$

c. $r_{p1} < r \le r_p$

$$\Delta\sigma_\theta^{p\prime} = \frac{\alpha B}{K_P-1}\left[1-\left(\frac{r_o}{r}\right)^{1-\frac{1}{K_P}}\right] - \sigma_o' \tag{96}$$

III. σ_z'

a. $r < r_{p1}$

$$\Delta\sigma_z^{p\prime} = (K_P-1)\sigma_o' + K_P\Delta\sigma_r' \tag{97}$$

b. $r = r_{p1}$

$$\Delta\sigma_z' = \left(\frac{K_P-1}{K_P+1}\right)\sigma_o' \tag{98}$$

c. $r_{p1} < r \le r_p$

– Upper bound solution: σ'_z fails $\rightarrow \sigma'_z = \sigma'_r$

$$\Delta\sigma_z' = \frac{\alpha B}{1-\frac{1}{K_P}}\left[1-\left(\frac{r_o}{r}\right)^{1-\frac{1}{K_P}}\right] - \sigma_o' \tag{99}$$

– Lower bound solution: σ_z' doesn't fail:

$$\Delta\sigma_z' = \frac{v\alpha B}{1-\frac{1}{K_P}}\left[1-\left(\frac{r_o}{r}\right)^{1-\frac{1}{K_P}}\right]\left(1+\frac{1}{K_P}\right)-2v\sigma_o' \tag{100}$$

In the above equations, G_1 and G_2 are integral constants, and $B = Q_o/(2\pi hk)$. The common approach adopted in previous studies for examination of the behavior of unconsolidated media under high induced pressures is to independently determine stress-strain relations in plastic and elastic domains. r_p is then computed as the intersection of the independently driven elastic and plastic stress solutions. However, this approach is not accurate, as plasticity in a location has a clear effect on stresses in the subsequent domain. In situ conditions in the elastic region are thus indeed dependent upon the extension of the plastic zone. Therefore, the general poro-elasto-plastic analytical solution for unconsolidated reservoirs under high injection pressures involves determining three unknowns: r_p, G_1, and G_2. These parameters can be determined via boundary conditions: radial and tangential stresses should satisfy the Mohr-Coulomb yield criterion at the boundary between plastic and elastic domains ($@\, r = r_p: \sigma'^{e}_{r} = \sigma'^{p}_{r}; \sigma'^{e}_{\theta} = \sigma'^{p}_{\theta}$), and displacements should approach zero at far field ($\mathrm{u}(r_{out}) = 0$).

Even though it appears that a time factor is not taken into account in equations 89 – 100, these relations in fact estimate stresses, displacements, and r_p at any given time subsequent to generation of the inner plastic domains, based on the pore pressure at the wellbore. The impact of time in above equations is implicitly incorporated in Q, which at any given time can be calculated using equation 56 once the pore pressure at the wellbore is known.

7.5 Verification of Analytical Solutions versus Numerical Model

The weakly-coupled analytical solutions (equations 89 – 100) are compared against fully coupled numerical models for verification. Figure 7-14 to Figure 7-16 illustrate numerical and analytical stress results during fluid injection at a given time near steady state, when the plastic domain has well been established.

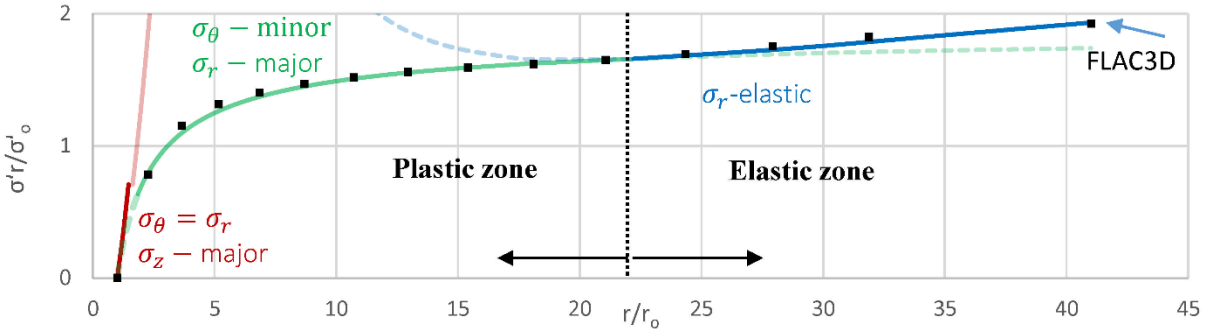

Figure 7-14. Normalized σ'_r distribution.

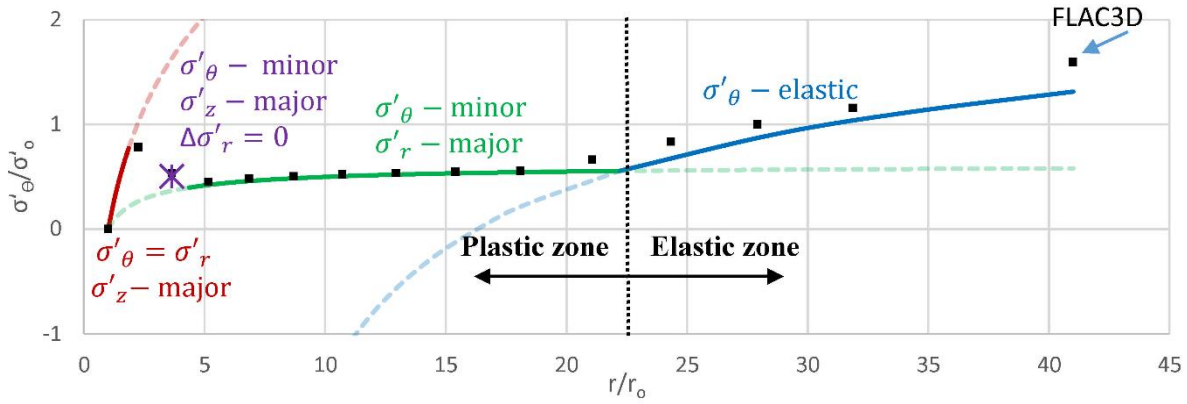

Figure 7-15. Normalized σ'_θ distribution.

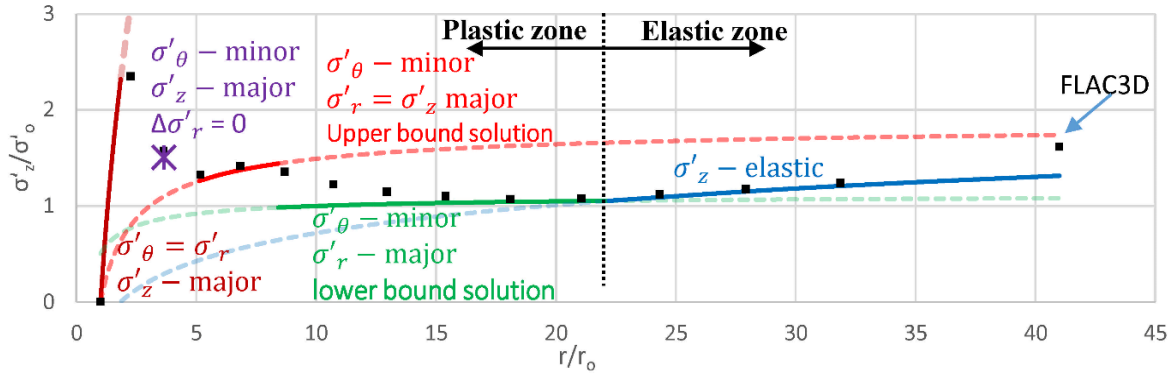

Figure 7-16. Normalized σ'_z distribution.

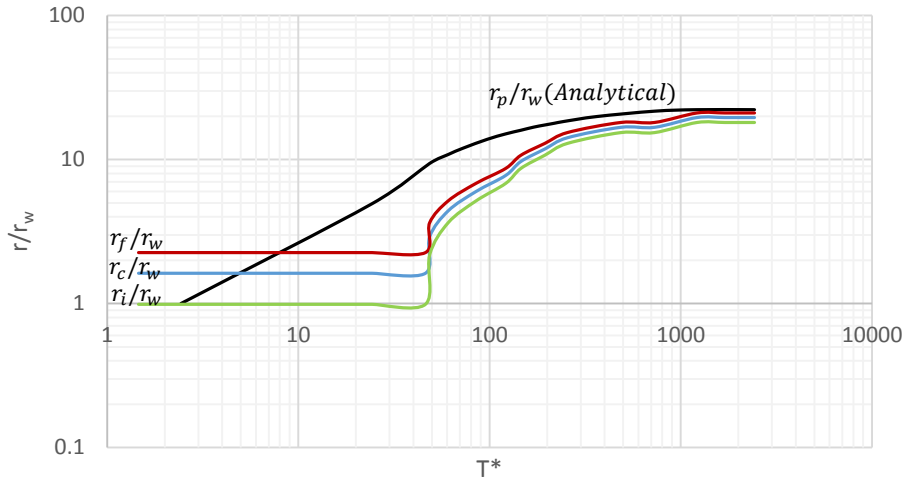

Figure 7-17. Extension of plastic region during the transient state of injection cycle.

The final extent of the plastic domain at steady state derived from the analytical solution is found to be $22r_w$, which is a good approximation of that of the numerical model. Figure 7-17 illustrates analytical propagation of the plastic zone computed using wellbore pressure at different T^*, and the corresponding numerical values obtained from *PF* distributions. r_p obtained from numerical results represents the center of the grid element throughout which failure has occurred. For better comparison, the starting point (r_i), center location (r_c), and end point (r_f) of the element which represents the boundary between plastic and elastic domains are shown in Figure 7-17. Figure 7-17 clearly indicates an over-estimation of the extent of the plastic domain using analytical calculations, particularly at early times into the injection cycle. This is due to lower numerical pressures at early times compared to those computed from equation 56, as coupled pressure-strain relations resulting in formation dilation are neglected in the equation. However, after a short period into the injection cycle, the formation ceases to dilate, as it is constrained, and numerical pressures approach the analytical values. At this state, r_p obtained from analytical calculations becomes a good approximation of that of the numerical model.

With respect to displacement distributions, analytical solutions are presented at two different states during the injection cycle: Failure initiation state, which in this study refers to the instant when failure initiates at the wellbore; and steady state. At the failure initiation state, elastic solutions are valid throughout the reservoir formation. In order to determine displacements, the correct pore pressure distribution must be determined. Numerical results at early times after injection initiation suggest generation of a high pressure gradient at the wellbore (Figure 7-12). The induced pressures are approximately zero in the remainder of

the reservoir formation. Pore pressure distribution at failure initiation state can be still be approximated using the logarithmic equation as follows:

$$\begin{cases} p(r) = p_o - \dfrac{Q_o}{2\pi Hk}\ln\left(\dfrac{r}{r_o}\right) & r \le r^* \\ p(r) = 0 & r > r^* \end{cases} \tag{101}$$

where r^* is the location wherein pressure drops to zero. In order to analytically replicate the numerical pressure distribution at the early state, $r^*$is determined numerically. Analytical and numerical pore pressures and displacements at failure initiation state are presented in Figure 7-18. Results indicate an acceptable approximation of the peak displacements in the numerical model using this analytical approach.

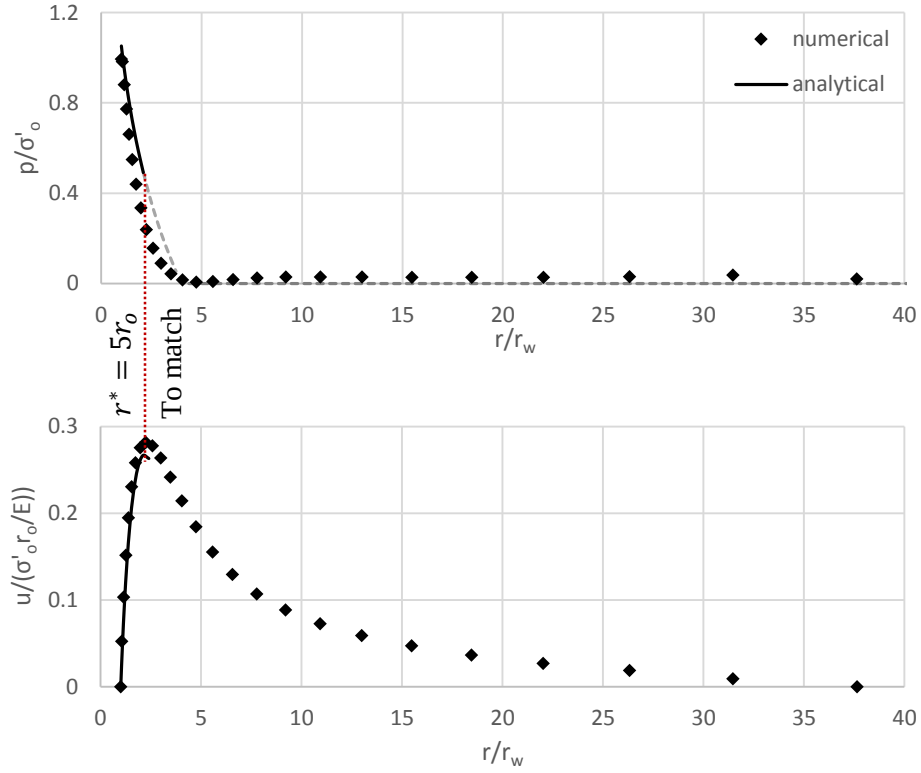

Figure 7-18. Normalized pore pressure and displacement distribution at the early state.

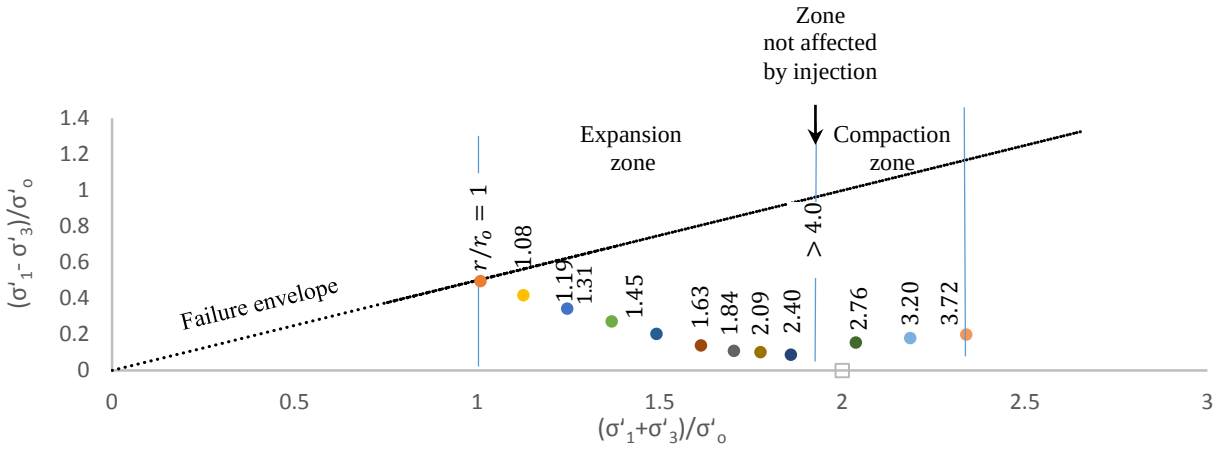

Figure 7-19. A snapshot of stress state at different observation points at failure initiation state.

Error! Reference source not found. presents a snap shot of the analytical stress state at different locations omputed using equations 101 for pore pressures. Results clearly illustrate a dilated zone located in the immediate area surrounding the wellbore, followed by a compaction region. Farther locations ($r/r_w > 4$) are not yet impacted by injection at this early state.

Figure 7-20 illustrates numerical displacements at steady state along with the values obtained from the analytical solutions. Results suggest a good accordance between the weakly-coupled analytical equations and the fully-coupled numerical results.

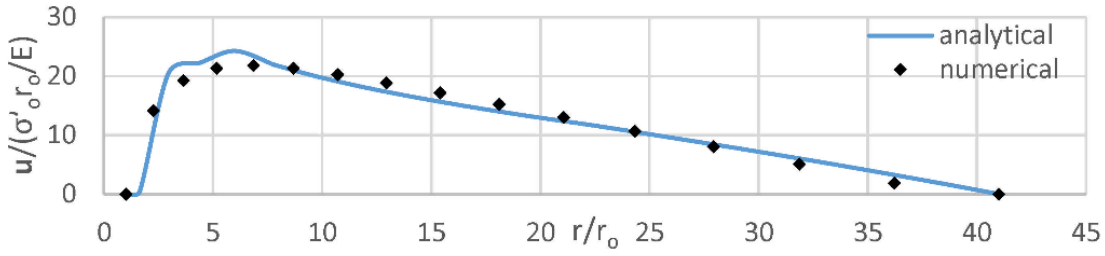

Figure 7-20. Normalized radial displacement distribution at steady state.

CHAPTER VIII

8. Post-Injection Behavior

No comprehensive study has been reported thus far on the fundamental geomechanics of a reservoir in the post-injection condition, and permanent induced effects of high pressure injection operations in weakly consolidated media. The objective of this chapter is to numerically evaluate variations in stresses, strains, displacements, and pore pressures throughout an unconsolidated reservoir formation confined with stiff seal rocks. More specifically, geomechanical processes within the plastic domain are of interest.

The same numerical model developed in section 7.1 is adopted for evaluating the post-injection behavior of unconsolidated reservoirs under plane strain settings. Results presented in this section are those of the shut in period subsequent to the injection cycle presented in section 7.1. After a period of $T^{*}=17021$, injection was ceased. Stresses, displacements, plasticity factor, and pore pressures were monitored until complete dissipation of the induced pressures ($T^{*} = 19452$) referred to as "*final state*" in this section.

Figure 8-1 illustrates pore pressure histories at different observation points during an entire transient state of injection cycle, at steady state, and during the shut-in period. The results show a rapid decline in the in situ pore pressures immediately after injection is ceased.

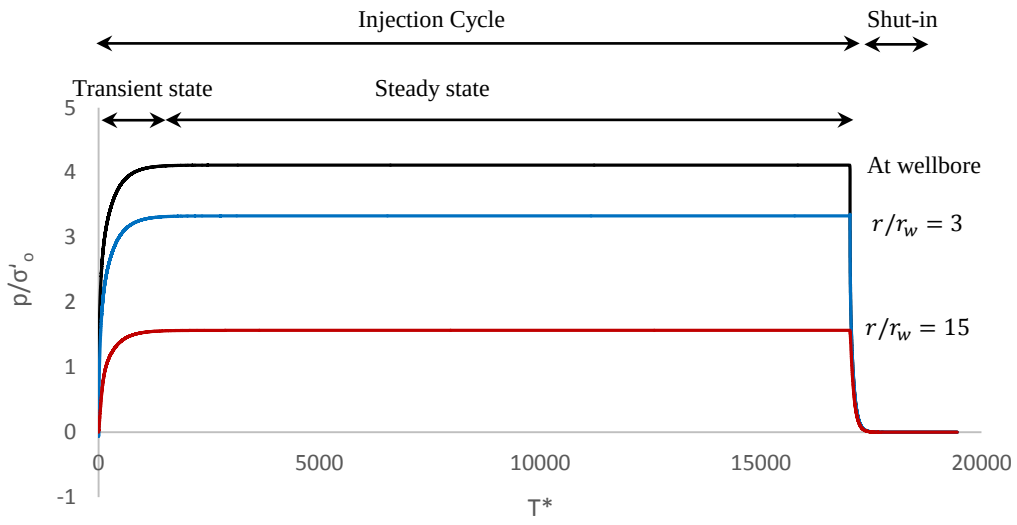

Figure 8-1. Normalized pore pressure histories at different observation points during: transient state of injection cycle, steady state, shut-in period.

To better evaluate pore pressure variations throughout the reservoir formation during the shut-in period, pore pressure distributions at different times are plotted in Figure 8-2. Results clearly illustrate a pore pressure drop in an adjacent area surrounding the wellbore immediately after injection is ceased. It takes a longer time for pore pressures to tend to drop at more distant locations. Theoretical pore pressure values computed using the simplified equation 56 are also plotted in Figure 8-2. Results indicate that adopting this uncoupled equation results in an under-estimation of pore pressures during the shut-in period.

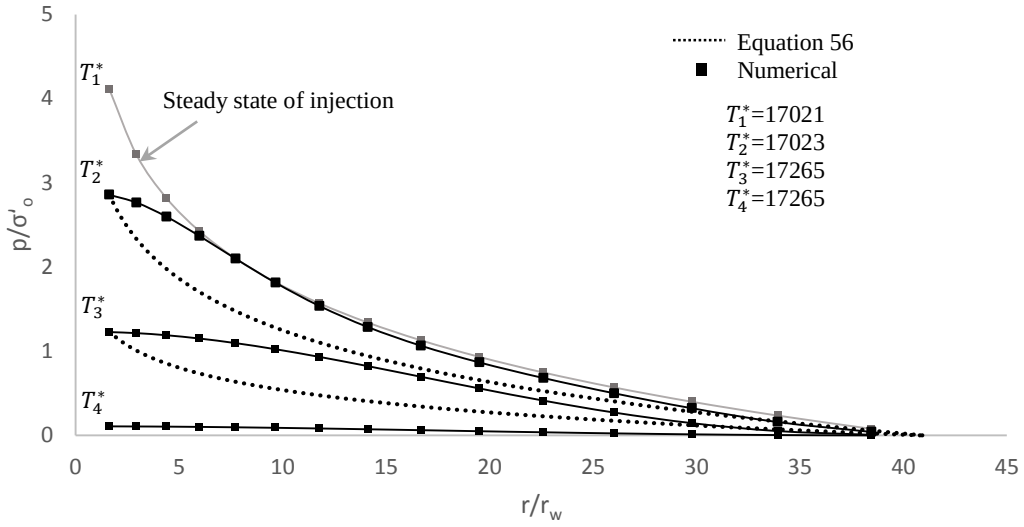

Figure 8-2. Normalized pore pressure distributions at different times during the shut-in period.

Effective stress histories during the shut-in period at different observation points are presented in Figure 8-3. For the location chosen at the wellbore wherein liquefaction had taken place during the injection cycle, an anisotropic increase in effective stresses takes place once injection is ceased. The maximum and minimum principal stresses at the wellbore at the *final state* are detected to be in the radial and vertical directions respectively. As for farther locations, a sudden slight decrease in effective stresses is observed at the moment when injection is ceased. This sudden slight decrease in effective stresses is suspected to be caused as a result of equalization of pore pressures within the formation once injection is halted. After injection is ceased, pore pressures in the immediate area surrounding the well will rapidly drop while the excess pore pressures continue to propagate to farther locations. This results in equalization of the in situ pore pressures. Notable anisotropy in the stress field is observed at different locations in the *final state*.

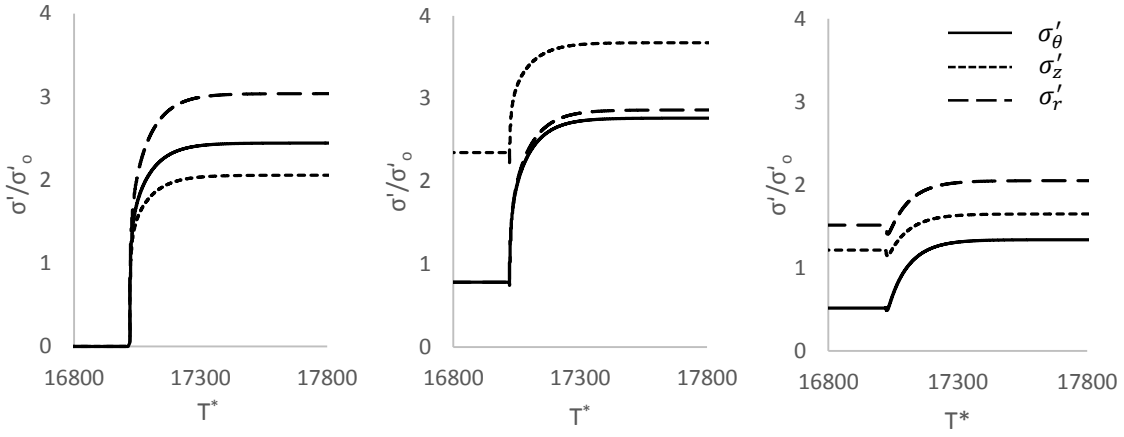

Figure 8-3. Normalized effective stress histories at: a) wellbore, b: $\boldsymbol{r/r_w = 3}$, c) $\boldsymbol{r/r_w = 15}$.

To better evaluate stress variations throughout the reservoir formation subsequent to the injection cycle, effective stress distributions during the shut-in period are presented in Figure 8-4. Results clearly illustrate occurrence of a significant increase in effective stresses once injection in stopped, specifically within the region which was once the plastic domain during the injection cycle. Stress distributions at the final state suggest higher in situ stresses in the once plastic region compared to the initial in situ stress (σ'_o). It is therefore concluded that, in spite of an initial isotropic stress field, a permanent anisotropy is induced due to high injection pressures explicitly within the plastic domain. Effective stresses at the *final state* in the area subsequent to the plastic region are found to be roughly equal to σ'_o. The highest effective stresses in the final state are observed to be in the vertical plane.

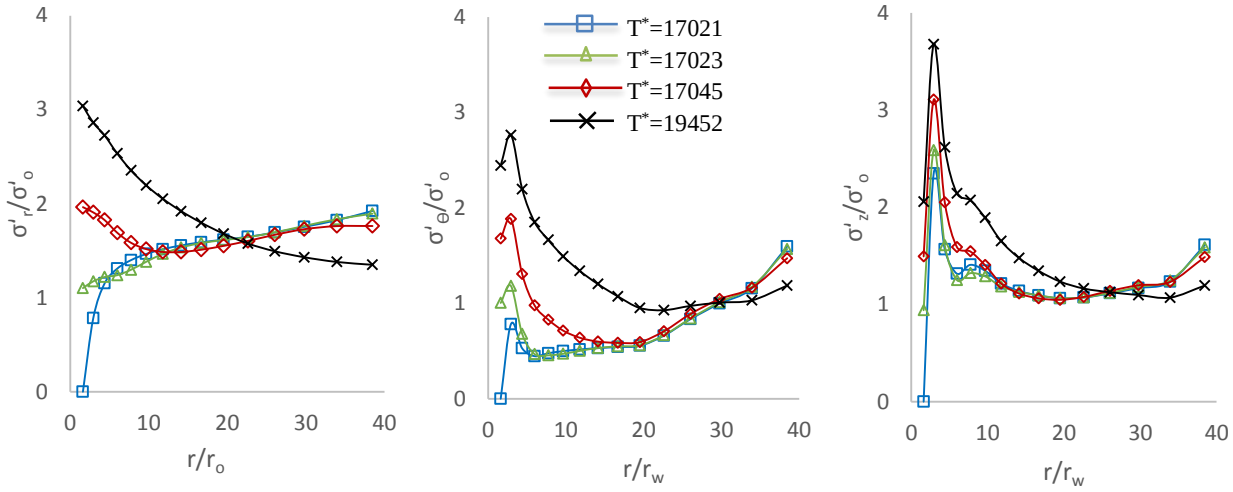

Figure 8-4. Effective stress distributions at different *T** during post-injection.

In order to better evaluate the permanent induced geomechanical impacts of injection, effective stress distributions at the *final state* are presented in Figure 8-5. Results also demonstrate permanent stress anisotropy induced due to radial injection. Effective stress distribution at the *final state* is found to be: $\sigma'_r \geq \sigma'_\theta > \sigma'_z$, at wellbore; $\sigma'_z > \sigma'_r \geq \sigma'_\theta$, in zone I; $\sigma'_r > \sigma'_z > \sigma'_\theta$, in zones II and III; $\sigma'_r > \sigma'_z \cong \sigma'_\theta$, in zone IV. The dominant major principal stress permanently induced as a result of radial injection in an unconsolidated reservoir confined with stiff seal rocks is found to be in radial direction.

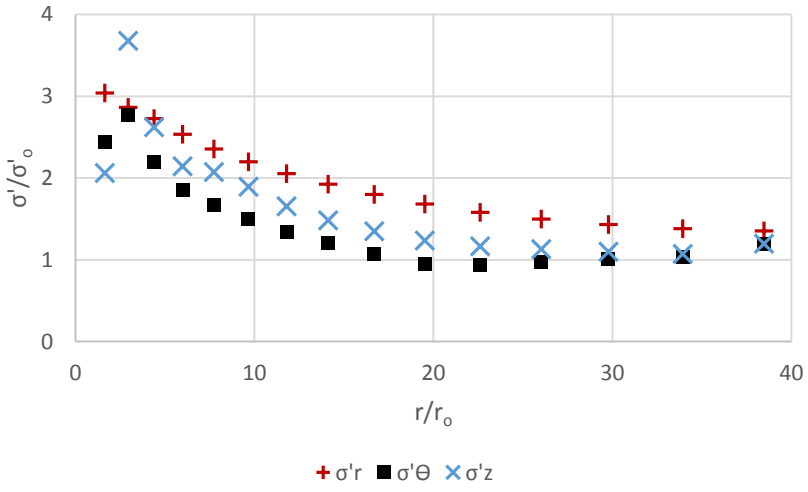

Figure 8-5. Effective stress distributions at final state.

In order to evaluate the plastic domain during the shut-in period, and to obtain better insight into the transition between a state of minimal shear resistance to a state of restored shear resistance, *PF* distributions at different times are plotted in Figure 8-6. Results illustrate a sudden drop at the wellbore at time T* = 17023, once injection is ceased. Therefore, the plastic domain changes into a state of restored shear resistance starting from the wellbore. At the *final state*, the area surrounding the boundary between the plastic and elastic regions (farthest location with respect to the wellbore, which demonstrates plasticity characteristics, r_p) contains highest values of *PF*.

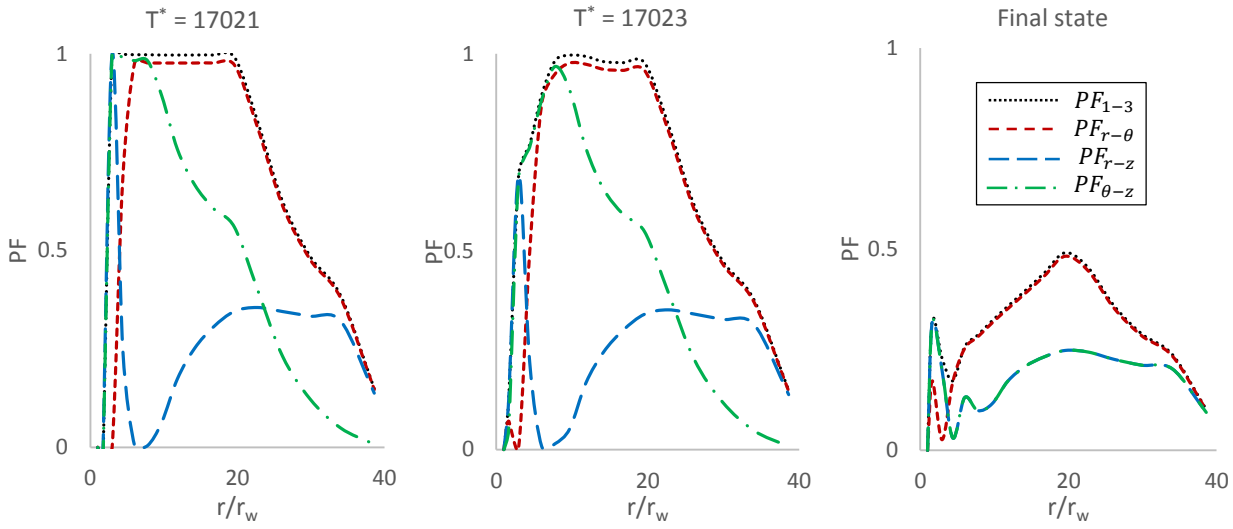

Figure 8-6. PF distributions at different planes for different T^*.

Variations in the induced radial displacements during the shut-in period are given Figure 8-7. As expected, results show a decrease in the induced deformations during post-injection. The ratio of the maximum induced displacements as a result of radial fluid injection obtained at the end of injection to the permanent deformations obtained at final state (u_{InjE}/u_{FS}) is given in Figure 8-8. This ratio increases linearly in both plastic and elastic domains with distance from the wellbore. Highest drop occurs in the elastic zone as expected.

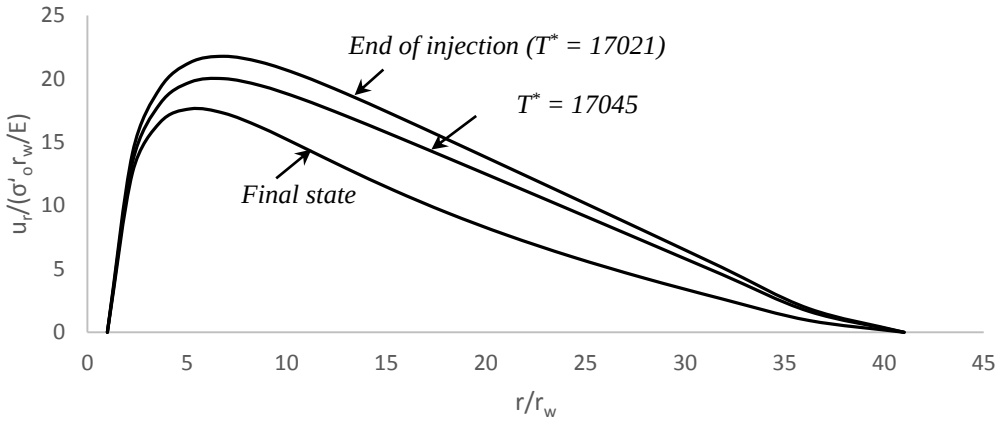

Figure 8-7. Radial displacement distributions during post-injection at different T^*.

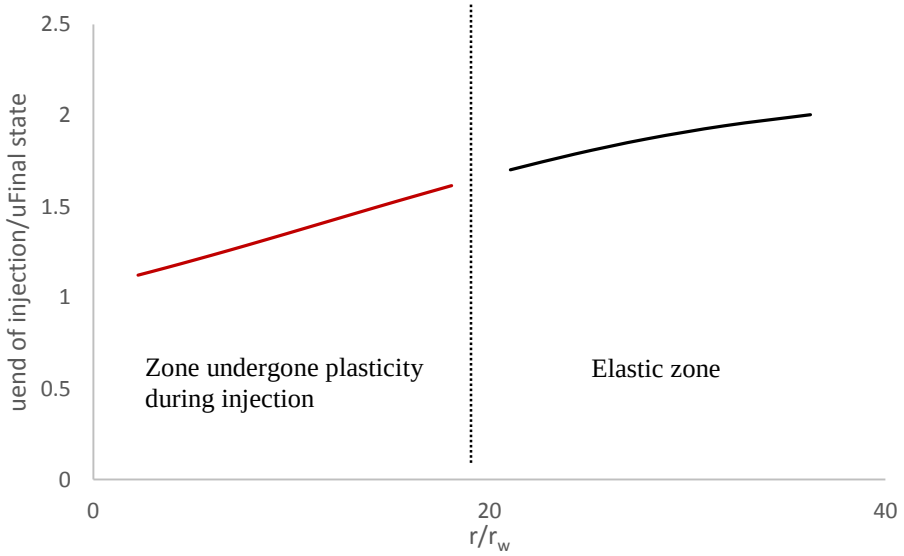

Figure 8-8. u_{InjE}/u_{FS} distribution.

In order to evaluate the geomechanical behavior of the porous medium during the shut-in period, stress paths at different observation points are plotted and presented in Figure 8-9. With respect to the observation point at the wellbore, an immediate increase in effective stresses and therefore a compacting response is detected from the liquefaction state once injection is ceased. This is consistent with observations from pore pressure and effective stress histories at the wellbore. As for the two observation points chosen within the plastic domain ($r/r_w = 4.5$, and $r/r_w = 6.0$), once injection is stopped, the stresses move on the failure

envelope in a dilative manner before entering an elastic state. This confirms the sudden drop in effective stresses observed in Figure 8-3. As for the observation point chosen far in the elastic domain ($r/r_w = 35.0$), the stress path indicates reduction in effective stresses is detected.

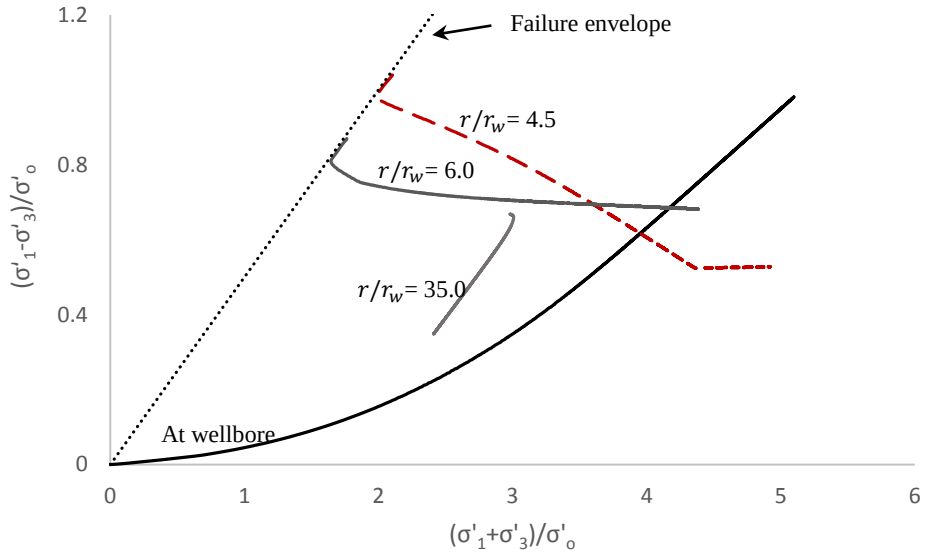

Figure 8-9. Stress paths at different observation points during shut-in period.

CHAPTER IX

9. Summary and Concluding Remarks

This dissertation presented a multi-faceted effort to assess coupled geomechanical processes during fluid injection from a fully penetrating vertical wellbore into an isotropic, homogeneous unconsolidated geological reservoir. The study focuses on coupled geomechanical processes triggered as a result of injection pressures that are high enough to induce plasticity yet not fracturing in the reservoir formation. The key objective of this research endeavor was to develop new analytical and numerical tools to: evaluate the coupled time dependent response of the geological formation to injection pressures; present a novel insight into failure mechanism/s plane/s induced during fluid injection; quantify extension of the significant influence zone surrounding the injection wellbore; and assess the permanent induced geomechanical effects of injection.

The first part of this dissertation concentrates on evaluating the poroelastic variations induced during fluid injection. Unlike previous studies, impacts of vertical confinement – governed by the stiffness of the overburden layer – on the coupled response of the reservoir formation during injection are incorporated.

- New coupled poroelastic closed-form analytical solutions were derived to describe the time dependent behavior of confined geological reservoirs during fluid injection, incorporating impacts of seal rock characteristics via implementation of the Winkle's soil model approximation.
- Analytical solutions were verified against new tightly-coupled numerical models developed in this study to evaluate wellbore injection, taking into account normal interactions between the reservoir and seal rocks.

- A new equation for the general consolidation coefficient was obtained contingent upon the medium's drained characteristic parameters, as well as permeability, fluid bulk modulus, and vertical confinement. The new equation approaches that of Rice and Cleary (1976), and Detournay and Cheng (1993) in formations with elastic moduli higher than 0.5 GPa. The impact of vertical confinement on "*c*" is substantial in case of lower elastic modului.
- Induced pore pressures aren't notably influenced by vertical confinement, although slightly higher values and shorter transient periods are detected under stiffer seal rocks.
- Induced vertical stress component is found to be the most sensitive to seal rock stiffness compared to horizontal stresses. The impact of K on σ_z is in fact fairly significant.
- The higher the seal rocks' stiffness, the larger induced radial displacements will be and the deformation field will expand in a wider domain.
- Largest vertical deformations occur under minimal vertical confinement.
- In order to define the influence domain due to injection in the elastic state, the extension of the radial deformation field is the most realistic parameter. Since the radial deformation field is a much wider domain compared to the region experiencing increase in pore pressures, or vertical deformations.
- Analytical expressions were derived for computing the magnitude and location of the maximum induced radial displacement at any given time based on injection rate. These can be applied as a valuable control parameter as well as a useful index for optimizing monitoring strategies.

The second part of this dissertation focuses on near wellbore stress modifications induced prior to failure initiation state. The objective was to present a novel insight for failure initiation within various in situ stress regimes, and to examine impacts of vertical confinement (governed by stiffness of the overburden layer) on the response of the porous medium. In order to obtain a generalized insight into geomechanics of fracturing, a comprehensive sensitivity analysis was conducted to evaluate effects of soil-injectant characteristic parameters on the coupled soil behavior. The poroelastic response of formations with a permeability lower than 0.05 Darcy was determined to be independent of seal rock stiffness. However, in typical hydrocarbon reservoirs which contain higher permeability, seal rock stiffness is found to have a notable impact on the poroelastic response of the near wellbore soil during injection. It is the ratio of vertical confinement, directly governed by seal rock stiffness, to reservoir's bulk modulus that dictates different stress behaviors. This ratio is found to be a limit state parameter: once the overburden stiffness yields to the bulk modulus of the reservoir formation, insignificant shear stresses are induced; once this ratio exceeds one, a gradual increase in shear stresses takes place; where this ratio is below unity, possible redirection of the minimum principal stress might occur from horizontal to vertical plane depending on the initial stress

field. Fracture redirection can therefore be explained to be a result of an increase in reservoir's bulk modulus during prolonged injection cycles. As a result of injection, continuous dilation takes place at the wellbore prior to experiencing shear failure independent of the initial stress field. In the specific case where $K_o = 0.9$, $K_{r\Theta} = 1.1$, the formation experiences failure close to liquefaction state. Failure is anticipated to initiate sooner in case of: higher anisotropy, higher elastic moduli, higher degree of soil-fluid coupling, lower permeability, and a higher vertical confinement.

The third part of this dissertation involves evaluation of the geomechanical response of an isotropic, homogeneous unconsolidated soil layer confined with stiff seal rocks under injection pressures that are high enough to induce plasticity but not fracturing. Results can directly be applied to assess geomechanics of "initial preconditioning" operations in a thin unconsolidated soil layer confined with stiff seal rocks.

a) A new tightly-coupled axisymmetric numerical model is developed to study wellbore injection. Stresses, strains, pore pressures, and principal planes are evaluated during the entire transient state of an injection cycle. The following are the observations and concluding remarks:

   – Failure mechanism at the wellbore is shear followed by liquefaction, which are both detectable in the pore pressure history at the borehole. The latter is an indication of fracture initiation.

   – Five distinctive zones of various plasticity states are induced during high pressure injection: at the wellbore surface where the soil matrix liquefies; two inner plastic domains where formation fails along two planes and the major principal stress is in vertical direction; the remainder of the plastic domain, where formation fails along one plane of r – θ and σ_1' is in radial direction; and the non-plastic region.

   – Two types of behaviors are induced as a result of high pressure injection: dilation (opening) of the reservoir formation at the area surrounding the wellbore; compaction in the remainder of the unconsolidated sand.

   – Substantial anisotropy is induced in a confined unconsolidated sand under radial injection: a decrease in radial and tangential effective stresses occurs in the immediate area surrounding the wellbore, while significant compaction is evident in the vertical direction.

   – Induced plastic region surrounding the wellbore propagates in time during the transient state of injection cycle. Major displacements takes place within this area.

   – Stress paths clearly reveal impacts of plasticity on stress-patterns in the subsequent elastic domain.

- Effective stresses do not change significantly once reaching the failure onset state.
- Substantial discrepancies are detected between pore pressures from fully coupled numerical models and values obtained from the simplified logarithmic equation at early times. However, not long into the injection cycle, the formation ceases to dilate as the reservoir is constrained, and numerical and analytical pressures approach similar values.

b) A novel methodology is presented based on which weakly-coupled analytical solutions are obtained for stresses/displacements throughout an unconsolidated reservoir during injection under plane strain conditions. Complete solutions for radial and tangential stress components are derived for the entire plastic domain. The vertical stress component however is statically indeterminate in zone III of the plastic zone. Nevertheless, an upper bound and a lower bound solution is presented for zone III of the plastic region. Complete solutions for all three stress components are presented in the elastic zone.

c) The weakly-coupled analytical solutions are found to be a good approximation of the coupled numerical model. This is convenient, as the runtime of the numerical model is significantly long (the run time of the numerical model in the current study was 6 months, 661 million steps, on an Intel® i7 processor, 3.33 GHz using FLAC3D version 3.0). Pressures, stresses, and displacement distributions, along with the extension of the plastic zone at any given time during injection can well be estimated based on the wellbore pore pressure using the analytical approach. Accuracy of the weakly-coupled analytical solution increases in time during injection, as in situ pressures approach the theoretical steady state equation.

The final part of this dissertation includes numerical evaluations of variations in stresses, strains, displacements, and pore pressures throughout an unconsolidated reservoir formation confined with stiff seal rocks during post-injection period. The following are the concluding remarks:

- Once injection is ceased, an anisotropic increase in effective stresses takes place at the wellbore. The maximum and minimum principal stresses at the wellbore at the *final state* are detected to be in the radial and vertical directions respectively.
- At the instant when injection is stopped, a sudden slight decrease in effective stresses is observed in locations farther from the wellbore. This is suspected to be due to equalization of pore pressures within the reservoir formation with cease of injection, as pore pressures tend to rapidly drop at the well while excess pore pressures continue to propagate to farther locations. Notable anisotropy in the stress field is observed at different locations in the *final state*.

– Higher in situ stresses compared to the initial state are detected at the *final state* in the once plastic region, indicating a clear permanent anisotropy induced due to high injection pressures explicitly within the plastic domain. Highest effective stresses in the final state are observed to be in the vertical plane.

– The dominant major principal stress permanently induced as a result of radial injection in an unconsolidated reservoir confined with stiff seal rocks is found to be in the radial direction.

– The plastic domain changes into a state of restored shear resistance starting from the wellbore. At the *final state*, the area surrounding the boundary between the plastic and elastic regions (farthest location with respect to the wellbore, which demonstrates plasticity characteristics, r_p) contains highest values of *PF*.

Appendix A

A.1 Derivation of transient pore pressure equation

The solution of equation 38 will be a function of consolidation coefficient, time, and radial distance from the injection source. This solution can be assumed to be in the following format:

$$p = f\left(\frac{cr^2}{4t}\right) \tag{A.1}$$

Computing $\frac{\partial^2 p}{\partial r^2}$, $\frac{\partial p}{\partial r}$ and $\frac{\partial p}{\partial t}$ from equation A.1 and substituting the obtained terms into equation 38, after some manipulation results in the following relation:

$$\frac{cr^2}{4t} f''\left(\frac{cr^2}{4t}\right) + (1 + \frac{cr^2}{4t}) f'\left(\frac{cr^2}{4t}\right) = 0 \tag{A.2}$$

where f' and f'' are respectively the first and second derivatives of the function f. Equation A.2 can be rewritten as:

$$\frac{dZ}{d\mathrm{v}}\mathrm{v} = -(1 + \mathrm{v})Z \tag{A.3}$$

where $\mathrm{v} = \frac{cr^2}{4t}$, and $Z = f'$. Consequently:

$$\int \frac{dZ}{z} = \int \frac{-(1 + \mathrm{v})}{\mathrm{v}}\, d\mathrm{v} \tag{A.4}$$

Solving the above integral equation will result in the following relation between the function *f* and variable v:

$$Z = \frac{df}{d\mathrm{v}} = \frac{\exp(-\mathrm{v})}{\mathrm{v}} \exp(b) \tag{A.5}$$

where *b* is in fact the integral constant. The term *exp (b)* is therefore a constant, which can be defined through boundary conditions. This term can be simply replaced with a constant variable of *C.* Function *f* is thus derived to be:

$$f = C \int_{\mathrm{v}}^{\infty} \frac{\exp(-\mathrm{v})}{\mathrm{v}} d\mathrm{v} \tag{A.6}$$

For injection purposes, *r > 0* resulting in v values greater than zero. The solution of equation A.5 can thus be expressed in terms of the exponential integral function given as follows:

$$f = CE_1(\mathrm{v}) = C \int_{\mathrm{v}}^{\infty} \frac{\exp(-\mathrm{x})}{\mathrm{x}} d\mathrm{x} \tag{A.7}$$

The transient pore pressure equation will therefore be:

$$p(r,t) = CE_1\left(\frac{cr^2}{4t}\right) \tag{A.8}$$

The integral constant *C* is obtained from boundary conditions as demonstrated in the following. At the location of injection source (on the wellbore interface) Darcy law results in the following relation between the pressure gradient and injection rate:

$$\frac{Q_o}{A} = -k\frac{\partial p}{\partial r} \tag{A.9}$$

or

$$Q_o = -k2\pi r_w h\frac{\partial p}{\partial r} \tag{A.10}$$

Derivative of *p* in terms of *r* can be obtained from equation A.8.

$$\frac{\partial p}{\partial r} = C\frac{d}{dr}E_1(\mathrm{X}) \tag{A.11}$$

or

$$\frac{\partial p}{\partial r} = -C\frac{2}{r}\exp(-\frac{cr^2}{4t}) \tag{A.12}$$

Substituting equation A.12 in A.10, for $r \rightarrow r_w$ results in the derivation of the integral constant *C*:

$$C = \frac{Q_o}{4\pi hk}\exp(\frac{cr_w^2}{4t}) \tag{A.13}$$

Regarding point source injection, $r_w \rightarrow 0$, which results in $\exp(\frac{cr_w^2}{4t}) \rightarrow 1$. In case of wellbore injection, r_w obtains a small value < 1m (typically 0.5 or smaller). The exponential function $\exp(\frac{cr_w^2}{4t})$ will therefore approach the value one soon after injection initiation. The integral constant *C* can thus be very well expressed independent of time and the consolidation coefficient, as demonstrated in equation A.14.

$$C = \frac{Q_o}{4\pi hk} \tag{A.14}$$

References

Abou-Sayed A., Zaki K., Wang G, Meng F., Sarfare M. (2004). Fracture Propagation and Formation Disturbance during Injection and Frac-Pack Operations in Soft Compacting Rocks. *In* Proceedings of SPE Annual Technical Conference and Exhibition, Houston, Texas, 26-29 Sep.

Abou-Sayed A, Zaki K, Wang G, Sarfare M. A Mechanistic Model for Formation Damage and Fracture Propagation during Water Injection (2005). *In* Proceedings of SPE European Formation Damage Conference, Sheveningen, Netherlands, 25-27 May.

Adachi J., Siebrits, E., Peirce, A., & Desroches, J. (2007). Computer simulation of hydraulic fractures. *International Journal of Rock Mechanics and Mining Sciences. 44*(5): 739-757.

Advani SH, Lee TS, Lee JK. (1990). Three-dimensional modeling of hydraulic fractures in layered media: part I—finite element formulations. *J. Energy Resour. Tech.*112:1–9.

Aguilera R. Naturally Fractured Reservoirs (1980). The Petroleum Publishing Company. Tulsa, Oklahoma.

Akpoborie I.A. (2005) Deep Well-Injection of Industrial and Hazardous Wastes in Nigeria: Prospects, Federal Regulations and the Ozoro Waste Injection Facility. *In* Proceedings of the Nigeria Annual International Conference and Exhibition, Abuja, 1-3 Aug.

Al Salem S., Al Samhan M. (2007). Plastic solid waste assessment in the state of Kuwait and proposed methods of recycling. *American Journal of Applied Sciences.* 4 (6): 354–356.

Arfie M., Marika E., Purbodiningrat E.S., Woodard, H.A., (2005). Implementation of slurry fracture injection technology for E & P wastes at Duri oilfield. *Society of Petroleum Engineers* Paper No. SPE-96543-PP.

Atefi Monfared K., Rothenburg L. (2011). Ground surface displacements and tilt monitoring for reconstruction of reservoir deformations. *International Journal of Rock Mechanics and Mining Sciences*. *48*(7): 1113-1122.

Atkinson B.K. (Ed.). (2013). *Fracture mechanics of rock*. Elsevier.

Baker B.D., Englehardt J.M., Reid J.D. (1999). Large scale NORM/NOW disposal through slurry waste injection. *Society of Petroleum Engineers* Paper No. SPE 53821.

Barree RD. (1983). A practical numerical simulator for three-dimensional fracture propagation in heterogenous media. *In* Proceedings of the SPE symposium reservoir simulation, San Francisco, November 15–18. Richardson: Society of Petroleum Engineers:403–13 [SPE 12273]

Bellarby J. (2009) *Well completion design*. Vol. 56. Elsevier.

Ben Naceur K, Thiercelin M, Touboul E. (1990) Simulation of fluid flow in hydraulic fracturing: implications for 3D propagation. *SPE Prod Eng J*:133–41 [SPE 16032].

Bianco, L. C. B. (1999). *Phenomena of sand production in Non-consolidated sandstones* (Doctoral dissertation, Pennsylvania State University).

Biot, M.A., 1941. General theory of three-dimensional consolidation (1941). *J. of Appl. Phys.* 12, 155-164.

Bloch S., Lander R.H., and Bonnell L. (2002). Anomalously high porosity and permeability in deeply buried sandstone reservoirs: Origin and predictability. *AAPG Bulletin*, 86(2): 301–328.

Board, M., Rorke, T., Williams, G., Gay, N. (1992). Fluid injection for rockburst control in deep mining. In: Tillerson JR, Wawersik WR, editors. *In*: Proceedings of the 33rd U.S. symposium on rock mechanics. Rotterdam: Balkema. p. 111–20.

Bohloli B, de Pater CJ. (2006) Experimental Study on Hydraulic Fracturing of Soft Rocks: Influence of Fluid Rheology and Confining Stress. *Journal of Petroleum Science and Engineering*; **53**: 1–12.

Bratli, R.K. and Risnes, R. Stability and Failure of Sand Arches. *Soc. Pet. Eng. J*. 1981; **21(2)**: 236 – 248.

Broek D. (1986) Elementary Engineering Fracture Mechanics. 4th Edition Revised, Kluwer Academic Publishers.

Bruno M.S., Dorfmann A., Lao K., Honeger C. (2001) Coupled Particle and Fluid Flow Modeling of Fracture and Slurry Injection in Weakly Consolidated Granular Media. *In*: Proceedings of North American Rock Mech. Conf., Washington D.C., 7-10 Jul.

Carter J.P., Booker J.R. (1982). Elastic consolidation around a deep circular tunnel. *Int. J. Solids Struc.* 18(12), 1059 – 1074.

Carter B.J., Desroches J., Ingraffea A.R., Wawrzynek P.A. (2000) Simulating fully 3D hydraulic fracturing. *In*: Zaman M., Booker J., Gioda G., editors. Modeling in geomechanics. New York: Wiley Publishers.

Chekhonin E., Levonyan K. (2012). Hydraulic fracture propagation in highly permeable formations, with applications to tip screenout. *International Journal of Rock Mechanics and Mining Sciences*, *50*, 19-28.

Chin L.Y., Raghavan R., Thomas, L.K., (2000). Fully coupled geomechanics and fluid-flow analysis of wells with stress-dependent permeability. *SPE J*. 5(1), 32-45.

Clifton R.J., Abou-Sayed, A.S. (1981). A variational approach to the prediction of the three-dimensional geometry of hydraulic fractures. *In*: Proceedings of the SPE/DOE low permeability symposium, Denver, May 27–29. Richardson: Society Petroleum Engineers; 1981 [SPE 9879].

Clifton R.J., Wang J.J. (1991). Adaptive optimal mesh generator for hydraulic fracturing. *In*: Roegiers JC, editor. Rock mechanics as a multidisciplinary science. Rotterdam: Balkema: 607–16.

Cornell R.W. (1953). Determination of stresses in cemented lap joints. *J. Appl. Mech*., 20:355-364.

Dal Ferro, B., Smith M. (2007). Global Onshore and Offshore Water Production. ⟨http://www.touchoilandgas.com/global-onshore-offshore-water-a7137-1.html⟩.

Desai C.S., Siriwardane H.J. (1984) Constitutive Laws for Engineering Materials: With Emphasis on Geologic Materials. Prentice Hall, Inc., Englewood Cliffs, New Jersey.

Desroches J., Thiercelin M. (1993). Modeling propagation and closure of micro-hydraulic fracturing. *Int. J. Rock Mech. Min. Sci.*; 30: 1231–4.

Desroches J. (1995). Stress testing with the micro-hydraulic fracturing technique—focus on fracture reopening. *In*: Daemen JK, Schultz RA, editors. Proceedings of the 35th U.S. symposium on rockmechanics. Rotterdam: Balkema. p. 217–23.

Detournay, E., Cheng, AHD. (1988). Poroelastic response of a borehole in a non-hydrostatic stress field. *Int. J. Rock Mech. Min. Sci. & Geomech*. 25(3), 171-182.

Detournay E, Cheng AHD.(1993) Fundamentals of Poroelasticity. Comprehensive Rock Engineering: Principles, Practice & Projects, Vol. II, Analysis and Design Method (Edited by Fairhurst C) Pergamon, Oxford; pp. 113-171.

Dong K.J., Zou R.P., Yang R.Y., Yu A.B., Roach G. (2009) DEM Simulation of Cake Formation in Sedimentation and Filtration. *Journal of Minerals Engineering*; 22:921-930.

Dusseault M.B., Geilikman M.B. & Roggensack, W.D. (1995). Practical requirements for sand production implementation in heavy oil applications. *SPE, 30250*, 19-21.

Dusseault M.B., Bilak R.A., & Rodwell L.G. (1997). Disposal of dirty liquids using slurry fracture injection. In *SPE/*EPA exploration and production environmental conference (pp. 193-203).

Dusseault M.B., Geilikman M.B., & Roggensack W.D. (1995). Practical requirements for sand production implementation in heavy oil applications. *SPE, 30250*, 19-21.

Dutton S.P., Flanders W.A., & Barton M.D. (2003). Reservoir characterization of a Permian deep-water sandstone, East Ford field, Delaware basin, Texas. *AAPG bulletin*, *87*(4): 609-627.

Economides M.J., Nolte K.G. Reservoir simulation. 3rd ed. Chichester: Wiley; 2000.

Economides M.J., Oligney R.E., Valko´ P.P. (2002) Unified fracture design: bridging the gap between theory and practice. Alvin, Texas: Orsa Press.

Egberts, P.J.P., Fokker, P.A. (2001). A new analytical approximation for the flow into a well in a finite reservoir. *Trans. In Porous Media* 44, 85 – 107.

Engelder, T., Fischer, MP. (1994). Influence of poroelastic behaviour on the magnitude of minimum horizontal stress, Sh, in overpressured parts of sedimentary basins. *Geology* 22, 949–52.

Fakhru´l-Razi A. , Pendashteh A. , Abdullah L.C., Biak D.R.A., Madaeni S.S., Abidin Z.Z. (2009). Review of technologies for oil and gas produced water water-treatment. *J. Hazard.Mater*.170: 530–551.

Fan Y., Economides, M.J. (1996) Fracture dimensions in Frac & Pack stimulation. *Soc. Pet. Eng. J.* 403–12.

Freeze RA, Cherry JA. (1979) *Groundwater*. Prentice-Hall, Inc. Englewood Cliffs, NJ.

Geertsma J. (1957). A Remark on the analogy between thermo-elasticity and the elasticity of saturated porous Media. *J . Mech. Phys. Solids* 6: 13-16.

Geertsma J, de Klerk F. (1969). A rapid method of predicting width and extent of hydraulically induced fractures. *J. Pet. Tech*. 21:1571–81 [SPE 2458]

Germanovich L.N., Hurt R.S., Ayoub J.A., Siebrits E., Norman W.D., Ispas I., Montgomery C. (2012) Experimental Study of Hydraulic Fracturing in Unconsolidated Materials. *In* Proceedings of SPE International Symposium and Exhibition on Formation Damage Control, Lafayette, Louisiana, USA, 15-17 Feb.

Gholami R., Moradzadeh A., Rasouli V., Hanachi J. (2014). Practical application of failure criteria in determining safe mud weight windows in drilling operations. *J. of Rock Mech. and Geotechnical Eng.* 6(1), 13-25.

Gil I., Roegiers J.C. (2003) Coupled Elasto-Plastic Model for Hydraulic Fracturing of Unconsolidated Formations. ISRM 2003–Technology Roadmap for Rock Mechanics, South African Institute of Mining and Metallurgy 2003; 363-370.

Gil I. (2005) Hydraulic Fracturing of Poorly Consolidated Formations: Considerations on Rock Properties and Failure Mechanisms. Doctoral dissertation, University of Oklahoma, Norman, Oklahoma.

Goodier J.N., Kanninen M.F. (1966). Crack propagation in a continuum model with nonlinear atomic separation laws. Tech. Rep. 165, Div. Eng. Mech., Stanford University.

Goodman R.E., Taylor R.L., Brekke T.L. (1968). A model for the mechanics of jointed rock. J. Soil Mech. Found. Div., ASCE 94 (SM3), 637 – 659.

Goulty N.R. (2003) Reservoir stress path during depletion of Norwegian chalk oilfields. *Pet. Geosci*. 9, 233–241.

Griffith AA. The Phenomena of Rupture and Flow in Solids. Phil. Trans. R. Soc 1921. A221: 163-198.

Gnirk P.F. 1972. The mechanical behavior of uncased wellbores situated in elastic/plastic media under hydrostatic stress. *Soc. Pet. Eng. J.* 49 – 59.

Guo Q., McLennan J.D., Martin J., & Geehan T. (2008, January). A Laboratory Study on Increased Assurance and Understanding Storage Mechanism of E&P Wastes Injection into an Unconsolidated Formation. *In* SPE International Conference on Health, Safety, and Environment in Oil and Gas Exploration and Production. SPE.

Gueguen Y, Bouteca M. (2004) Mechanics of Fluid Saturated Rocks. ELSEVIER Academic Press. International Geophysics Series.

Han G., Dusseault M.B. (2003). Description of fluid flow around a wellbore with stress-dependent porosity and permeability. *J of Pet. Sci. Eng.* 40(1), 1 – 16.

Hawkes C.D., McLellan P.J., Bachu S. (2005). Geomechanical factors affecting geological storage of CO2 in depleted oil and gas reservoirs. *J. Can. Pet. Technol*. 44 (10), 52–61.

Hill, R. (1950) *the mathematical theory of Plasticity*, Oxford University Press, London.

Hofmann H., Babadagli T., & Zimmermann G. (2014). Hot water generation for oil sands processing from enhanced geothermal systems: Process simulation for different hydraulic fracturing scenarios. *Applied Energy, 113*, 524-547.

Hsiao C. (1988). Growth of plastic zone in porous medium around a wellbore. *In* Proceeding of the 20th Annual OTC, Houston, Texas, 2-5 May, 439-448.

Hu K., Dietrich J. (2009, May). Hydrocarbon Reservoir Potential in Carboniferous Sandstones in the Maritimes Basin, Eastern Canada. In*Frontiers+ Innovation–2009 CSPG CSEG CWLS Convention*.

Hubbert M.K., Willis D.G. (1972) Mechanics of hydraulic fracturing: 239-257.

Hutter K., (1975). Floating sea ice plates and the significance of the dependence of the poisson ratio on the brine content. Proc. R. Soc. London, Ser. A., 343: 85-108.

Kanninen M.F. (1973). An augmented double cantilever beam model for studying crack propagation and arrest. *Int. J. Fract.*, 9:83-92.

Keck R.G. (2002) Drill Cuttings Injection: A Review of Major Operations and Technical Issues. SPE 77553, SPE Annual Technical Conference, San Antonio, 29 September - 2 October 2002.

Khatib Z., Verbeek P. (2002).Water to value-produced water-management for sustainable field development of mature and green fields. *In* Proceedings of the SPE International Conference on Health, Safety and Environment in Oil and Gas exploration and Production, Kuala Lumpur, Malaysia,March20–22.

Khodaverdian M, Sorop T, Postif S, Van den Hoek P. (2009) Polymer Flooding in Unconsolidated Sand Formations: Fracturing and Geomechanical Considerations. *In* Proceedings of SPE Europian/EAGE Annual Conference and Exhibition, Amsterdam, Netherlands, 8-11 Jun.

Khristianovic SA, Zheltov YP. Formation of vertical fractures by means of highly viscous liquid. *In* Proceedings of the fourth world petroleum congress, Rome, 1955: 579–86.

Kirsch. Die Theorie der Elastizität und die Bedürfnisse der Festigkeitslehre. Zeitschrift des Vereines deutscher Ingenieure, 1898; 42: 797–807.

Kroon, I.C., Nguyen, B.L., Fokker, P.A., Muntendam-Bos, A.G., Lange, G.D. (2008). Disentangling shallow and deep processes causing surface movement. Math Geosci. 2008; 41(5):571–84.

Legarth B., Huenges E., & Zimmermann G. (2005). Hydraulic fracturing in a sedimentary geothermal reservoir: Results and implications. *International Journal of Rock Mechanics and Mining Sciences*, *42*(7): 1028-1041.

Lister JR. (1990). Buoyancy-driven fluid fracture: the effects of material toughness and of low-viscosity precursors. J Fluid Mech.; 210: 263–80.

Mader D. (1989) Hydraulic Proppant Fracturing and Gravel Packing. ELSEVIER Science Publishing Company INC.

Mack MG, Warpinski NR. Mechanics of hydraulic fracturing. *In* Economides, Nolte, editors. Reservoir stimulation. 3rd ed. Chichester; Wiley: 2000 [Chapter 6].

Meyerhof G.G. (1960). Bearing capacity of floating ice sheets. *J. Eng. Mech. Div., Proc. A.S.C.E.*, 86: EM5, 110-145.

Monicard R.P. (1980) Properties of Reservoir Rocks: Core Analysis. Editions Technip Paris.

Montgomery C.T., Smith, M.B. (2010). Hydraulic fracturing: history of an enduring technology. *J. Pet. Techol. 62*(12): 26-40.

Morita N., Whitfill D.L., Nygaard O., Bale A. (1989). A quick method to determine subsidence, reservoir compaction, and in-situ stress induced by reservoir depletion. *J. Pet. Technol*. 41(1): 71 – 84.

Moschovidis Z.A., Gardner D.C., Veatch R.W. (1993) Disposal of Oily Cuttings by Downhole Periodic Fracturing Injections in Valhall - North Sea: A Case Study and Modeling Concept. SPE/IADC 25757, 1993 SPE/IADC Drilling Conference, Amsterdam, 23- 25 February.

Moschovidis Z., Steiger R., Peterson R., Warpinski N., Wright C., Chesney E., & Akhmedov O. (2000, January). The Mounds Drill-Cuttings Injection Field Experiment: Final Results and Conclusions. *In* IADC/SPE Drilling Conference. Society of Petroleum Engineers.

Nadeem M., Dusseault M.B., Bilak R.A. (2005) Assessment Criteria for Deep Waste Disposal Sites. *In* Proceedings of Alaska Rocks 2005, 40th U.S. Symposium on Rock Mechanics (USRMS), Anchorage, AK, 25-29 June.

Nordren RP. (1972) Propagation of a vertical hydraulic fracture. *SPE J.* 12(8):306–14 [SPE 7834].

Olson J.E., Holder J., Hosseini S.M. (2011) Soft Rock Fracturing Geometry and Failure Mode in Lab Experiments. *In* Proceedings of SPE Hydraulic Fracturing Technology Conference, The Woodlands, Texas, USA, 24-26 Jan.

Pape, H., Clauser, C., Iffland, J. (1999). Permeability Prediction for Reservoir Sandstones and Basement Rocks Based on Fractal Pore. *J. Geophysics*; 64(5):1447-1460.

Paslay, P.R., Cheatham, J.B., (1963). Rock stresses induced by flow of fluids into borehole. *Soc. Pet. Eng. J*. 3(1): 85 – 94.

Pedroso CA, Marques LC, Paixão LC, Pires PR, Junior EBL. Analysis of Fracture Growth Induced by the Injection of Water above the Fracture Pressure in Nonconsolidated Sandstones and Soft Carbonates. In: Proceedings of Nigeria Annual International Conference and Exhibition, Tinapa - Calabar, Nigeria, 31 July - 7 Aug 2010.

Perkins T.K., Kern L.R. (1961)Widths of hydraulic fractures. *J Pet Tech.* 13(9):937–49 [SPE 89].

Pine R.J., Cundall P.A. Applications of the Fluid-Rock Interaction Program (FRIP) to the modelling of hot dry rock geothermal energy systems. *In* Proceedings of the international symposium on fundamentals of rock joints, Bjorkliden, Sweden, September 293–302, 1985.

Potyondy D.O., Cundall P.A, and Lee C. (1996) Modeling rock using bonded assemblies of circular particles. *In* Aubertin M., Hassani, F., and Mitri, H., editors. Rock Mechanics Tools and Techniques. Rotterdam: Balkema; 1937-44.

Reed A.C., Mathews J.L., Bruno M.S., Olmstead S.E. (2001). Chevron safely disposes one million barrels of NORM in Louisiana through slurry fracture injection. *Society of Petroleum Engineers* Paper No. SPE 71434.

Reissner E., Goland M. (1944). The stress in cemented joints. *J. Appl. Mech*. 66: A17-A27.

Rice J.R., Cleary M.P. (1976). Some basic stress diffusion solutions for fluid-saturated elastic porous media with compressible constituents. *Rev. Geophysics*. 14, 227 – 241.

Risnes R., Bratli R.K., Horsrud P. (1982). Sand stress around a wellbore. *SPE J*. 22(6): 883- 898.

Rubin A.M. (1995) Propagation of magma-filled cracks. *Ann Rev Earth Planet Sci*. 23:287–336.

Rudnicki J.W. (1999). Alteration of regional stress by reservoirs and other inhomogeneities: stabilizing or destabilizing?. In 9th ISRM Congress. *Int. Soc. for Rock Mech*.

Saif Ud Din, Oskui, G.P.R., Al Dousari, A., Al Ghadban, A.N., Al Murad, M., (2009). An environmentally viable waste disposal method for oil producing countries. *J. Waste Management & Research*. doi:10.1177/0734242X09335698.

Salehi S., Hareland G., Nygaard R. (2010). Numerical simulations of wellbore stability in under-balanced-drilling wells. *J. Pet. Sc. Eng.* 72(3): 229-235.

Samieh A.M., Wong R.C.K. (1998) Modeling the Responses of Athabasca oil Sand in Triaxial Compression Tests at Low Pressures. *Canadian Geotechnical Journal.* 35(2):395-406.

Sanchez M., Tibbles R. (2007). Frack Packing: Fracturing for Sand Control. Middle East & Asia Reservoir Review. 8: 38-49.

Sanfilippo F., Dusseault M.B., & Santarelli F. J. (2009). Waste Disposal In to the Deep Underground-Technical And Economical Considerations For Applications Outside The Oil Industry. *In* International Petroleum Technology Conference.

Schuh P.R., Secoy B.W., Sorrie E. (1993). Case history: cuttings reinjection on the Murdoch development project in the southern sector of the North Sea. *Society of Petroleum Engineers*. SPE 26680.

Sneddon IN (1946). The distribution of stress in the neighbourhood of a crack in an elastic solid. *Proc. R Soc. London* 187: 229–60.

Segall P. (1992). Induced stresses due to fluid extraction from axisymmetric reservoirs. *Pure and Applied Geophysics*, 139(3-4), 535-560.

Segall P., Fitzgerald S.D. (1998). A note on induced stress change in hydrocarbon and geothermal reservoirs. T*ectonophysics* 289, 117–128.

Selvadurai A.P.S. (1977). Axisymmetric deformation of a Winkler layer by internally loaded elastic halfspaces. Mech. Res. Comm., 4:241-246.

Selvadurai A.P.S. (1978). An approximate analysis of an internally loaded elastic plate containing an infinite row of clsely spaced parallel cracks. *J. Eng. Fract. Mech*., 10.

Selvadurai, A.P.S. (1979). Elastic analysis of soil-foundation interaction. Elsevier Scientific co.

Sipple-Srinivasan M., Bruno M.S., Bilak R.A., Danyluk P.G. (1997). Field experiences with oilfield waste disposal through slurry fracture injection. *Society of Petroleum Engineers* Paper No. SPE 38254.

Sipple-Srinivasan M.M.S., Bruno M.S., Hejl K.A., Danyluk P.G., Olmstead S.E. (1998). Disposal of crude contaminated soil through slurry fracture injection at the West Coyote field in California. *Society of Petroleum Engineers* Paper No. SPE 46239.

Shokanov T, Gumarov S, Ronderos J. (2011) Multiple-Fractures Propagation, Orientation and Complexities in Drilling Waste Injection. In: proceedings of SPE Hydraulic Fracturing Technology Conference, The Woodlands, Texas, U, 24-26 Jan.

Showalter R.E., Stefanelli U. (2004) Diffusion in Poro-plastic Media. *J. of Math. Meth. Appl. Sci*. 27:2131-2151.

Siebrits E., Peirce A.P. (2002). An efficient multi-layer planar 3D fracture growth algorithm using a fixed mesh approach. *Int. J. Numer. Meth. Eng.* 53:691–717.

Smith, G.E. (1988) Fluid Flow and Sand Production in Heavy-Oil Reservoirs under Solution-Gas Drive. *Soc. Pet. Eng.J.* 3(2): 169 – 180.

Soltanzadeh H., Hawkes C.D. (2008). Semi-analytical models for stress change and fault reactivation induced by reservoir production and injection. *J. Pet. Sci. Eng*. 60(2), 71-85.

Spence D.A., Turcotte D.L. (1985). Magma-driven propagation crack. *J Geophys Res*.; 90:575–80.

Streit J.E., Hillis R.R. (2004). Estimating fault stability and sustainable fluid pressures for underground storage of CO2 in porous rock. *Energy* 29, 1445–1456.

Terzaghi K. (1923) Die Berechnung der Durchl¨assigkeitsziffer des Tones aus dem Verlauf der hydrodynamische Spannungserscheinungen, Sitzber. Akad. Wiss. *Wien, Abt. IIa*, 132: 125-138.

Thallak S, Rothenburg L, Dusseault M.B. (1991) Simulation of Multiple Hydraulic Fractures in a Discrete Element System. In: Proceedings of 32nd U.S. Symposium on Rock Mechanics (USRMS), Norman, Oklahoma, 10-12 July; 271-280.

U.S. Environmental Protection Agency. Citing online sources: Classes of Injection Wells[online]. Available from http://permanent.access.gpo.gov/lps21800/www.epa.gov/safewater/uic/classi.html [last updated on September 16th, 2004].

Vandamme L., Curran J.H. (1989). A three-dimensional hydraulic fracturing simulator. *Int. J. Numer. Meth. Eng.*; 28: 909–27.

Walton I.C., Atwood D.C., Halleck P.M., Bianco C.B. (2002). Perforating unconsolidated sands: an experimental and theoretical investigation. *SPE Drilling Completion J.* 17(3),141–150.

Wang Y, Dusseault M.B. (1991) Borehole Yield and Hydraulic Fracture Initiation in Poorly Consolidated Rock Strata-PartII. Permeable Media. *Int. J. Rock. Mech. Min. Sci. & Geomech*. 28(4):247-260.

Wang HF (2000). Theory of Linear Poroelasticity with Applications to Geomechanics and Hydrogeology. Princeton University Press.

Wangen M. (2011) Finite Element Modeling of Hydraulic Fracturing on a Reservoir Scale in 2D. *Journal of Petroleum Science and Engineering* 77(3-4): 274–285.

Warren E.A., Pulham A.J. and Naar J. (1997). Primary compositional control on quartz cement and porosity in deeply-buried sandstones, Cusiana field, Llanos foothills, Colombia (abs.): AAPG Annual Convention, Program with Abstracts, 6: A122–A123.

Wong R.C.K., Barr W.E., Kry P.R. (1993) Stress-strain Response of Cold Lake oil Sands. *Canadian Geotachnical Journal* 30(2):220-235.

Wong R.C.K. (2003) Strain-Induced Anisotropy in Fabric and Hydraulic Parameters of Oil Sand in Triaxial Compression. *Canadian Geotechnical Journal* 2003;40(3):489-500.

Wong R.C.K. (2003) A model for Strain-Induced Permeability Anisotropy in Deformable Media. *Canadian Geotechnical Journal* 40(1):95-106.

Wu R. (2006) Some Fundamental Mechanics of Hydraulic Fracturing. *PhD thesis*, Civil and Environmental Engineering, Georgia Institute of Technology, Atlanta, Georgia.

Wyman M. (1950). Deflections of an infinite plate. *Can. J. Res. Sec. A.*, 28: 293 – 302.

Xu B., Wong R.C.K. (2010) A 3D Finite Element Model for History Matching Hydraulic Fracturing in Unconsolidated Sands Formation. *J. Canadian Pet. Tech.*;49: 58-66.

Yang D., Udey N., Spanos T.J.T. (2004) Automaton Simulations of Dispersion in Porous Media. *Transport in Porous Media*, (32): 187-198.

Yin S., Rothenburg L., Dusseault M.B. (2006). 3D Coupled displacement discontinuity and finite element analysis of reservoir behavior during production in semi-infinite domain. *J. of Transport in Porous Media*, 65,425-441.

Yin S., Dusseault M.B., Rothenburg L. (2009) Multiphase Poroelastic Modeling in Semi-Space for Deformable Reservoirs. *J. Pet. Sci. Eng.* 64:45-54.

Zhai Z., Sharma M.M. (2005) A New Approach to Modeling Hydraulic Fractures in Unconsolidated Sands. In: Proceedings of SPE Annual Technical Conference and Exhibition, Dallas, Texas, 9-12 Oct.

Zhang X, Detournay E, Jeffrey R. (2002) Propagation of a penny-shaped hydraulic fracture parallel to the free-surface of an elastic half space. *Int J Fract.* 115:126–58.

Zhang Y.J., Li Z.W., Guo L.L., Gao P., Jin X.P., & Xu T.F. (2014). Electricity generation from enhanced geothermal systems by oilfield produced water circulating through reservoir stimulated by staged fracturing technology for horizontal wells: A case study in Xujiaweizi area in Daqing Oilfield, China.*Energy*, *78*, 788-805.

Zhang Y.J., Li Z.W., Yu Z.W., Guo L.L., Jin X.P., & Xu T.F. (2015). Evaluation of developing an enhanced geothermal heating system in northeast China: Field hydraulic stimulation and heat production forecast. *Energy and Buildings*, *88*, 1-14.

Zhou J., Dong Y., de Pater C.J., Zitha P.L.J. (2010) Experimental Study of the Impact of Shear Dilation and Fracture behavior During Polymer Injection for Heavy Oil Recovery in Unconsolidated Reservoirs. In: Proceedings of Canadian Unconventional Resources & International Petroleum Conference, Calgary, Alberta, 19-21 Oct.

Zoback M.D., Zinke J.C., (2002). Production-induced normal faulting in the Valhall and Ekofisk oil fields. *Pure Appl. Geophys*. 159, 403–420.

Zoback M.D. (2010). *Reservoir geomechanics*. Cambridge University Press.